



Université Grenoble Alpes

Report

Mid-term

MIRA Anna

Supervisors:

Yohan Payan, TIMC-IMAG Lab, CNRS & Univ. Grenoble Alpes
Serge Muller, GE-Healthcare, France
Ann-Katherine Carton, GE-Healthcare, France

V2

Grenoble, September 2016

Contents

Contents	iii
List of Figures	vii
⁵ List of Tables	xi
I Introduction	1
General Problem statement	2
Technical approach	3
Thesis overview	4
¹⁰ Key contributions	5
Software	6
Ethics	7
II Background	9
1 Clinical background	10
¹⁵ 1.1 Introduction	10
1.2 Breast anatomy	11
1.2.1 Breast embryogenesis	11
1.2.2 Breast Appearance	12
1.2.3 Internal structure	13
²⁰ 1.2.4 Adult breast texture changes	17
1.3 Breast Cancer	17
1.3.1 Cancer classification	18
Report	iii

25	1.3.2 Breast cancer screening	19
1.4 Medical Imaging	19	
25	1.4.1 X-ray mammography	19
1.4.2 Ultrasounds	21	
25	1.4.3 Magnetic resonance imaging	21
1.5 Conclusion	22	
III Biomechanical breast modeling		23
30	2 Background and state of the art	24
2.1 Introduction	24	
2.2 Continuous mechanics	25	
35	2.2.1 Deformation and strain	25
2.2.2 Stress measures	29	
35	2.2.3 Conservation equations	31
2.2.4 Constitutive models	33	
2.3 Finite Element Discretization	36	
2.3.1 Eulerian and Lagrangian mesh description	36	
2.3.2 Lagrangian mesh	37	
40	2.4 Contact mechanics	40
2.4.1 Contact interface equations	41	
2.4.2 Surface interaction models	42	
2.4.3 Contact formulation algorithm: Pure Penalty model	43	
45	2.5 Breast biomechanical model: overview	46
2.5.1 Breast reference configuration	46	
2.5.2 Constitutive models	48	
2.5.3 Boundary conditions	52	
2.5.4 Conclusion	52	
50	3 A new biomechanical breast model	55
3.1 Introduction	55	
3.2 Geometry extraction	56	
3.2.1 Data acquisition	56	
3.2.2 Image segmentation	57	
3.2.3 Image registration	58	
55	3.2.4 Patient-specific 3D geometry	59
3.3 Finite Elements Mesh	60	
3.4 Breast reference configuration	61	
3.5 Boundary conditions	63	
3.6 Materials constitutive models	65	
60	3.6.1 Model simplification	66
3.6.2 Estimation of optimal constitutive parameters	68	

3.6.3	Conclusion	69
4	Model validation	72
65	4.1 Introduction	72
	4.2 Technical approach	73
	4.3 Results	73
	4.4 Discussions and conclusion	75
IV	Breast Compression: a comparative study	77
5	Background	78
70	5.1 Introduction	78
	5.2 Breast compression: overview	79
	5.2.1 Mammographic positioning	79
	5.2.2 Compression mechanics	80
	5.2.3 Compression paddle designs	81
75	5.3 Pain and discomfort	82
	5.4 Image quality and average glandular dose	82
	5.5 Conclusion	82
6	Breast compression quality evaluation	83
80	6.1 Breast compression simulation	83
	6.2 Image acquisition simulation	83
	6.3 Compresure quality metrics	83
	6.3.1 Patient comfort	83
	6.3.2 Image quality	84
	6.3.3 Average glandular dose	84
85	6.4 Results	85
	6.5 Discussions and conclusion	90
V	Thesis review	91
	Conclusion	92
	Perspective	93
90	Bibliography	94

List of Figures

95	1.1 Breast embryogenesis: embryonic evolution of duct system. The epidermis is responsible for the creation of ductal system and alveoli, the dermis mes- enchyme is responsible for the creation of connective tissue and vessels	11
100	1.2 Breast development sequence into subcutaneous tissues. A Mammary bud development by splitting the superficial fascia in 2 layers. B Mammary bud development by superficial fascia retracting	12
105	1.3 Left: thorax landmarks; Right: four breast quadrants	12
110	1.4 Breast anatomy	14
	1.5 Skin anatomy	15
	1.6 Suspensory ligaments	16
	1.7 Lymphatic system and Mammary Arteries for adult female breast	16
	1.8 Mammographyc exam	20
115	2.1 The position of a particle in the reference and current body configurations.	26
	2.5 a) Lagrangian mesh formulation. b) Euler mesh formulation	36
	2.6 From strong formulation of the generalized momentum balance (GMB) to numerical equations.	37
120	2.7 a) Discretization of a 2D domain with triangular finite elements :Lagrangian mesh . b) Different types of finite elements	38
	2.8 Computation of the aspect ratio for a triangle	39
	2.9 Example of triangles with different maximal corner angles.	39
	2.10 Example of triangles with different skewness with the corresponding circum radius.	40
	2.11 Multi-body contact problem.	41
	2.12 Contact status update using a pinball of radius r. Green nodes- updated nodes to closed contact status; gray nodes - updated nodes to open contact status; blue nodes- nodes which contact status need to be updated	44
	2.13 a) Body \mathcal{A} and body \mathcal{B} are close but not in contact. The $d_1(x_B, \mathcal{A})$ measure define the gap between the bodies at point x_B . b) Body \mathcal{B} have penetrated the body \mathcal{A} . The $d_1(x_B, \mathcal{A})$ measure gives the penetration at point x_B	44

LIST OF FIGURES

2.14	The contact surface projection over the target surface: a) Target discretized area; b) contact discretized area; c) intersection of the projected surfaces.	45
2.15	Prediction-correction algorithm	48
125	3.1 MRI images in three breast configuration: first line- subject 1; second line- subject 2	56
	3.2 Breast tissues segmentation on the breast MRI of the second subject. Prone breast configuration. White-voxel belongs to breast tissue; blue - voxel don't belongs to fatty tissue	57
130	3.3 Registered MRI images: first line- subject 1; second line- subject 2; first column - prone configuration versus supine; second column - supine tilted versus supine	58
	3.4 Anatomical planes and nominal Cartesian axis directions.	59
135	3.5 3D geometries generation. a) MR images; b) segmeted image; c) corresponding 3D geometries	60
	3.6 Finite elements mesh quality.	61
	3.7 Finite elements mesh components. The tissues components are cropped for visualization purposes.	61
140	3.8 Fixed point type iterative algorithm for stress-free geometry approximation. D_i - mean node to node distance over the active nodes at iteration i , G - gravity force	62
	3.9 Finite elements mesh boundaries	63
	3.10 Tissues accumulation on the sternum line with excessive sliding	64
	3.11 Components of the finite elements mesh.	65
145	3.12 Process to estimate optimal material parameters	66
	3.13 Process to estimate optimal material parameters	67
150	3.14 First column: relation between maximal and mean nodes displacement and the equivalent Young's modulus variation for different tissues. Second column: rate and cumulative change rate of node displacement in function of quivalent Young's modulus	69
	3.15 Hausdorff distance on the skin surface over the constitutive parameters space	70
155	4.1 Three breast configurations: prone, supine and supine tilted. First line - MR images in 3 breast configurations. Second and third lines - point to node distance from simulated breast shape (surface mesh) to the measured one (black grid lines).	74
	5.1 left: crano-caudal breast compression; righ - mediolateral oblique breast compression	79
	5.2 A typeical breast compression cycle. Reproduced from Groot et al. (2015)	80
160	5.3 Characteristic breast flattening curve as function of the applied force. Reproduced from Groot et al. (2015)	81

LIST OF FIGURES

5.4	Breast compression between the paddle (up) and the receiver (down): a Rigid paddle; b)Flex paddle with flexion angle α	82
165	6.1 Microclcification distribution over the smallest breast volume ($d = 10mm$): a)axial view, b) sagittal view.	84
170	6.2 Resulting breast thickness for a given compression force	85
	6.3 Stress, strain and contact pressure distribution for the first subject	87
	6.4 Stress, strain and contact pressure distribution for the second subject	88
	6.5 Breast nominal thickness (BNT), average glandular dose (AGD), signal-to-noise-ratio (SNR) and signal-difference-to-noise (SDNR) for both volunteers and both compression paddle types	89

List of Tables

175	2.1	Surface interaction models and corresponding mechanical behaviors	42
	2.2	Material properties for adipose and glandular tissues.	50
	2.3	Breast biomechanical models	54
	3.1	Minimal and maximal value (in kPa) for Youngs modulus.	68
	6.1	Compression force and breast thickness for both subjects for a cranio-caudal mammogram	84

¹⁸⁰ List of Symbols

λ	Young's moduli
\mathcal{B}	Body
μ	shear moduli
ν	Poisson ratio
¹⁸⁵ Ω	Domain occupied by the body
Ω_0	Reference body configuration
Ω_1	Current or analyzed body configuration
E_{xx}	Youngs's moduli of the material xx
$E_{xx}^{l/r}$	Young's modulus of the material xx for the left/right breast
¹⁹⁰ F	Deformation gradient
J	Jacobian determinant of the deformation gradient tensor
l	body stretch
m	Body mass
p	Particle or material point
¹⁹⁵ u	Particle displacement
X	Point position on the reference configuration
x	Point position on the current configuration
AGD	Average Glandular Dose
CC	Cranial-Caudal view

LIST OF TABLES

- 200 FDA Food and Drug Administration
FE Finite Element
FFDM Full Field Digital Mammography
GBM generalized momentum balance
ILC Invasive lobular carcinoma
205 IQ Image Quality
K Bulk moduli
LIQ Lower Inner Quadrant
LOQ Lower Outer Quadrant
MLO Mediolateral-Oblique view
210 MRI Magnetic Resonance Imaging
PDE partial differential equations
RF Radio-Frequency waves
SWE Shear-Wave Elastography
UIQ Upper Inner Quadrant
215 UOQ Upper Outer Quadrant
US Ultrasound

Part I

Introduction

²²⁰ General Problem statement

Today, mammography is the primary imaging modality for breast cancer screening and plays an important role in cancer diagnosis. Subtle soft-tissue findings and microcalcifications that may represent early breast cancer are visualized by means of X-rays images. After investigation, the abnormal findings are taken in charge for further evaluation. A standard mammographic protocol always includes breast compression prior to image acquisition. Women breast is compressed between two plates until a nearly uniform breast thickness is obtained. The breast flattening improves diagnostic image quality¹ and reduces the absorbed dose of ionizing photons². However, the discomfort and pain produced by this procedure sometimes might deter women from attending breast screening by mammography³. Fleming et al⁴ show in a study of 2500 women that 15% of those who skipped the second appointment cited an unpleasant or painful first mammogram. Nowadays, the European Commission recommends a force standardized breast compression, i.e. the compression stops at a level of force just below the subjects pain threshold or to the maximum setting of the machine (not to exceed 200 N). Some research⁵ indicates that with a reduced level of compression (10N vs 30N), 24% of women did not experience a difference in breast thickness. If breast thickness is not reduced when compression force is applied, then discomfort is increased with no benefit in image quality. An important improvement concerning the patient comfort could be achieved with the emergence of Full-Field Digital Mammography (FFDM). Several studies have shown that digital mammography is better in terms of image quality^{6,7} and radiation dose^{2,8} than FilmScreen Mammography (FSM). Therefore, there is an opportunity to leverage the potential of the recent imaging technologies to investigate alternative breast compression techniques, considering the patient comfort in addition to an improved image quality and a reduced ionizing radiation dose. The aim of this work is to develop and evaluate a biomechanical Finite Element (FE) breast model allowing to investigate alternative breast compression strategies.

Technical approach

Several studies showed that, the pain experienced by women during the mammographic exam depends on psychologic factor (Aro et al., 1996) (technician behavior, patient anxiety), sociologic factors (Dullum et al., 2000) (ethnicity, education level) as well as physiologic (Poulos et al., 2003) factors (compression level, breast size). Here, the psychologic and sociologic factors are neglected. The study focuses on physiological factors as the compression force or structural specifications of the compression paddle to characterize the patient comfort.

Thesis overview

Key contributions

260 **Software**

Ethics

Part II

Background

Clinical background

1.1 Introduction

In France, in 2012, approximately 1.2 million new cases were diagnosed, and 400,000 women died from breast cancer. Early detection of cancer is a major condition to a fast and full recovery from breast cancer. Today, mammography is by far the primary imaging modality for breast cancer screening and plays an important role in cancer diagnosis. However, frequently this experience is described by women as unpleasant and sometimes painful.

The aim of this chapter is to provide the required clinical background on breast cancer screening and diagnosis for a good understanding of the global aim and relevance of the present work.

First the breast evolution from early to the adult ages is described, with a detailed characterization of internal and external adult breast structures. To explain the intra-individual variation of breast mechanical and structural properties, the hormonal changes during the menstrual cycle, pregnancy or menopause are presented. Next the cancer edogenesis is described and the most common types are characterized. Finally, different modalities for breast imaging are presented with their underlying technical principals as well as their utilization and relevance for breast cancer regular screening.

1.2 Breast anatomy

Internal and external breast structures will be repeatedly referenced in the following work, therefore their detailed description including mechanical properties and their localization is needed. Although the breast anatomy seems to be simple and easy to understand, a detailed analysis of breast embryogenesis is requested then the supporting breast tissues are studied. As we intend to build a breast biomechanical model, these structures are of high interests.

1.2.1 Breast embryogenesis

The breast is a modified skin gland which starts to develop at the embryonic stage from the epidermis and dermis. During the sixth fetal month, from 12 to 20 solid cords of epithelial cells are growing down into the dermis (fig. 1.1.a-b). Later, these cords evolve into lactiferous ducts and alveoli (fig. 1.1.c-d). Thus, near birth, a simple network of branching ducts is already developed in the pectoral area (Skandalakis, 2009).

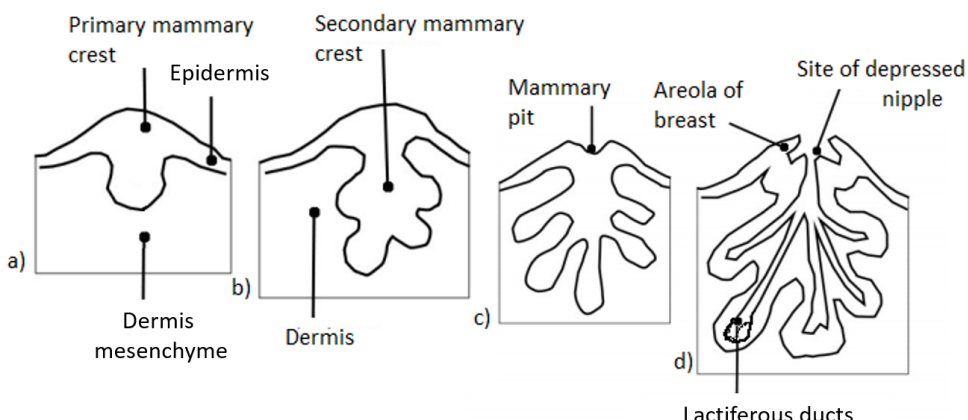


Figure 1.1: Breast embryogenesis: stages of formation pf the duct system. the ectoderm is responsible for duct system and alveoli, the mesenchyme is responsible for the connective tissue and vessels (Skandalakis, 2009).

The glandular lobs, generally remain underdeveloped until puberty (13 to 18 years). Under hormonal stimulation, the breast buds due to the development of the mammary glands and increased deposition of fatty tissues, becoming palpable discs beneath the nipple. The ducts grow into the soft tissues and the lobular differentiation begins (Kopans, 2007).

Kopans (2007) analyzed breast development sequence in the subcutaneous tissues. According to the authors the evolution of breast within the fascial system is unclear, with two possible evolution paths:

- (A) The superficial fascia splits in two layers forming the deep and the superficial fascia layers. The mammary glands appears between these two layers (fig.1.2.A).

- 305 (B) The elongating ducts retracts the superficial fascia. The mammary glands is enveloped by the superficial fascia (fig.1.2.B)

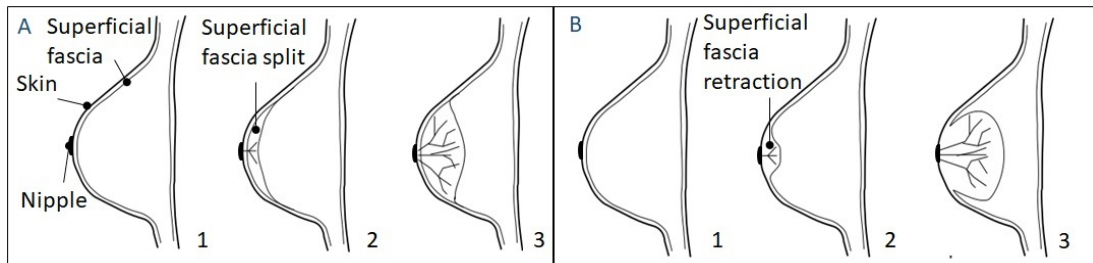


Figure 1.2: Breast development sequence in the subcutaneous tissues. A Mammary bud development by sleeting the superficial fascia in 2 layers. B Mammary bud development by fascia retracting, reproduced from (Kopans, 2007)

1.2.2 Breast Appearance

In order to describe the breast appearance, several notions for localization into the breast volume and its vicinity are defined. Usually, the breast volume is divided into four quadrants: upper outer quadrant (UOQ), upper inner quadrant (UIQ), lower outer quadrant (LOQ), lower inner quadrant (LIQ)(see fig.1.3). However, the anatomical structures surrounding the breast are localized using the anatomical landmarks as: the inframammary fold, the clavicle, the sternal angle, the sternal line, the costal margin and the axilla.

Starting with the Warner Brother Corset Company in 1935 the underwear industry 310 introduced a new unit to measure the breast volume, the cup. The cup size is computed using a relation between the circumference of the chest at the level of the nipples and the torso width (Pechter, 1998).

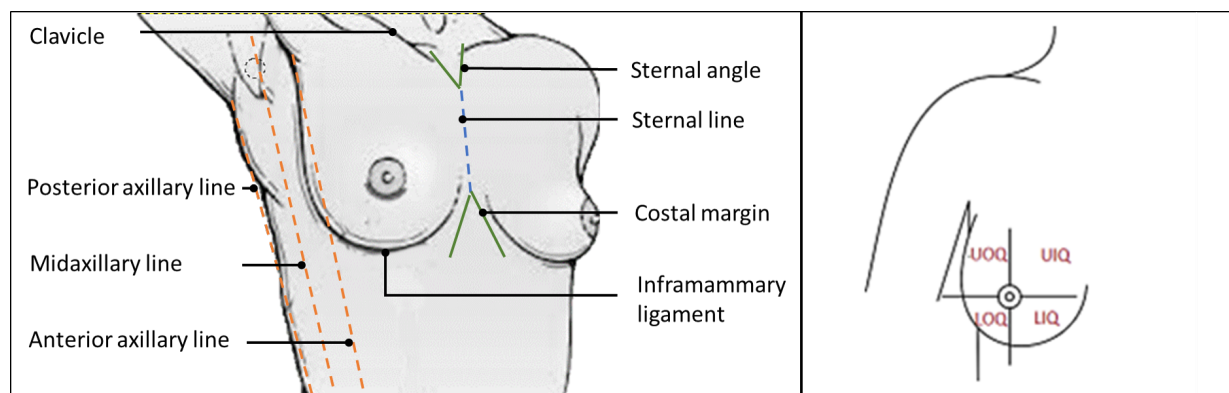


Figure 1.3: Left: thorax landmarks; Right: four breast quadrants

Anatomically, the adult breast is localized on top of the ribcage, between the clavicle superiorly and costal margin inferiorly. Its traverse boundaries are defined from the sternal

320 line medially to the midaxillary line laterally (fig.1.3). The intra-individual asymmetry is considered as a normality for the young and the adult breast (between left and right breast). The breast shape and contour are influenced by (Mugea and Shiffman, 2014):

- 325
- The volume of mammary gland in each breast quadrants.
 - The amount of the subcutaneous and intra-lobular fat.
 - The body contour of the chest wall.
 - The muscular covering and thickness.
 - The thickness and elasticity of the skin.

330 Anthropomorphic characteristics of women breast were studied almost for the aim of cosmetic and reconstructive surgery. Vandeput and Nelissen (2002) measured distances between anatomical landmarks of the thorax of 973 women with aesthetically near-perfect breasts. The authors proposed different relations as guidelines to compute the recommended breast size parameters (nipple-mid clavicle distance, nipple inframammary fold distance) as a relation of body parameters (body height, torso width). In their study, a poor correlation was found between body height or weight and breast volume. Contrariwise 335 a high correlation was found between the nipple to the inframammary fold distance or the nipple to the mid clavicle distance and the thorax width. Catanuto et al. (2008) mentioned that the breast shape after surgery cannot be predicted by volumetric measurements only; they have proposed additional measures (surface, distance or angles) permitting to characterize unambiguously the breast shape. According to the authors, the curvature of the 340 thoracic surface is the most relevant parameter to evaluate the outcome of a reconstructive breast surgery.

1.2.3 Internal structure

345 Breast heterogeneous structure includes a mixture of parenchyma and adipose tissue (fig.1.4). The breast parenchyma consists of glandular components, lymphatic network and blood vessels (Clemente, 2011). Skin, Cooper's ligaments and fascias are the supporting system of the breast; their interconnection and intersections with the pectoral muscle fix and support the breast soft tissues (Mugea and Shiffman, 2014).

350 **Adipose tissue** is the predominant tissue of the breast that fills up depressions between the deep and superficial fascia. In the intra-fascial space, adipose tissue surrounds and is dispersed among the glandular structures. Fat properties and its spatial distribution gives the breast a soft consistency. The main aim of this tissue is to protect the lobes and lactiferous ducts.

355 **Glandular tissue** is represented by breast lobes. A healthy female breast is made up of 12-20 lobes. They are distributed centrally and laterally within the breast. The total amount of glandular tissue depends on the hormonal fluctuation, age and physical state. Mammary ducts arise from the lobes as branches and connect them to the female nipple.

There are about 10 duct systems with a tree-like structure in each breast that carry the milk from the lobes to the nipple. The dark area of skin surrounding the nipple is called the areola. Huang et al. (2011) have studied the breast shape and fibro-glandular distribution
 360 using dedicated breast CT images. This study shows that the glandular tissues is situated in the central portion of the breast. In prone position about 60 % of glandular tissues is located near to the nipple. A mean percentage of glandular tissue was computed by Yaffe et al. (2009), the values varied from 13.7% to 25.6 % within different groups. They also mentioned a drop in glandular fraction with the advancing age.

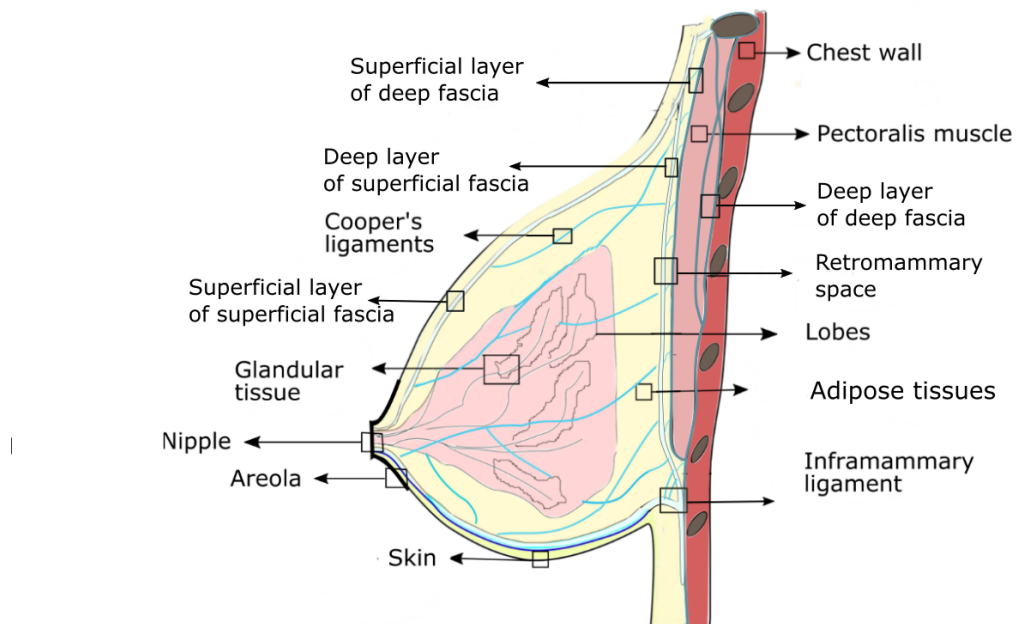


Figure 1.4: Breast anatomy

365

A layer of adipose tissue and connective fascia separates the breast from the pectoral muscle forming a retro-mammary fat space.

The **skin** is the covering breast layer which provides protection and receives sensory stimuli from the external environment. It is a heterogeneous organ composed of 3 layers
 370 (see fig. 1.5 , (Kanitakis, 2002)): epidermis (dead cells) mainly composed of keratin, dermis composed of collagen and elastin fibers in a viscous matrix made of water and glycoproteins and hypodermis, mainly composed of adipocytes cells.

The breast skin thickness varies from breast base to the nipple between $\sim 2\text{ mm}$ and $\sim 0.5\text{ mm}$. At the nipple areola region, the skin thickness measure $4\text{-}5\text{ mm}$. (Andolina and
 375 Lillé, 2011). Sutradhar and Miller (2013) studied the breast skin thickness of 16 different sectors radially oriented around the nipple. The thickness range proposed by the authors varies between 0.83mm and 2.35mm with a mean of $1.55 \pm 0.04\text{mm}$. According to this

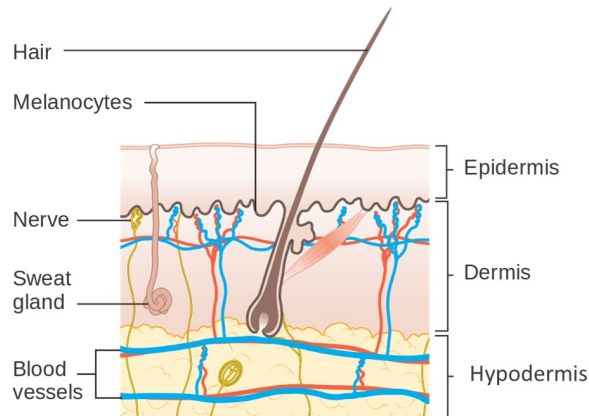


Figure 1.5: Skin anatomy

study the skin thickness varies as follows: the lateral region thickness is the thinnest among all the breast regions followed by superior/inferior and medial region; there is no significant
 380 difference between the inferior and superior breast regions; in the radially exterior region, the skin is thicker than in the radially interior region (close to the nipple). Ulger et al. (2003) found that, during the breast puberty, that is associated with an increase of the breast volume, the skin thickness decreases in all regions.

Connective tissue is represented by Cooper's ligaments and fascial system. The breast
 385 fascial system is composed of deep fascia and superficial fascia. During puberty, breast is growing and the superficial fascia divides in two layers: the deep layer of the superficial fascia and the superficial layer of the superficial fascia (Kopans, 2007). Cooper's ligaments run throughout the breast tissue parenchyma from the deep layer of the superficial fascia beneath the breast to the superficial layer of superficial fascia where they are fixed (fig.
 390 1.4). Because they are not taut, these ligaments allow the natural motion of the breast (Clemente, 2011). Between the deep layer of the superficial fascia and the superficial layer of the deep fascia, a layer of connective loose tissue forms the retro-mammary space, allowing the breast tissue to slide over the chest (Mugea and Shiffman, 2014). In regions where the superficial fascia meets the deep fascia, suspension ligaments are created. One
 395 of these ligaments is situated at the level of the sixth and seventh ribs and is called the **inframammary ligament** (Bayati and Seckel, 1995). It evolves into the **deep lateral ligament** and the **deep cranial ligament** that are respectively attached to the axillary fascia and to the clavicle. The second meeting point of the 2 fascias is situated on the sternal line and is called the **deep medial ligament**. On the upper pole of the breast, near the
 400 second rib space, the deep fascia tightly connects with the 2 layers of the superficial fascia, here the third meeting point is created. The three ligaments are 3D structures, evolving from pectoral muscle toward the nipple underlying the skin surface.

The existence, the topography, and the thickness of the membranous layers of superficial fascia have been studied in various regions of the body (Abu-Hijleh et al., 2006). According
 405 to the authors, the thickness of these superficial layers in both superior and inferior breast

regions is equal to $88.12 \pm 7.70\mu\text{m}$ and $140.27 \pm 11.03\mu\text{m}$ respectively.

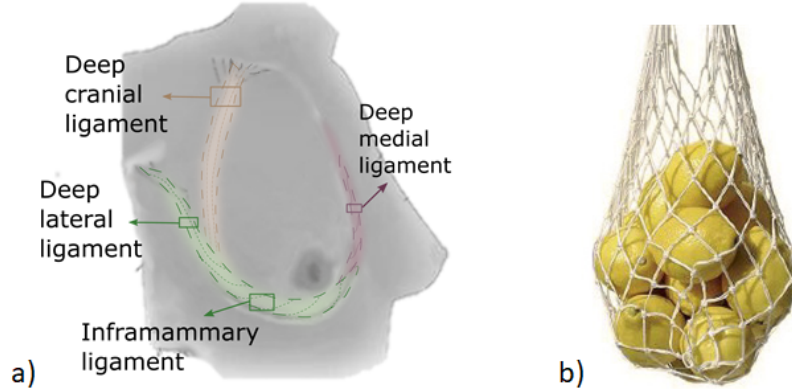


Figure 1.6: Suspensory ligaments

The lymphatic system is a vessel network which insures the transportation of white blood cells from tissues into the bloodstream. The majority of intramammary nodes are associated with the upper outer breast tissue and the lower outer part of the breast (Kopans, 2007). All intramammary lymph nodes are in the lateral half of the breast along the margin of the breast parenchyma. The lymphatic drainage of the breast extends from the subareolar plexus deep to and around the nipple (fig.1.7).

The blood supply from the breast comes primarily from the internal mammary artery named successively subclavian, axillary, and brachial arteries (fig.1.7), from which lateral and internal thoracic arteries runs underneath the main breast tissue.

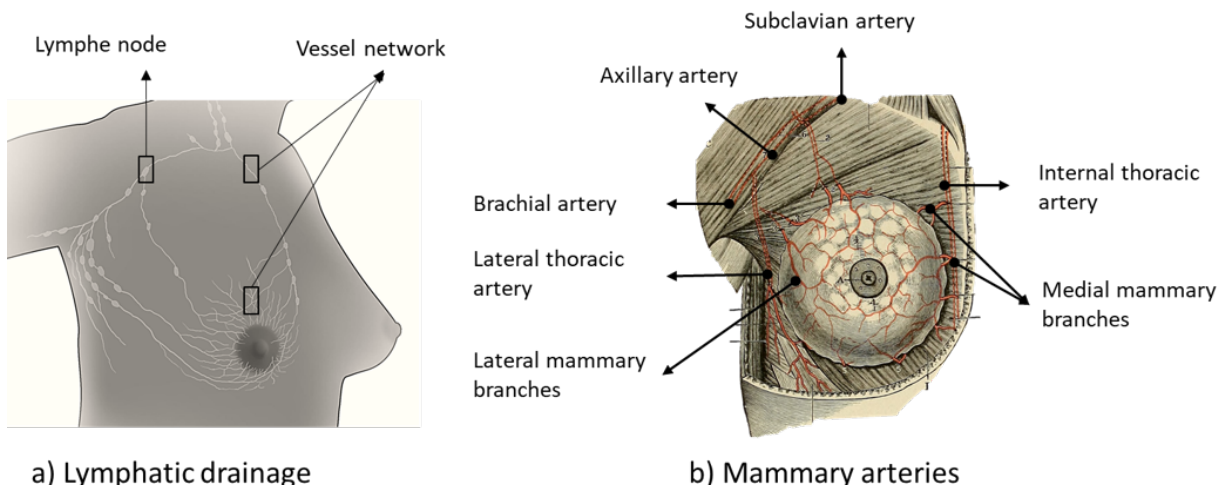


Figure 1.7: Lymphatic system and Mammary Arteries for adult female breast

1.2.4 Adult breast texture changes

The female breast undergoes substantial changes during the lifetime. Most changes are caused by hormones and by woman's physiological condition. Important changes in female breast stiffness and composition occur during the menstrual cycle, pregnancy and menopause.

There are 3 important changes during the menstrual cycle caused by hormonal changes (Andolina and Lillé, 2011). During the first phase, the estrogen (female hormones) diffusion stimulates the epithelial cell multiplication and the enlargement of ductal structures. Next, during ovulation, epithelial cells begin to grow in the lobule due to progesterone hormones; an increase in blood flow is also noticed. In the last phase, the ductal structures and the lobes support an involution and a regression process. It must be mentioned that not all lobules regress, therefore during menstrual cycle new lobules can be created. The work by Lorenzen et al. (2003) showed that during the premenstrual phase the stiffness of fibro-glandular tissue and glandular tissue can change by 30% and 14 % respectively. They also have shown that in the middle of the menstrual cycle, the parenchyma volume increases of 38% and the water content by 24.5%.

During pregnancy, under the influence of estrogen and progesterone, the breast enlarges in volume and density, the veins dilate and the ratio of parenchyma tissues increases. When lactation is weaned the breast returns to the pre-pregnancy state, and the atrophy of glandular, ductal, and stromal elements atrophy is observed (Pandya and Moore, 2011).

The menopausal breast contains a larger fraction of fatty tissues and reduce the number of ductal and lobular elements. During the first four years after menopause the breast is the subject of an atrophy process. The atrophy begins medially and posteriorly, then laterally, working its way to the nipple (Andolina and Lillé, 2011). In this period the breast loses progressively fat and stoma tissues resulting in breast shrinkage and loss off contours.

The breast support matrix can be stretched and attenuated by weight changes occurring during pregnancy and can relax with aging. These various changes can result in an excess of breast mobility over the chest and ptosis.

1.3 Breast Cancer

The first written description of breast cancer was on ancient Egyptian papyrus. At that time the treatment was considered futile and the woman was left without any medical assistance. Ancient Greeks, thought that the breast cancer was caused by an excess of black bile. It was thought that the monthly menstrual flow naturally relieved women of this excess, which explained why breast cancer was more common after menopause (Andolina and Lillé, 2011).

Nowadays, several researches (Pike et al., 1993; Martin, 2017) have shown that the cancer is always caused by damages to a cell's DNA . The initiation of the mutagenic process that may result in various genetic errors requires cell division. A factor that increase cell proliferation will increase also the risk of cancer. The woman hormones,

455 estrogen and progesterone, appear to impact the breast cell division rate (Ciocca and Fanelli, 1997; Fanelli et al., 1996), which explain the high rates of breast cancer in women (more than 99% of breast cancer occurs in women). The risks of developing a cancer is increased by various factors like age, genetics, family history or life style. According to (Martin, 2017) the breast cancer risk factors can be explained by woman exposure to the
460 ovarian hormones during her lifetime.

The breast cancer is the second most frequent type of cancer and is the leading cause of death within women with cancer diagnosis (SPF, 2016). The Foundation for Medical Research (FRM, 2017) estimates the risk of developing breast cancer for french women as 1 in 8 with more than 47% of cases diagnosed on women within 65 years old. According to
465 the French Public Health Agency SPF (2016) the incidence of breast cancer has increased by 138% between 1980 and 2005. In United Kingdom and United States by the year 2000 the death rate from breast cancer was reduced by almost 20% and in 2005 was down by 25% (Peto et al., 2000). This significant improvement was attributable to the rise in the life expectancy and the upgrowth of screening technologies.

470 **1.3.1 Cancer classification**

The breast cancer type is determined by the specific cells that are affected. When a woman is developing a breast cancer, more frequently the primary tumor is developed in the epithelial cells, this type of tumor is called carcinomas. The primary tumor can also start in cell from other tissues such as muscle, fat or connective tissues. These types of
475 tumors are called sarcomas, phyllodes, Paget disease and angiosarcomas but they are much rarer ACS (2017).

The carcinomas are then classified based on their location and how far the cancerous cell have spread. When the cancerous cells remain within the milk ducts or lobules, the cancer is classified as a non-invasive cancer. Otherwise, when the malignant cancerous cells
480 break through normal breast tissue barriers and spread out through other body organs, they are classified as invasive cancer (Andolina and Lillé, 2011). The most common types of carcinomas characterized by their location are: ductal carcinoma and lobular carcinoma.

The invasive ductal carcinoma starts in the epithelial cells that line the milk ducts, whereas the invasive lobular carcinoma starts in the lobules. Both evolve through the
485 surrounding tissues and may widespread to the other organs through the bloodstream and lymph nodes (metastasize).

Although the non-invasive carcinomas are not malignant, they have a 40% chance to change to invasive carcinomas over a 30-year period. The non-invasive ductal carcinomas start and stay inside the milk duct. The non-invasive lobular carcinoma overgrowth the
490 normal breast cells and stay inside the lobule.

Invasive lobular carcinoma (ILC) may be harder to detect on physical exam as well as imaging, like mammograms, than invasive ductal carcinoma. And compared to other kinds of invasive carcinomas, about 1 in 5 women with ILC might have cancer in both breasts. Non-invasive ductal carcinoma is the more commonly detected form, making up
495 4% of symptomatic cancers and 20% of the cancer detected during a screening program.

Its presence may be indicated on X-ray mammogram by microcalcifications (ACS, 2017).

1.3.2 Breast cancer screening

Early detection remains the primary defense available to prevent the development of breast cancer. The early detection consists of regular screening test aimed to find breast cancer before any symptoms can develop. The principal benefit of the regular screening is the potential to prevent the premature and often prolonged, painful death of the individual. Studies have shown that regular mammographic screening resulted in a 63% reduction in breast carcinoma death among women who actually underwent screening (Tabár et al., 2001). In 2012, the review of the UK screening program (NHSBSP, 2012) showed that it prevented 1300 deaths from breast cancer a year.

Secondary benefits include a reduction in the trauma of treating earlier-stage lesions. Indeed, earlier found invasive carcinoma respond better to treatment which means that the patient may avoid having a mastectomy or a chemotherapy.

Various worldwide countries have adopted organized breast screening examination programs. Depending on the regional statistics and the estimated risk factors (age group, breast density, family history etc) the population is invited to participate to a free screening examination. In 1994, the French National Authority for Health approved a national screening program (FNAH, 2016). Since then, every woman within 50 and 74 years old, is invited one in two years for a clinical exam and a mammography.

The individuals who are suspected of having breast cancer, will have additional diagnostic tests as: diagnostic mammography, ultrasound (US), Magnetic Resonance Imaging (MRI), biopsy, blood test etc. The diagnostic test help not only to confirm or to infirm the screening results, but also, in case of positive test, to determine the stage and the type of the breast cancer.

520 1.4 Medical Imaging

Medical images are the technique used in modern medicine to achieve information on human body internal structures or internal tissues properties. This information is then processed and analyzed in order to diagnose, monitor, or treat medical conditions. This technology encompasses different imaging modalities and processes, each with their own advantages and disadvantages.

1.4.1 X-ray mammography

X-ray mammography is a type of medical imaging that uses x-rays to capture images of the internal structures of the breast (FDA definition). In digital mammography (also known as Full Field Digital Mammography, FFDM) x-rays are beamed through the breast to an image receptor (fig.1.8). A scanner converts x-ray to digital information. The

mammography can be used to detect parenchymal distortion, asymmetry, masses and microcalcifications within the breast.

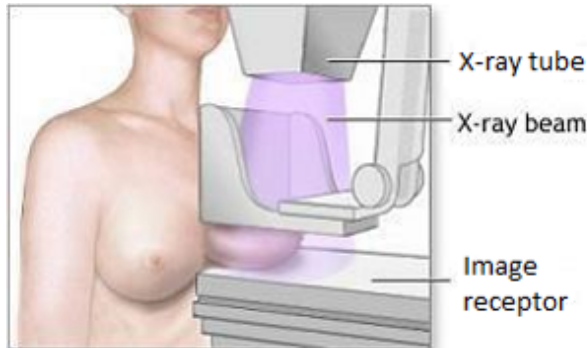


Figure 1.8: Mammographyc exam

A standard mammographic protocol always includes breast compression prior to image acquisition. Women breast is compressed between two plates until a nearly uniform breast thickness is obtained. Nowadays, the European Commission recommends a force stand-
535 arized breast compression, i.e. the compression stops at a level of force just below the subjects pain threshold or to the maximum setting of the machine (not to exceed 200 N). Historically, mammographic systems used fin films to display breast internal structures, thus the compression was needed in order to insure a uniform exposure over the breast
540 volume. With digital mammography, the exposure variation could be corrected, however the breast compression is still indispensable for many reasons: to hold the breast away from the chest wall; to reduce the blur due to physical motion; to reduce the absorbed dose of ionizing photons; to separate overlapping structures; to reduce image degrading scatter; to press breast structures closer to the detector (Kopans, 2007).

545 Screening mammography typically involves taking two views of the breast, from above (cranial-caudal view, CC) and from an oblique or angled view (mediolateral-oblique, MLO). The two views are complementary. The MLO view covers more tissue and provide better visualization of the upper juxtathoracic part of the breast. The CC-view suffers less from overlapping dense tissues and provide a better visualization on the central part of the breast
550 (Chan et al., 1987). Further compression or magnified view may be needed for diagnostic mammography.

Studies from different countries have assessed mammography sensitivity and specificity: the obtained sensitivities range between 81 and 88 %, and the specificities between 90 and 98 % (Kemp Jacobsen et al., 2015; Hofvind et al., 2012). The mammography sensitiv-
555 ity is mostly affected by dense breasts. A dense breast is a breast which proportion of the fibroglandular tissues exceed greatly the one of fatty tissues. Fatty tissues are radio- graphically translucent, high intensity signal appear on the mammographic images as dark areas. Meanwhile, the fibroglandular tissues and breast cancers tend to absorb the x-rays photons, therefore they will appear as white areas. The lack of contrast between the cancer
560 and background on white areas will make the detection more difficult.

1.4.2 Ultrasounds

Breast ultrasound uses high-frequency sound waves to image the tissues. The ultrasound technician put gel on the skin above the area of interest and moves the sound-emitting probe over the skin. The emitted waves are bounced by the breast soft tissues. The probe picks up the resulting waves and transformed them into a 2D images.

For asymptomatic women, a careful investigation of lateral and profound breast tissues is needed to identify the suspicious legions. The limited field of view of the ultrasound image prevents from seeing abnormalities that lie deeper in the breast. Consequently, the ultrasounds are not sufficient for regular screening and are used to complement other screening tests. However, it is widely used to investigate suspicious legions found within mammography, clinical or self-examinations. The ultrasound is particularly effective in differentiating between cysts and cancers, but have a low sensitivity for microcalcification detection which are the most common feature of tissue around a tumor. The ultrasound can also be used for differential diagnosis, local staging and interventions guidance.

Ultrasound elastography is a sonographic imaging technique combining the ultrasound technology with the basic physical principles of elastography. Elastography assesses tissue deformability by providing information on the tissues elasticity. It consists of either an image of strain in response to force or an image of estimated elastic moduli.

Shear-wave elastography (SWE) uses a focused pulse of ultrasound generated by the probe to induce soft tissues deformation. The tissues elasticity is assessed either by directly measuring soft tissues deformation or by measuring the speed of shear wave propagation. The combination of SWE with conventional ultrasound increases the diagnostic performance for breast lesions, compared with conventional ultrasound alone (Youk et al., 2017). Elastography serves as a complementary tool to differentiate between benign and malignant lesions by providing information about the lesion stiffness(Itoh et al., 2006; Olgun et al., 2014)

1.4.3 Magnetic resonance imaging

Magnetic resonance imaging is a noninvasive procedure for studying internal structure of the body that cannot be properly seen through normal X-rays (example: dense breasts). It employs radio-frequency(RF) waves and intense magnetic fields to excite hydrogen atoms. Body parts that contain hydrogen atoms (e.g. in water) are thus visible within fine details. The quality of the image produced by MRI techniques depends, in part, on the strength of the received signal. For higher image quality, it is optimal to use an independent RF receiving coil placed in close proximity to the region of interest. For breast imaging, dedicated breast MRI coils can be used. The patient is placed in prone position with the breast inside the coil and both arms by the sides of the body.

For breast cancer imaging, a contrast agent is employed to enhance highly vascularized regions. Then the cancerous tumor develops, new vascularizations are created on the direct surrounding to provide oxygen. Thus, the lesions are visualized due to their uptake of contrast agent. Contrast enhanced MRI is used as a screening modality for women with

high risk of cancer.

Low specificity and high cost of MRI restricted its use in a routine screening (Peters et al., 2008). However, it is increasingly used for high-risk groups and for lesions that are difficult to detect with mammography or ultrasounds tests.

605 1.5 Conclusion

Today, mammography is by far the primary imaging modality for breast cancer screening and plays an important role in cancer diagnosis. Ultrasounds and Magnetic Resonance Imaging are complementary imaging techniques used mostly for dense breasts and high-risk women.

610 In order to obtain an accurate reading, the mammography machine needs to compress the breasts. The discomfort and pain produced by breast compression might deter women from attending breast screening by mammography (Aro et al., 1999; Fleming et al., 2013). In a study by (Dullum et al., 2000) more than 50% of attendants ($N= 1800$) mentioned from moderate to extreme physical discomfort. It has been reported that the fear for pain itself
615 can already be a reason to avoid getting the first mammogram (Andrews, 2001), and that 15% of those who skipped the second appointment cited as the main cause an unpleasant or painful first mammogram(Fleming et al., 2013; Whelehan et al., 2013). Postpone the mammographic exam can lead to delayed breast cancer diagnoses and worse prognoses (expected outcomes) for some women.

620 The direct cause of pain in mammography is the flattening of the breast which is directly linked to the applied compression force. Latest researches indicate that with a reduced level of compression (10N vs 30N), 24% of women did not experience a difference in breast thickness. If breast thickness is not reduced when compression force is applied, then discomfort is increased with no benefit in image quality or mean average dose. Therefore, a
625 detailed study on alternative breast compression techniques considering the patient comfort in addition to the image quality and ionizing radiation dose is needed.

630 The aim of this work is to provide a simulation framework capable to assess the patient physical comfort, as well as the corresponding image quality and mean average glandular dose for breast compression with different paddles designs. The developed numerical methods would serve to build an optimal compression paddle in terms latter listed parameters, and therefore increase the adherence to breast cancer screening.

635 In this scope, a subject-specific biomechanical Finite Element (FE) model is developed and evaluated on real deformation measured on MR images. The proposed model is then used to compute the tissues deformation associated to breast compression during mammography. The resulting internal stress/strain intensities are then used as a first estimate of the physical comfort. The deformed geometry is the subject of a Monte-Carlo image simulation allowing to assess the image quality (IQ) and average glandular dose (AGD).

Part III

Biomechanical breast modeling

Background and state of the art

2.1 Introduction

Finite elements models are widely used to estimate body parts deformation under pre-defined boundary conditions. Several biomechanical models of the breast were recently developed providing physics-based predictions of tissue motion and internal stress and strain intensity. In our work, we assume that the strain intensity obtained during the tissues deformation may be correlated with the patient discomfort. Thus, a biomechanical model obtained from the patient's MRI volume can be subsequently used to mimic breast compression during the mammographic acquisition. The resulting tissues strain cartography can be used as a first quantification of the patient inconfort.

This chapter provide theoretical background on continuous mechanic theory applied to soft tissues modeling. The principle of finite elements theory is defined including solid bodies and contact mechanics. A review of the existing biomechanical breast model is given describing the main challenges in the field and the proposed solution. These works proved the core foundation for the next developed patient specific breast model.

2.2 Continuous mechanics

Continuum mechanics is a branch of mechanics that deals with the analysis of the kinematics and the mechanical behavior of materials modeled as a continuous mass. Continuum mechanics is based on the continuum hypothesis: the matter is continuously distributed throughout the space occupied by the matter. The basis for the hypothesis is how physical quantities, as for example pressure, temperature, and velocity, are measured macroscopically.

In this section the continuous mechanis theory applied to solids bodys was discribed using the following sources: Belytschko et al. (2013); Abeyaratne (2012).

2.2.1 Deformation and strain

Continuous mechanics is the mathematical description of how physical objects that occur in nature respond to the application of forces.

A **body** is the mathematical abstraction of an *object* and is defined by its geometric and constitutive properties. At a macroscopic level, a solid *object* is described as homogeneous and continuous body, i.e. the substance of the object has a unique composition and completely fills the space it occupies thus, ignoring the granular (atomic) nature of matter. In continuous mechanics, a body \mathcal{B} is composed of a set of **particles** p (or material points). Each particle is located at some defined **point** x in three dimensional space. The set of all the points in space, corresponding to the locations of all the particles, is the **domain** Ω occupied by the body in a given configuration, here also named *geometry*. A particular body can change its configuration and therefore the occupied region in the space when exposed to some external stimuli like force, pressure or heat.

The **configuration** of a body is defined as a one-to-one mapping between the particle p and position x , $\Omega_0 = \chi_0(\mathcal{B})$ (see figure 2.1). To describe the solid's respond to external stimuli one needs to know the changes in geometrical characteristics between at least two configurations: the configuration that one wishes to analyze Ω_1 , and the **reference configuration** relative to which the changes are to be measured Ω_0 . Here, see figure 2.1, the mappings χ_0 and χ_1 take $p \rightarrow X$ and $p \rightarrow x$, thus X and x are the positions of particle p in the two configurations under consideration.

Frequently, the reference configuration is fixed for a given study and is chosen arbitrary in a the most convenient way among all the configurations that the body can sustain.

The **deformation** of the body from the reference configuration Ω_0 is characterized by the next defined mapping Φ :

$$x = \Phi(X) = \chi_1(\chi_0^{-1}(X)), \quad \text{where } X \in \Omega_0 \text{ and } x \in \Omega_1 \quad (2.1)$$

The **displacement** u of a particle is the difference between its position in the analyzed configuration (or current configuration) and its position in the reference configuration.

$$u(X) = \Phi(X) - X \quad (2.2)$$

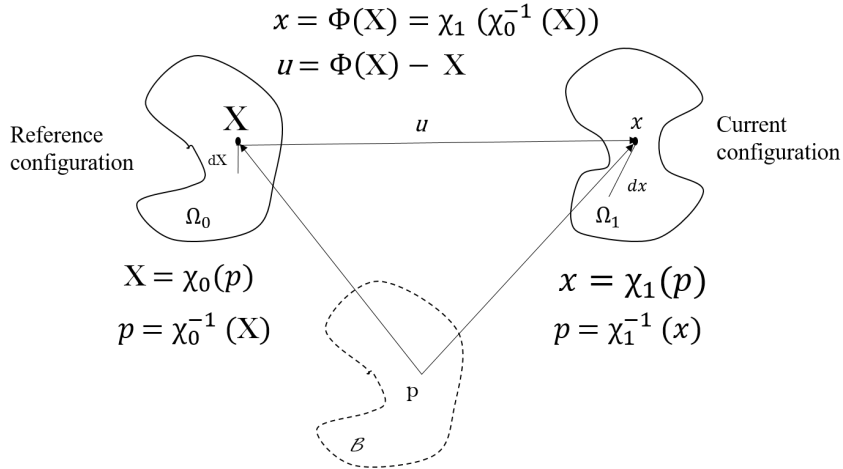


Figure 2.1: The position of a particle in the reference and current body configurations.

Suppose that $G(\Omega_1)$ is the value of some extensive physical property associated with the body \mathcal{B} in the current configuration (such as the body mass m). There exists a density $g(x)$ such that:

$$G(\Omega_1) = \int_{\Omega_1} g(x) dv$$

where dv is the volume of the material element. Thus, the property $G(\Omega_1)$ is related to the body while the density $g(x)$ is related to the position of the body particle.

Eulerian and Lagrangian formulations

There are two classical techniques used to describe the body physical characteristics depending on the choice of independent variables. Some physical characteristics, such as mass density, can be defined for each individual particle. In such cases, the body characteristics are defined by the function

$$m = \mathcal{M}(p)$$

for all $p \in \mathcal{B}$. Here the coordinate system remains consistent and moves with the particle. Therefore, the coordinates of both, the particle and the attached variable, do not change along the deformation. A particle is an abstract entity and cannot be used in numerical calculations, thus it is described by its location in reference configuration $p = \chi_0^{-1}(X)$.

$$m = \mathcal{M}(p) = \mathcal{M}(\chi_0^{-1}(X))$$

We call X Lagrangian or material coordinates and their application is called Lagrangian or material description.
695

Instead of defining body characteristics as a function of body particles, one can define it directly as a function of particle location in current configuration by using the relation

$x = \chi_1(p)$, and therefore

$$m = \tilde{\mathcal{M}}(x) = \mathcal{M}(\chi_1^{-1}(x))$$

Here the coordinate system is fixed and the particles coordinate are changing. Therefore, the position of particle and any related quantity changes during the deformation. We call x Eulerian or spatial coordinates and their application is called Eulerian or spatial description.

These approaches are distinguished by three important aspects: the mesh description, the stress tensor and momentum equilibrium and the strain measure. The advantages and drawback of these two formulations will be discussed later in this chapter. Further, only Lagrangian formulation is used to describe the continuous deformation of soft tissues.

Deformation gradient

In mathematical formulation the deformation gradient tensor F is the Jacobian matrix of the deformation $\Phi(X)$:

$$F = \frac{\partial \Phi(X)}{\partial X} = \frac{\partial x}{\partial X} \quad (2.3)$$

Considering infinitesimal quantities, the deformation gradient relates the segment dX in the reference configuration to the corresponding deformed segment dx in the current configuration (Figure 2.1)

$$dx = F \cdot dX. \quad (2.4)$$

In addition to the mapping of such vectors, the deformation gradient tensor allows also the mapping of differential volumes as:

$$dv = \det(F)dV = JdV \quad (2.5)$$

The Jacobian determinant of the deformation gradient tensor J is a measure of the volume variation during the deformation. It can be used to relate extensive physical properties in the current and reference configurations:

$$\int_{\Omega_1} g(x)dv = \int_{\Omega_0} g(\Phi(X))JdV \quad (2.6)$$

Decomposition of the deformation gradient tensor into rotation and stretch

The deformation gradient tensor F completely characterizes the body deformation in the vicinity of a particle p . This deformation consists of a rigid body rotation and body *stretch* (see fig. 2.2). As dX and dx are differential segments, the map F is not affected by rigid-body translations.

Generally, the body stretch is defined as the ratio of the deformed line elements to the length of the corresponding undeformed line element

$$l = \frac{|dx|}{|dX|}, \quad (2.7)$$

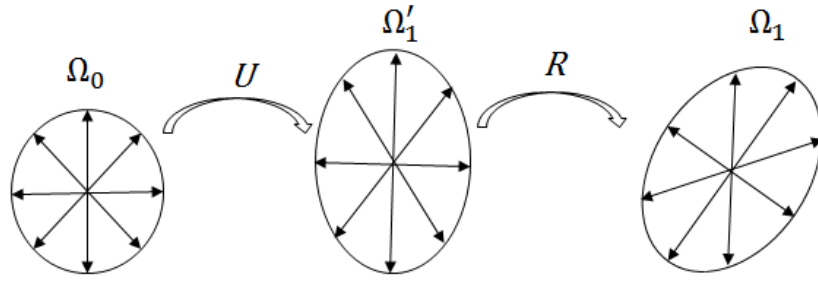


Figure 2.2: Decomposition by rotation and a stretch of a material particle.

and consists locally on three mutually orthogonal stretches named **the principal stretches**.

According to the polar decomposition theorem, the deformation tensor can be written as the product of a proper orthogonal tensor R representing the rotational part, and a symmetric positive defined tensor U representing the body distortion.
725

where U and R are given by the relations $U = (F^T \cdot F)^{\frac{1}{2}}$ and $R = F \cdot U^{-1}$. The essential property of tensor U is that it is symmetric and positive, therefor it has three real positive eigenvalues $\lambda_1, \lambda_2, \lambda_3$ and a corresponding triplet of orthonormal eigenvectors r_1, r_2, r_3 . Thus then an infinitesimal segment dx is stretched by the tensor U , the segment is distorted
730 in the principal direction of U by amounts of the corresponding eigenvalues of U .

The tensor U is also called the **right stretch tensor**. Since there is a one-to-one relation between U and U^2 , for the simplification of numerical calculus the stretch tensor can be replaced by the **Green deformation tensor** $C = F^T \cdot F$.

There are three particular functions of C called the principal invariants.

$$I_1(C) = \text{tr}C, \quad I_2(C) = \frac{1}{2} [\text{tr}C^2 - (\text{tr}C)^2], \quad I_3(C) = \det(C). \quad (2.9)$$

These functions are related to the three principal stretches by the next relations:
735

$$I_1(C) = \lambda_1^2 + \lambda_2^2 + \lambda_3^2, \quad I_2(C) = \lambda_1^2\lambda_2^2 + \lambda_2^2\lambda_3^2 + \lambda_3^2\lambda_1^2, \quad I_3(C) = \lambda_1^2\lambda_2^2\lambda_3^2 \quad (2.10)$$

The essential property of the principal invariants is that they don't change under coordinate transformations for a given body configuration. Their use to compute the body stretch will be an essential part of constitutive modeling, because the behavior of a material should not depend on the coordinate system.

It can be also shown that:
740

$$\det(C - \mu I) = -\mu^3 + I_1(C)\mu^2 - I_2(C)\mu + I_3(C) \quad (2.11)$$

Strain measures

Referring to small deformations, the engineering nominal strain is defined as the ratio of the change in length of the deformed line element to the length of the corresponding undeformed line element:

$$\epsilon = \frac{dx - dX}{dX} \quad (2.12)$$

When the body is not deformed, the deformation gradient F and therefore the right stretch tensor U is equal to identity tensor I . The strain in such a case is equal to zero.

For most biological soft tissues, large deformation has to be considered. In that case, the previously defined strain is no more applicable. For large deformations, a measure of strain can be any monotonically increasing function related to stretch in a one-to-one manner, this function has to vanish in the reference configuration.

In orthogonal coordinate system, an admissible function is

$$f(x) = \frac{1}{m}(x^m - 1) \text{ for } (m \neq 0) \text{ and } \ln(x) \text{ for } (m = 0) \quad (2.13)$$

For $m = 0$ the function represents the Hencky strain tensor,

$$E = \ln(U), \quad (2.14)$$

for $m = 1$ the function represents the Biot strain tensor

$$E = U - I, \quad (2.15)$$

and for $m = 2$ the Green-Lagrangian stain tensor:

$$E = \frac{1}{2}(U^2 - I) = \frac{1}{2}(C - I) \quad (2.16)$$

The Green-Lagrangian tensor is commonly used in practice as, by using the relation 2.11, it can be computed without prior knowledge of the eigenvectors of the Green deformation tensor C .

2.2.2 Stress measures

760 Body and contact forces

Generally, forces are categorized as internal and external forces. An **external force** is a force caused by an external agent outside of the system, and contrariwise an **internal force** is a force exchanged by the particle in the system. The external forces, in turn, are categorized in **body forces** (acting at the distance) and **contact forces** (acting on the body surface). The relation between body forces per unit undeformed volume $\tilde{b}(X)$ (Lagrangian coordinates) and body forces per unit deformed volume $b(x)$ is given by the following relation:

$$\tilde{b} = \frac{dv}{dV} b = Jb. \quad (2.17)$$

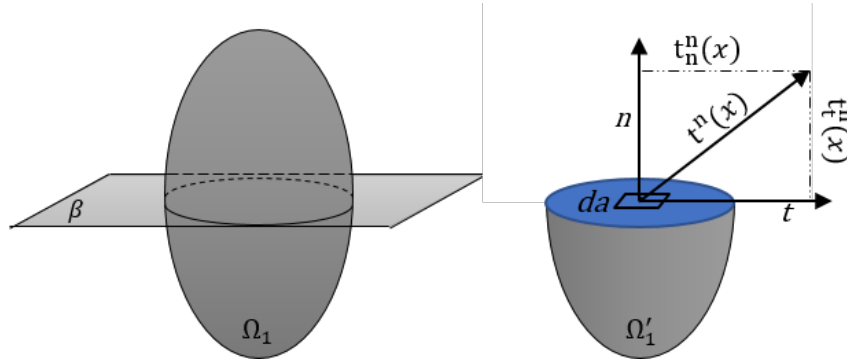


Figure 2.3: True stress vector $t^n(x)$ at point x on the fictitious surface created by the cutting plane β of normal \vec{n} passing through the point x .

The contact forces can act on the external surface of the body or on a imaginary internal surface enclosing a volume element (Fig. 2.3). In general terms, the stress (or the **traction vector**) $t^n(x)$ is defined as contact force per unit area da in the limit as $da \rightarrow 0$.
 770 Therefore $t^n(x)$ varies from point to point in intensity and orientation depending on the $da(n)$ orientation. The stress vector projection on normal axis n defines the **normal stress vector** and its projection on the tangential axis define the **shear stress vector**.

The stress on the boundary $\partial\Omega_1$ of the region occupied by the body is applied by
 775 external forces through physical contacts along the boundary. When formulating and solving a boundary-value problem, this stress defines the boundary conditions.

Cauchy's lemma

Cauchy's lemma states that traction vectors acting on opposite sides of a surface are equal and opposite.

$$t^{-n}(x) = -t^n(x) \quad (2.18)$$

780 Cauchy's Law

Cauchys law states that there exists a Cauchy stress tensor σ which maps linearly the normal to a surface to the stress vector acting on that surface, according to the next relation

$$t^n = \sigma \cdot n \quad \text{where} \quad t_i^n = \sigma_{i,j} n_j \quad (2.19)$$

When large deformations are considered, the reference and current configurations of
 785 the body are significantly different and a clear distinction has to be made between them. The traction vector t^n is defined in Eulerian coordinates (body current configuration) and is also called the **true stress**. Accordingly, the Cauchy stress tensor σ is called the true stress tensor.

The definition of any measure with respect to the deformed configuration is less practical
 790 as it is usually unknown a priori. For the simplification of mathematical formulation, a

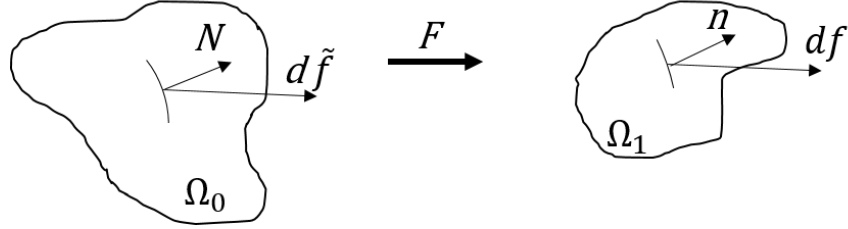


Figure 2.4: Deformation of area dA into area da . The force df acting on deformed area da and the pseudoforce $d\tilde{f}$ acting on undeformed area dA

new pseudostress is defined in the Lagrangian coordinate space named the **engineering stress**. The engineering stress has no physical meaning and has to be converted in to true stress for any interpretations.

Next, two pseudostress vectors are defined (Fig. 2.4):

- T^N defined as the contact force df per unit area dA in reference configuration.
- \tilde{T}^N defined as the contact pseudoforce $d\tilde{f}$ per unit area dA in reference configuration.

Accordingly, two pseudostress tensors are defined based on pseudostress vectors:

- $T^N = P \cdot N$, P is called **first Piola-Kirchhoff stress tensor**,
- $\tilde{T}^N = S \cdot N$, S is called **second Piola-Kirchhoff stress tensor**.

were N is the normal vector of unit area dA .

The three stress tensors are linked by the next relation

$$\sigma = J^{-1}F \cdot P = J^{-1}F \cdot S \cdot F^T \quad (2.20)$$

2.2.3 Conservation equations

Three conservation laws must be satisfied by physical system subject to any applied boundary conditions: **conservation of mass**, **conservation of linear momentum** and **conservation of angular momentum**. The resulting equations describe partially the mechanical behavior of a continuous body.

Conservation of mass

The mass m of a body with the density ρ , that infills the space region Ω_1 is given by :

$$m(\Omega) = \int_{\Omega} \rho(X) dV \quad (2.21)$$

The mass conservation law requires that the body mass remains constant throughout all possible body configurations. For a Lagrangian formulation, this results in a relation

between the body density in the reference configuration ρ_1 and the body density in the current configuration ρ .

$$\int_{\Omega_1} \rho_1 dv = \int_{\Omega_0} \rho_0 dV = const.$$

Using the relation 2.6 one can deduce that:

$$\int_{\Omega_0} (\rho_1 J - \rho_0) dv = 0 \quad and \quad \rho_1 J = \rho_0 \quad (2.22)$$

810 Conservation of the linear momentum

Assume that a body \mathcal{B} is defined on a arbitrary region Ω_0 with boundary Γ_0 , and is subjected to a body-force $\rho_0 b$ and the surface traction T^N . And let X be the particle location in the undeformed solid. The total force acting on the body \mathcal{B} is defined as:

$$f = \int_{\Omega_1} \rho_0 b(X) dV + \int_{\Gamma_0} T^N(X) dA \quad (2.23)$$

The conservation of the linear momentum requires that the total forces acting on the body to be equal to the time rate change of the linear momentum. In a static problem the time rate change of the linear momentum is neglected and thus an equilibrium equation is obtained.

$$\rho_0 b + \nabla_0 \cdot P = 0 \quad (2.24)$$

Where the P_{ji} are the components of first Piola-Kircchoff stress tensor. The equilibrium equation can be formulated in terms of the second Piola-Kircchoff stress tensor by using 2.20 relations.

Conservation of angular momentum

The conservation of angular momentum requires that the resultant momentum on any part of the body about a fixed point \mathcal{O} equals the rate of increasing of its angular momentum (about \mathcal{O}). For a static problem, the integral form of the conservation of angular momentum is defined as:

$$\int_{\Omega_0} X \times \rho_0 b(X) dV + \int_{\partial\Omega_0} X \times T^N(X) dA = 0 \quad (2.25)$$

The relation 2.25 requires that the second Piola-Kircchoff stress tensor is a symmetric tensor:

$$S = S^T \quad (2.26)$$

In summary, the conservation equations are fulfilled if and only if the following local conditions are fulfilled at each point in the body:

$$\rho_1 J = \rho_0, \quad \nabla_0 \cdot S \cdot F^T + \rho_0 b = 0, \quad S = S^T \quad (2.27)$$

830 with the traction on the surface related to the stress through $\tilde{T}^n = S \cdot N$. For the simplification of mathematical calculus, the constitutive equations are formulated in terms of the second Piola-Kircchof stress tensor using the relations 2.20.

2.2.4 Constitutive models

The constitutive models, called also material models, define the relation between stress and strain of a physical system under the action of external stimuli. It is almost impossible to define a universal material behavior capable to model the material response to all possible conditions. Thus, for a given material, several constitutive models can be defined depending on the studied characteristics.

Biological materials are classified into:

- *Isotropic or anisotropic materials*: in a isotropic (anisotropic) material the values of a property is constant (vary) with respect to the direction.
- *Compressible or incompressible materials*: in a compressible (incompressible) material the volume changes (remains constant) during the deformation and the density remains constant. For a incompressible material the Jacobian determinant of the deformation tensor J is equal to 1.
- *Homogeneous or heterogeneous materials* in a homogeneous (heterogeneous) material the values of a property is constant (vary) with respect to the position within the body.

Biological soft tissues are modeled using elastic materials model. The elasticity is the property of a solid material to return to its original size and shape when the influence of an external force is removed. In this case the strains are said to be reversible.

Considering small deformations, the stress-strain law of a linear material is given by the **Hook's law**

$$\sigma = \lambda \epsilon,$$

where the coefficient of proportionality λ is named **Young's moduli**.

Elastic materials may be defined also with a non-linear stress-strain relationship. In such cases the elastic moduli (λ) is defined in function of strain ϵ

$$\lambda = \frac{\partial \sigma}{\partial \epsilon} = f(\epsilon).$$

For example, for an elastic exponential material (Azar et al., 2002) the elastic moduli is computed using the function

$$f(\epsilon) = b e^{m\epsilon}, \quad (2.28)$$

where b and m are material parameters.

For large deformation the stress-strain relationship is deduced from a potential function. A **hyperelastic** material is an elastic material for which the work is independent of the deformation path. The material reversibility and path-independent behavior implies the absence of energy dissipation during the deformation. Thus there exist a **potential** function $W(E)$ such that

$$S = \frac{\partial W(E)}{\partial E} = 2 \frac{\partial \psi(C)}{\partial C}$$

Moreover, if the material is isotropic, the stored strain energy W of a hyperelastic material can be written as a function of principal invariants (I_1, I_2, I_3) of the Green deformation tensor C previously defined in equation 2.9.

⁸⁶⁰ We introduce below the most used potential functions for the characterization of biological soft tissues.

For the simplification of potential expressions, we define the first and the second deviatoric strain invariants:

$$\bar{I}_1 = \frac{I_1}{I_3^{2/3}}; \quad \bar{I}_2 = \frac{I_2}{I_3^{4/3}}$$

⁸⁶⁵ We also define the **Bulk moduli** as measure of a material's resistance to compression; the **shear moduli** as the ratio of shear stress to the shear strain; and the **Poisson ratio** as the ratio between longitudinal strain to the transverse strain describing the body shape change. For small deformation the Bulk moduli and shear moduli are linked to the Young's moduli and Poisson ratio by the next relations:

⁸⁷⁰
$$K = \frac{\lambda}{3(1-2\nu)} \text{ and } \mu = \frac{\lambda}{2(1+\nu)}$$

Neo-Hookean potential function

The Neo-Hookean (Treloar, 1943) law is an extension of the Hook's law to large deformations. The potential function is based only on the first invariant and is given by

$$W = \frac{\mu}{2}(\bar{I}_1 - 3) + \frac{K}{2}(J - 1)^2, \quad (2.29)$$

where μ and K are initial shear moduli and initial Bulk moduli respectively.

⁸⁷⁵

Mooney-Rivlin potential function

The potential function of a Mooney-Rivlin (Rivlin and Saunders, 1951) material is defined as:

$$W = \frac{\mu_1}{2}(\bar{I}_1 - 3) + \frac{\mu_2}{2}(\bar{I}_2 - 3) + \frac{K}{2}(J - 2)^2, \quad (2.30)$$

where the constants μ_1 and μ_2 describing the material properties are linked to the initial shear moduli $\mu = (\mu_1 + \mu_2)$. And the constant K is the initial Bulk moduli.

⁸⁸⁰

Gent potential function

The potential function of a Gent (Gent and Thomas, 1958) material model is defined as:

$$W = -\frac{\mu J_m}{2} \ln \left(1 - \frac{\bar{I}_1 - 3}{J_m} \right) + \frac{K}{2} \left(\frac{J^2 - 1}{2} - \ln J \right), \quad (2.31)$$

where μ and K constants are the initial shear moduli and the initial Bulk moduli respectively. And J_m is a parameter limiting the value of $(\bar{I}_1 - 3)$

Ogden model

- 885 The Ogden (Ogden, 1972) material model is based on the three principal stretches ($\lambda_1, \lambda_2, \lambda_3$) and $2N$ material constants, where N is the number of polynomials that constitute the potential function:

$$W = \sum_{i=1}^N \frac{\mu_i}{\alpha_i} (\lambda_1^{\alpha_i} + \lambda_2^{\alpha_i} + \lambda_3^{\alpha_i} - 3) + \sum_{k=1}^N \frac{K}{2} (J - 1)^{2k}, \quad (2.32)$$

where μ_i and α_i are material constants, and K is the Bulk moduli.

Yeoh model

- 890 The potential function of Yeoh (Yeoh, 1990) model is based on the first invariant:

$$W = \sum_{i=1}^N \mu_i (\bar{I}_1 - 3)^i + \sum_{k=1}^N \frac{K}{2} (J - 1)^{2k}, \quad (2.33)$$

where the μ_i are material constants and K is the Bulk moduli.

Governing equations of Lagrangian formulation

- We consider a body \mathcal{B} which occupies in the reference configuration the domain Ω_0 with a boundary Γ_0 . The governing equations for the mechanical behavior of a continuous body
895 are:

1. Conservation of mass $\rho_1 J = \rho_0$
2. Conservation of linear momentum $\nabla \cdot P + \rho b = 0$
3. Conservation of angular momentum $F \cdot P = P^T \cdot F^T$
4. Constitutive equations
- 900 5. Measure of strain $E = \frac{1}{2}(C - I)$
6. Boundary condition: $e_i \cdot N \cdot P = e_i \cdot \bar{t}$ on $\Gamma_0^{t_i}$
7. Internal continuity condition: $\llbracket e_i \cdot N \cdot P \rrbracket = 0$ on Γ_0^{int}

Where we note $\Gamma_0^{t_i}$ the set of prescribed traction \bar{t} on the body boundary Γ_0 ; and Γ_0^{int} is the union of all surfaces where the stresses are discontinuous in the body (material interfaces).
905

The momentum equation together with the traction boundary condition and interior traction continuity condition are called generalized momentum balance (GMB) .

2.3 Finite Element Discretization

In continuous mechanics the body deformation is expressed in terms of partial differential equations (PDE). For the majority of problems, the PDEs cannot be solved analytically, therefore approximation methods are developed. To this end, the finite element (FE) method has become the standard numerical calculation to compute such approximations. The computational domain, the unknown solution, and its partial derivatives are discretized, so as to obtain a set of algebraic equations for the function values at a finite number of discrete locations. The unknowns of the discrete problem are associated with a computational mesh which represents a subdivision of the domain Ω_0 into many small control volumes Ω_k

2.3.1 Eulerian and Lagrangian mesh description

The mesh description depends on the chosen independent variables (Eulerian or Lagrangian formulation). An Eulerian mesh formulation is usually used to solve problems linked to fluid like materials and a Lagrangian mesh for solid like materials. In an Eulerian mesh, the Eulerian coordinates of nodes are fixed (coincident with spatial points) and the material point change in time (see Figure 2.5.b). In this case the mesh has to be large enough to contain the body in its current configuration. Throughout the deformation, the material points will belong to different elements. On the contrary, in a Lagrangian mesh, the Lagrangian coordinates of nodes are time invariant, nodal trajectory corresponds with material points trajectory and no material passes between elements (see Figure 2.5.a).

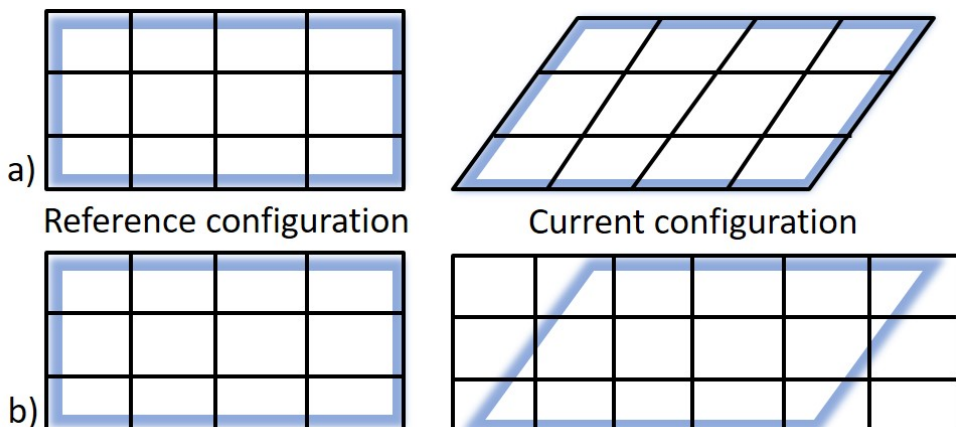


Figure 2.5: a) Lagrangian mesh formulation. b) Euler mesh formulation

In a Lagrangian mesh, the boundary and interface nodes remain coincident with body boundaries and material interfaces throughout the entire deformation. Thus, the boundary conditions are defined directly on the respective nodes. On the other hand, in a Eulerian mesh the boundary and interface conditions have to be defined on point which are not nodes. This implies important complications in multi-dimensional problems.

935 An important drawback of a Lagrangian mesh affect mainly the large deformation domain. As the nodes are coincident with the material points, the elements deform with materials. Therefore, the magnitude of deformation is limited because of element distortion. The limited distortion that most elements can sustain without performance degradation or failure is a important factor in nonlinear analysis with Lagrangian formulation.

2.3.2 Lagrangian mesh

940 The general approach of the FE method in Lagrangian formulation is shown in Fig. 2.6. First the momentum equations with given boundary conditions are multiplied by a set of appropriate test functions. The test functions have to satisfy all displacement boundary conditions and to be smooth enough so that all derivatives in momentum equations are well defined. Then performing an integration by parts, the week formulation of GMB is obtained, also called the principle of virtual work (Belytschko et al., 2013).

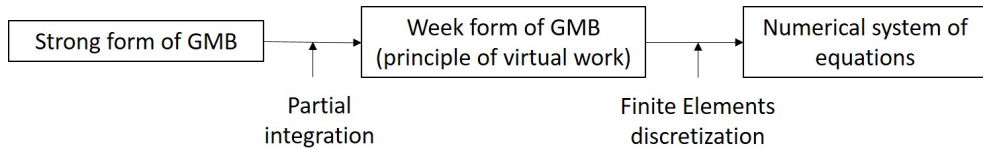


Figure 2.6: From strong formulation of the generalized momentum balance (GMB) to numerical equations.

945 The momentum equations and the traction boundary conditions, usually called the strong form, cannot be directly discretized by FE method. The strong formulation of the GMB equations impose the C_1 continuity conditions on the field variables. Therefore, the solution of this problem does not always exist. This is true especially in the case of complex domains with different material interfaces. In order to overcome these difficulties, 950 weak formulations are preferred. The week formulation of GMB reduces the continuity requirements thereby allowing the use of easy-to-construct and implement polynomials. Because of the reduction in the requirements of function smoothness, the weak forms never give an exact solution but one can obtain a relatively accurate solution with the discretization refinement.

955 From the week form of the GMB equations, the numerical system of equations is formulated by using finite elements interpolants for the mechanical displacement and the test functions. The whole domain is discretization into a number of smaller areas or volumes which are called **finite elements** and their assembly is called a **mesh**. Elements can be of various shapes (as shown in Figure 2.7.b), quadrilateral or triangular in two dimensions, 960 and tetrahedral or hexahedron in three-dimensions.

The mechanical displacement is approximated at the discretization points called finite element**nodes**. The nodes are at the vertices corners of the elements for a linear type, and at the vertices corners and midsides of the elements edges for a quadratic type (figure 2.7.b). The displacement of each point within an element is interpolated from the values

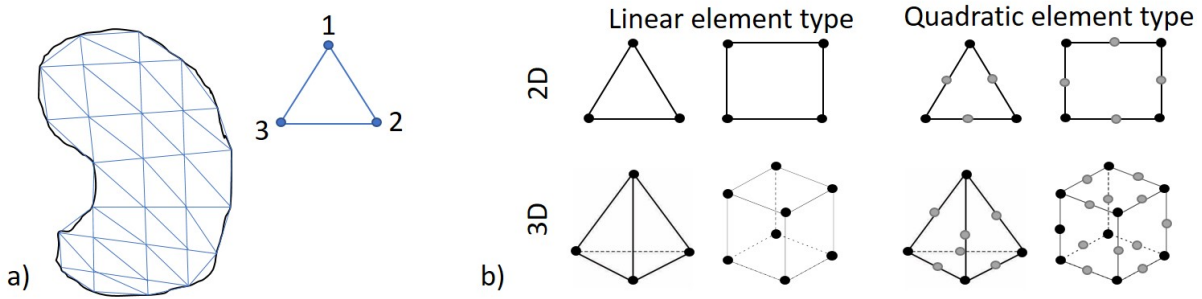


Figure 2.7: a) Discretization of a 2D domain with triangular finite elements (Lagrangian mesh). b) Different types of finite elements

965 of the displacements of the nodes of the element. In this way, the problem of finding the displacement of every point within the body is replaced by the problem of finding the displacements of a finite number of nodes.

As in a Lagrangian mesh the nodes are following the motions, for large deformation the finite elements can be highly distorted. Therefore, the elements shape quality is generally 970 checked all along the deformation process. Several shape parameters for each element type have been proposed such as: aspect ratio, maximum corner angle, Jacobian ratio, skewness, parallel deviation, warping factor. The acceptable limit values of these shape factors are proper to the elements types.

In the following, only the shape parameters of the linear triangular elements are presented 975 (ANSYS, 2017b).

Triangle aspect ratio

The element's shape aspect ratio is computed using only the vertices corner nodes of the element (Figure 2.8). First, two lines are created: one through a node (K) and the midpoint of the opposite edge (K'), the second through the midpoint of the others two edges (J' and I'). Then two rectangles are created, each rectangle have a pair of edges parallel to one of previously defined lines. The rectangle edges have to pass through the nodes and the triangle's edges midpoints. This construction is repeated for each triangle's node resulting in 6 rectangles. The aspect ratio of a rectangle is defined as the ratio between the longer and shorter side. Thus, the triangle's aspect ratio is defined as the maximal aspect ratio 985 over the 6 rectangles divided by squared root of 3.

The best possible aspect ratio is 1 and is represented by an equilateral triangle. An element with an aspect ratio larger than 20 is considered as bad aspect element, large aspect ratio may degrade solution performance.

Triangle maximum corner angle

990 The maximum corner angle is computed using nodes position in 3D space. The best possible maximum corner angle is 60° . An element having a maximal corner angle larger

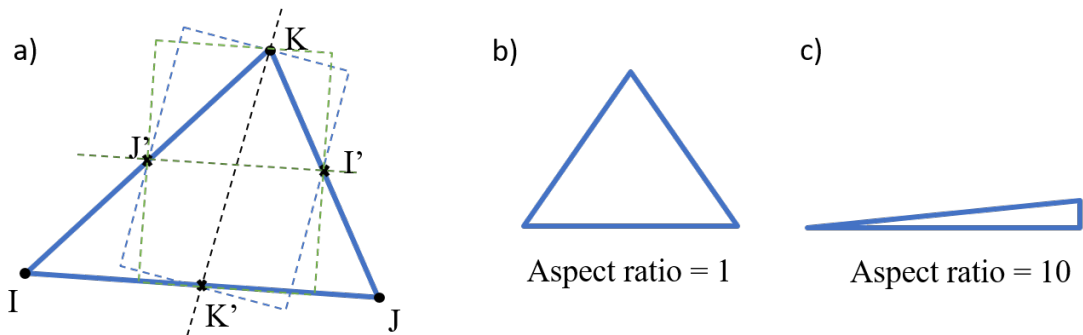


Figure 2.8: Computation of the aspect ratio for a triangle

than 165° is considered as bad shape element, large corner angles may degrade the solution performance. Figure 2.9 shows a triangle with a good (60°) and bad (165°) quality.

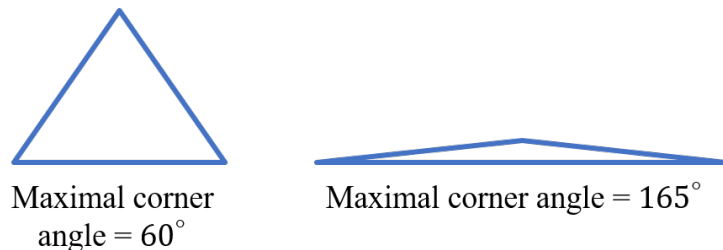


Figure 2.9: Example of triangles with different maximal corner angles.

The aspect ratio and the maximal corner deviation of a tetrahedra is computed using
995 the definition of the same measure on a triangle. The elements shape parameter is assigned
as the worst value over the triangles defined by the tetrahedra's faces and cross-sections.

Skewness

The skewness of a triangular element is computed using the equivalent volume deviation method. It is defined as the difference between the optimal and real cell size over the
1000 optimal cell size. The optimal size is the size of an equilateral cell with the same circum radius. According to its definition, the value of 0 indicates an ideal cell, from 0 to 0.75 the cell is considered to have a good quality, from 0.75 to 1 the cell is considered to have a bad quality and a value of 1 indicates a completely degenerated cell (Figure 2.10).

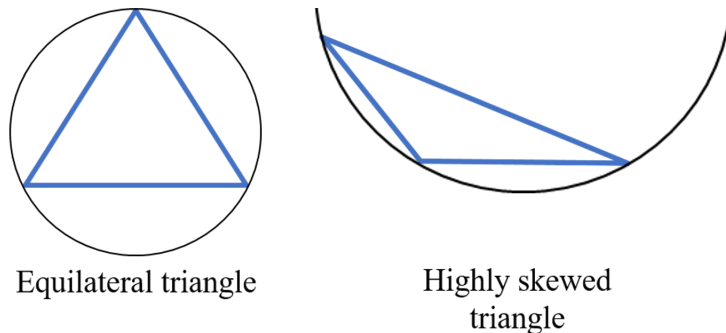


Figure 2.10: Example of triangles with different skewness with the corresponding circum radius.

2.4 Contact mechanics

- ¹⁰⁰⁵ In order to transfer the loads between elements, the nodes have to be connected together. If two bodies are separated with no common nodes, no interaction will occur during the deformation and the bodies will pass through each other. Here, an asymmetric surface-to-surface contact method is used to solve the multi-body interaction problems.

Let's consider two different bodies \mathcal{A} and \mathcal{B} and their occupied domains Ω_A and Ω_B with boundaries Γ_A and Γ_B respectively (see Figure 2.11). Also, we note Ω the domain of intersection of two bodies. The contact interface is the intersection of the surfaces of the two bodies:

$$\Gamma = \Gamma_A \cap \Gamma_B.$$

- ¹⁰¹⁰ The intersection consists of two surfaces, usually distinguished as **target** and **contact** surfaces. For an asymmetric contact each surface has a single designation and the choice of the surfaces type is made following these next guidelines (the target surface property are enumerated in their priority order):

- if the body \mathcal{A} is stiffer than the body \mathcal{B} , the surface Γ_A defines the target and Γ_B the contact surface;
- if Γ_A is a concave surface getting in contact with the convex surface Γ_B , the surface Γ_A defines the target and Γ_B the contact surface.
- if the surface Γ_A is larger than Γ_B , the surface Γ_A denotes the target and the Γ_B the contact surfaces.

- ¹⁰²⁰ For the following, we identify Γ_A as the target surface and Γ_B as the contact surface (Figure 2.11).

Sometimes, the asymmetric contact does not perform satisfactory results and a symmetric contact is needed. When defining a symmetric contact each surface coming in contact is designated to be both, contact and target surface type. Therefore, two set of contact

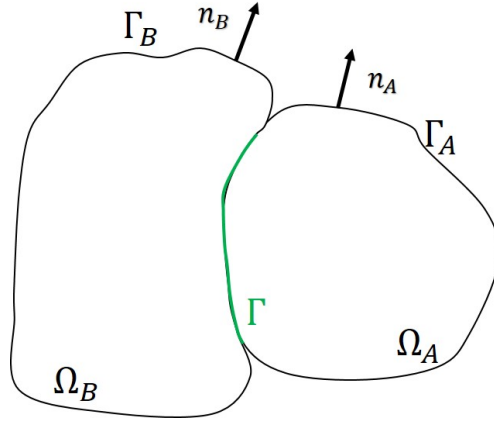


Figure 2.11: Multi-body contact problem.

1025 pairs are defined. The symmetric contact may be used then the distinction between the contact and the target surfaces is not clear or to reduce the contact penetration, however it usually results in a more time-consuming solution.

2.4.1 Contact interface equations

In the case of multi-body interaction, in addition to the standard mechanical governing 1030 equations, two more contact conditions have to be fulfilled: the two bodies cannot penetrate and the traction must satisfy momentum conservation on the contact interfaces.

Traction conditions

Traction conditions must follow the balance of momentum across the contact interface:

$$t_A + t_B = 0 \quad (2.34)$$

On the contact boundary surface Γ the traction vector is decomposed into its normal and 1035 tangential components:

$$t_A^n = t_A \cdot n_A, \quad t_B^n = t_B \cdot n_B$$

$$t_A^t = t_A - t_A^n n_A, \quad t_B^t = t_B - t_B^n n_B$$

Therefore the momentum balance requires:

$$t_A^n + t_B^n = 0, \quad t_A^t + t_B^t = 0 \quad (2.35)$$

Inter-penetrability condition

The bodies implied in a multi-body problem must fulfill the inter-penetrability condition:

$$\Omega_A \cap \Omega_B = 0 \quad (2.36)$$

Decomposing the displacement u into its normal and tangential components u^n and u^t
 1040 respectively the inter-penetrability condition can be written as:

$$t^n \leq 0, \quad u^n - gn_a \leq 0, \quad t^n(u^n - gn_a) = 0 \quad (2.37)$$

Where g is the gap between the two bodies and n_a is the normal to the target surface.

2.4.2 Surface interaction models

When two solid bodies are placed together under a nonzero normal force and acted upon by another with a tangential force, a **friction force** $f_{friction}$ tangential to the interface
 1045 and opposite to the applied force is created. Depending on whether the applied force can overcome the friction force opposing it, the bodies may or may not move relative to each other. The body motion along the interface is called **sliding**. The **sliding force**, $f_{sliding}$ is the applied tangential force which causes the sliding motion between the two bodies.

Determining whether relative motion will or will not occur requires balancing the involved forces.
 1050 According to the allowed relative body motion in tangential or normal directions, five types of surface interaction models are distinguished: bonded, rough, no-separation, frictional and frictionless. Table 2.1 resumes each corresponding mechanical behavior. If the body motion is not allowed in normal or tangential direction, once the bodies get in contact, the respective components of traction are equals ($t_A = t_B$), which means that, for a pure **bonded** contact, the two bodies are considered as a unique solid body.
 1055

Name	body motion in normal direction	body motion in tangential direction
Bonded	No	No
Rough	Yes	No, $f_{friction} \gg f_{sliding}$
No-separation	No	Yes, $f_{friction} = 0$
Frictionless	Yes	Yes, $f_{friction} = 0$
Frictional	Yes	Yes, if $f_{sliding} > f_{friction}$

Table 2.1: Surface interaction models and corresponding mechanical behaviors

The *frictional* contact behavior is defined using Coulomb friction law. For a continuous body the Coulomb friction model is applied at each point of the contact interface. Considering that bodies \mathcal{A} and \mathcal{B} which are in contact within the surface Γ , then for all
 1060 $x \in \Gamma$:

$$if \|t^t(x)\| < -\mu_f t^n(x), \quad \Delta u^t = 0 \quad (2.38)$$

$$if \ \|t^t(x)\| = -\mu_f t^n(x), \ \Delta u^t = -k(x)t^t(x), \ k(x) > 0 \quad (2.39)$$

Where μ_f is the material property named **friction coefficient**, Δu^t is the slip incremental in the tangential direction and $k(x)$ is a variable computed from the momentum equation. The condition 2.38 is known as the sticking condition: the tangential traction is less than the critical value, thus no sliding occurs. Reciprocally, condition 2.39 is called the sliding condition.

When a frictionless contact model is used, $\mu_f = 0$, the tangential tractions vanish completely: $t_A^t = t_B^t = 0$. On the contrary, when a rough contact is modeled, the friction coefficient μ_f is equal to infinity, so that the sticking condition is always fulfilled.

In practice, several contact models can be combined to model a physical contact between two bodies.

2.4.3 Contact formulation algorithm: Pure Penalty model

Pinball region

Contact formulation presents two primary difficulties from a computational point of view. First, the traction conditions have to be estimated for each considered frictional model. And second is the unpredictability of regions which will get in contact with each other during the deformation process.

The region of contact depends on materials properties and imposed boundary conditions; therefore, it is difficult to know a priori where the surfaces will be in contact. To formulate analytic equations, one has to know exactly the nodes involved in the contact process. Therefore, during body deformation, the program calculates if the contact is *opened* or *closed*. The status is defined using a sliding pinball (Figure 2.12). The pinball slides over the contact surface nodes and searches for the target surface. If the node to surface distance is smaller than the pinball radius, the contact is considered to be closed (Figure 2.12, green nodes) otherwise the contact is considered to be opened (Figure 2.12, gray nodes).

Gap and penetration measures

Let's consider a point x_B belonging to the body surface Γ_B and x_A the intersection point of the surface normal n_B with the surface Γ_A (Figure 2.13). The point to surface distance $d_1(x_B, \mathcal{A})$ is defined as:

$$d_1(x_B, \mathcal{A}) = \|x_B - x_A\| = \left[\sum_{i=1,2,3} (x_B^i - x_A^i)^2 \right]^{\frac{1}{2}} \quad (2.40)$$

If the intersection point x_A is located inside the pinball area, the node to surface distance define the amount of **gap** or **penetration** of the respective node (Figure 2.13).

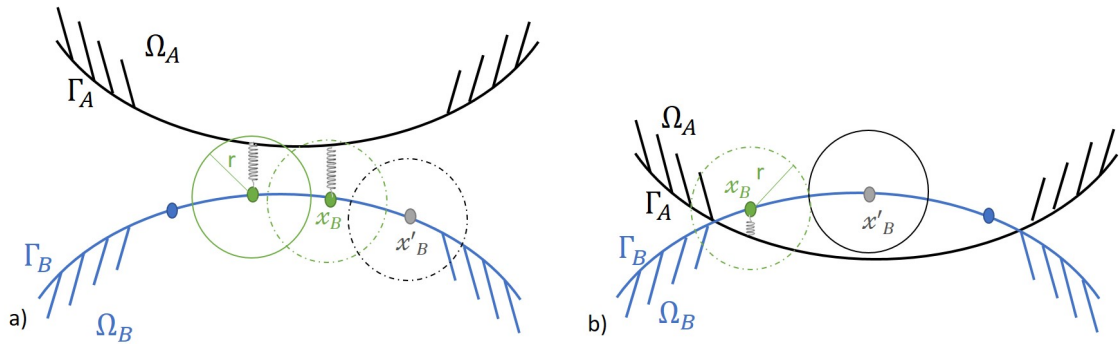


Figure 2.12: Contact status update using a pinball of radius r . Green nodes- updated nodes to closed contact status; gray nodes - updated nodes to open contact status; blue nodes- nodes which contact status need to be updated

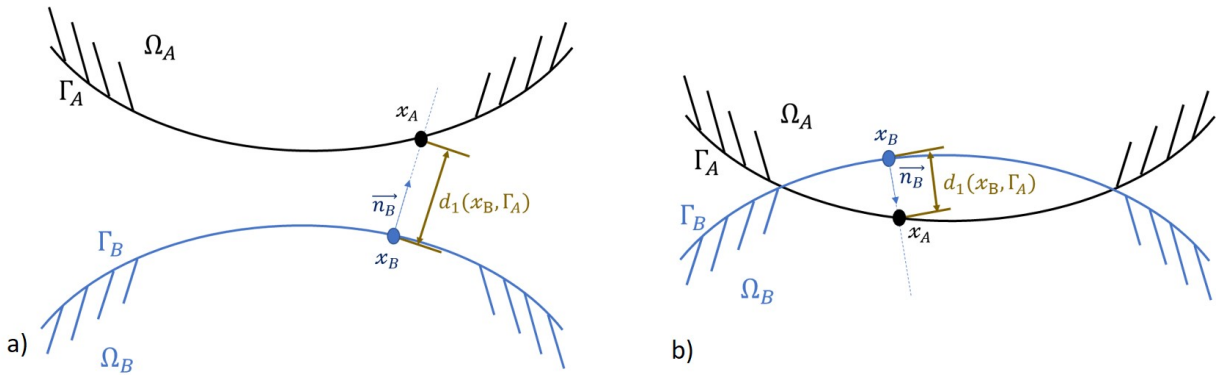


Figure 2.13: a) Body \mathcal{A} and body \mathcal{B} are close but not in contact. The $d_1(x_B, \mathcal{A})$ measure define the gap between the bodies at point x_B . b) Body \mathcal{B} have penetrated the body \mathcal{A} . The $d_1(x_B, \mathcal{A})$ measure gives the penetration at point x_B .

Computing the gap or penetration at single points increase numerical instabilities.
 1095 Therefore, in this work, the gap and penetration are computed in an averaged manner over
 the projected surface areas. Figure 2.14 show the projected surface areas (c) obtained by
 the intersection of the target surface areas (a) with the projected contact surface areas (b)
 over the target areas (a).

1100 The interested reader is referred to ANSYS contact technology guide (ANSYS, 2017a)
 for more details on the contact modeling.

Finite element mesh

For the finite element computation, contact and target surfaces have to be discretized with 2D linear or quadratic elements (Figure 2.7) consistent with the underling 3D element

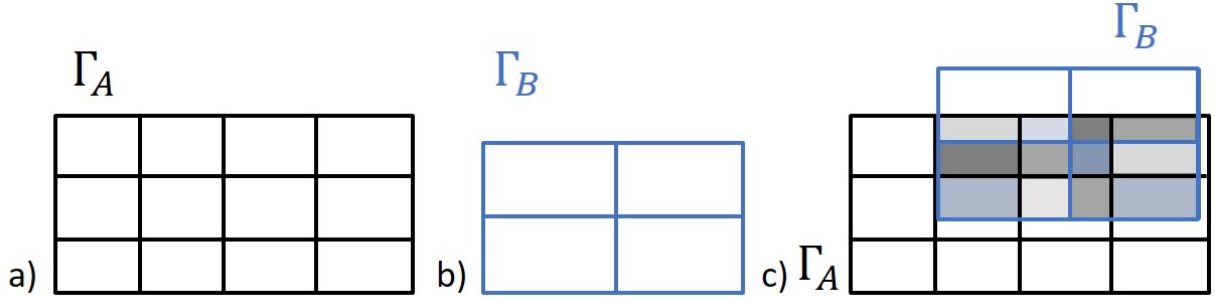


Figure 2.14: The contact surface projection over the target surface: a) Target discretized area; b) contact discretized area; c) intersection of the projected surfaces.

1105 mesh. The elements are named contact and target elements respectively. They have no material properties apart the friction coefficient μ_f . The stress-strain as well as the gap or penetration measures are computed for each mesh node of the discretized surface.

Pure Penalty method

1110 In this manuscript, one of the most popular mathematical expression of contact compatibility conditions is used, namely the penalty method. With such a method, additional contact properties are defined to manage contact behavior: a normal stiffness factor, opening stiffness factor, and a tangential stiffness factor. Such factors play an important role in the numerical computation but have no physical meaning.

1115 The penalty method uses a spring like relationship to introduce a force for all nodes pairs (contact-target) that are defined to be in closed contact (Figure 2.40). The contact force is computed using the following expression:

$$f_c = k_c d \quad (2.41)$$

1120 where d represents the penetration or gap amount and k_c is the normal stiffness factor or the opening stiffness factor respectively. The tangential stiffness factor works in the same way enforcing the responding frictional force. Even if physical contacting bodies do not interpenetrate ($d = 0$), some finite amount of penetration, $d > 0$, is required mathematically to maintain equilibrium.

1125 The biggest challenge here is that the magnitude of the stiffness contact factors is completely unknown beforehand. The contact force at each node have to be large enough to push the contact surface back to the target surface and eliminate unwanted penetration or gap. In the same time, if the contact force is too large, it pushes the contact surface far away from the pinball region causing error and solution instabilities.

2.5 Breast biomechanical model: overview

Biomechanical modelling of breast tissues has been widely investigated for various medical applications such as surgical procedure training, pre-operative planning, diagnosis and clinical biopsy, image guided surgery, image registration, and material parameter estimation
1130 (Table 2.3). For the last 20 years, several research groups have presented their breast models based on finite elements modeling. The complexity and relevance to breast anatomy of each model depend on the research purposes for which it was designed.

Several groups have proposed biomechanical breast models to register uncompressed volumetric breast data to the compressed one (Han et al., 2012; Ruiter et al., 2006; Sturgeon et al., 2016) or to compressed projection mammographic data (Kellner et al., 2007). Within this framework, the authors modeled the breast deformation from prone to compressed prone position assuming linear elastic materials, zero residual stress and Dirichlet boundary conditions. However, compression-like breast deformation is too limited to characterize
1140 global breast mechanics.

Applications such as image guided surgery or preoperative planning imply a wider range of deformations. Therefore biomechanical breast models capable of estimating gravity induced deformation between different body position were proposed, for example from supine to prone positions (named also multi-loading gravity simulations) (Gamage et al.,
1145 2012; Georgii et al., 2016; Eiben et al., 2016c). Considering the involved large deformation, these models need to be more accurate with respect to mechanical and anatomical breast properties. In this respect, a patient-specific model is needed considering more personalized boundary conditions, material models and a better representation of breast anatomy.

As described in Section 2.2, to build such a mechanical breast model, one need to provide the breast geometry in a **reference configuration**, the **constitutive models** of tissues composing the volume and the **boundary conditions**. The definition of all these variables has a significant impact on model accuracy.
1150

2.5.1 Breast reference configuration

A large number of existing patient specific models are using volumetric data from MR images Carter (2009b), Kellner et al. (2007), Conley et al. (2015) Eiben et al. (2016b), Martínez-Martínez et al. (2017) or CT images Palomar et al. (2008), Sturgeon et al. (2016)
1155 to design the breast geometry. During such exams, the acquired breast tissues are already deformed with deformation that significantly change breast geometries, for example if the patient is in a supine or in a prone position. Moreover, the deformed breast configurations include already the initial pre-stresses which are generally unknown and are extremely
1160 difficult to measure in clinical conditions.

To model the breast tissues deformation under gravity loading, the reference state is chosen to be the breast geometry in a stress-free configuration, i.e. without being deformed by any force, including gravity. The breast stress-free geometry is practically impossible to measure; therefore, several estimation methods have been proposed. The four most used
1165

ones are described below.

Inverse gravity

(Palomar et al., 2008; Sturgeon et al., 2016) used the inverse gravity method to estimate the stress-free geometry from the prone position measured during the exam. In their work, 1170 the authors just reversed the gravity effects without considering the initial stresses already included in the breast prone configuration. According to Eiben et al. (2014) the inverse gravity methods gives a poor approximation of the breast reference state and can be used only with small deformations or highly constrained models.

Breast neutral buoyancy configuration

1175 Assuming that breast density is equal to water density, Rajagopal et al. (2008) compute the breast stress-free configuration by imaging the breast immersed in water. Following the same physical assumptions, Kuhlmann et al. (2013) proposed to estimate the stress-free configuration by applying a hydro-static distributed load on the breast surface collected in a prone configuration. Even though the estimated geometries are accurate enough, these 1180 methods are time-consuming and is difficult to transpose in a clinical framework.

Prediction-correction iterative algorithm

The prediction-correction iterative method was first proposed by (Govindjee and Mihalic, 1998) and adapted later by Carter (2009b) and Eiben et al. (2014). The original method 1185 is based on the prediction-correction iterative scheme represented in Figure 2.15. The first approximation of the breast reference configuration is estimated by applying the inverse gravity method on the prone breast configuration (see above). Then, a numerical breast prone configuration is computed and compared to the corresponding measured one. The difference between the two prone geometries (The measured one and the simulated one) is used to update the reference breast configuration. The process is repeated until the 1190 convergence is achieved (i.e. then the difference is minimal). These methods were validated using the neutral buoyancy breast shape.

Inverse FE algorithm

Pathmanathan et al. (2008) and later Vavourakis et al. (2016) proposed an analytic computation of the breast reference state by reparametrizing the equilibrium equation and 1195 by solving a finite element formulation of the inverse motion. The model provides good estimates of breast reference configurations but needs large numerical resources. Eiben et al. (2014) showed that the prediction-correction iterative algorithm and the inverse FE algorithm are similar in terms of resulting accuracy.

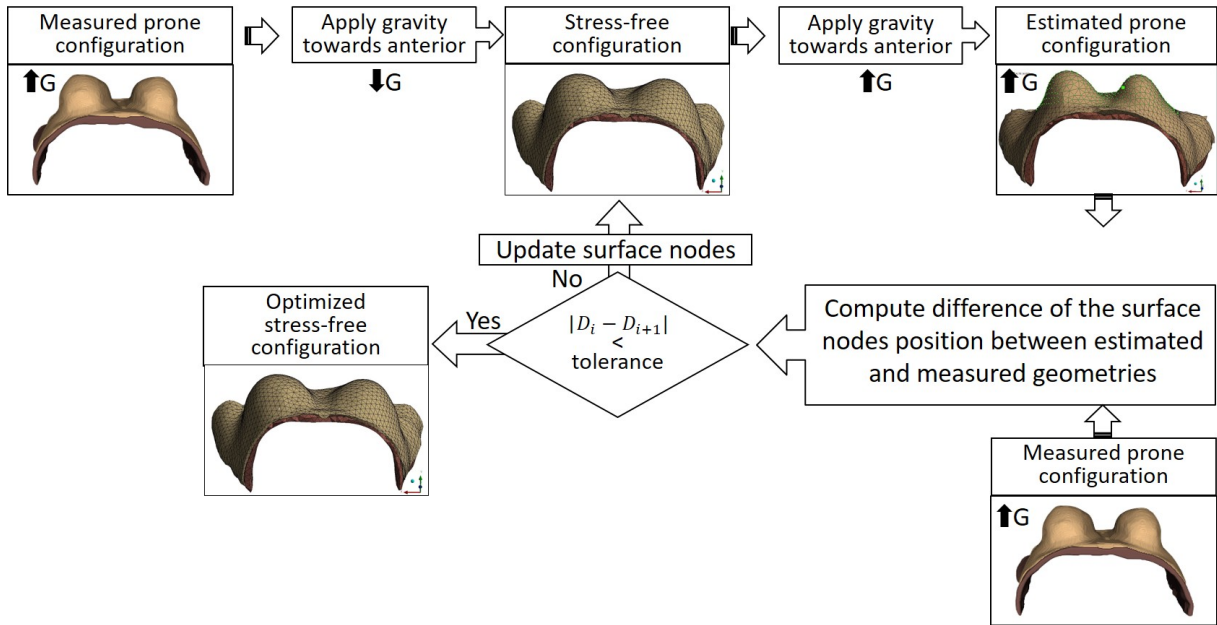


Figure 2.15: Prediction-correction algorithm

2.5.2 Constitutive models

¹²⁰⁰ Global breast mechanics is governed by breast tissue compositions and their individual mechanical properties. The breast soft tissues are known to be incompressible, nonlinear, anisotropic, and viscous materials. However, according to Wellman et al. (1999) the breast tissues viscosity can be neglected when the mechanical load is applied within short time scales.

¹²⁰⁵ Under large compression and body position changes, the breast volume can vary due to blood flows. Thus, soft tissues are frequently modeled as quasi-incompressible materials with a Poisson ratio ranging between $\nu = 0.45 - 0.5$. The influence of the Poisson ratio within linear constitutive models was studied for breast by Tanner et al. (2006); according to the authors, the best estimates are obtained with high Poisson ratio ($\nu = 0.495, 0.499$).
¹²¹⁰ The breast tissues are predominately composed of water; therefore, the density is considered to be equal to 981 kg/m^3 .

For the last decades several constitutive models were used to model the breast tissues response to an external force: exponential elastic (Azar et al., 2002), Neo-Hookean hyperelastic (Carter, 2009b; Rajagopal et al., 2010b; Sturgeon et al., 2016; Eiben et al., 2016a; Han et al., 2014; Garcia et al., 2017), Money-Rivlin (Samani et al., 2007; Tanner et al., 2006; Carter et al., 2012; Martínez-Martínez et al., 2017). Eder et al. (2014) compared the most popular models in a multi-loading gravity simulation; according to the authors, the Neo-Hookean model proposed by Rajagopal et al. (2008) gives the best estimates.

Glandular and adipose tissues biomechanical properties

1220 Multiple studies have shown that breast composition, and so its mechanical behavior undergo substantial changes during woman lifetime (section 1.2.4). The first studies on mechanical proprieties estimation of breast tissues were done in diagnosis purposes. When the breast is developing benign or malign disorders, its mechanical properties differ from the ones of the normal breast tissues. In a study of 142 samples, bellowing to 4 type of
1225 tissues, Krouskop et al. (1998) found that depending on the pre-compression level, Young moduli of invasive carcinoma is from 5 to 25 times larger than the one of normal adipose tissue (from 5% to 20% strain levels).

Later, several research groups (Table 2.2) have studied the elastic moduli of adipose and glandular tissues. The breast tissues elastic parameters range between 0.1 kPa and
1230 271.8 kPa. Such huge variation may be explained by the differences in the experimental set-up used to estimate stiffness, but also by the participant's physical condition, age or period of the menstrual cycle. For example, Han et al. (2012), though using the same FE method, found significantly inter-individual variability, with the shear moduli ranging between 0.22 – 43.64kPa. Lorenzen et al. (2003) showed that during the menstrual cycle,
1235 due to the hormonal changes, the elastic properties of the glandular tissues can change by about 30%.

An important difference in estimated values of breast elastic moduli is observed between the linear elastic and hyperelastic models. If only in-vivo studies with Neo-Hookean material models are considered, the range of the adipose and glandular shear moduli is significantly lower than 50kPa.
1240

Carter (2009b) compared a one parameter Neo-Hookean potential function with a five parameters Money-Rivlin potential function for various material properties. The multi-loading gravity simulations were thus performed on 3 subjects. According to the authors, even for parameters 10 times softer than the literature (Samani et al., 2001), the Money-Rivlin model underestimates the tissues deformation by at least 75% when the subject is re-positioned from the supine to the prone positions. The best estimates were given by the Neo-Hookean model with the initial shear moduli equal to 0.2kPa.
1245

Previously listed researches clearly showed the variability of elastic moduli of the same tissue between and within individuals. Eder et al. (2014) made a larger analysis including
1250 all material models proposed in the literature. According to authors, many of them are too stiff permitting not enough deformation within the gravity loading. This study has shown that the most reliable elastic moduli values are the ones given by Rajagopal et al. (2008) (Table 2.2).

Muscle biomechanical properties.

1255 Muscle is a kinematically, geometrically, and materially complex tissue. Muscle mechanical behavior depends on its contractile active and passive elastic properties (Nordez and Hug, 2010). In biomechanics the muscle is modeled using complex models as Hill-type models (Zajac, 1989), Feldmans lambda model (Feldman, 1986) which are considering the variation

Ex-vivo estimation				
Author	Method	Material model	material properties	
			Adipose kPa	Glandular kPa
Krouskop et al. (1998)	Indentation-5%	Linear elastic	$\lambda = 19 \pm 7 \text{ kPa}$	$\lambda = 33 \pm 11 \text{ kPa}$
Krouskop et al. (1998)	Indentation-20%	Linear elastic	$\lambda = 20 \pm 6 \text{ kPa}$	$\lambda = 57 \pm 19 \text{ kPa}$
Wellman et al. (1999)	Indentation - 5%	Linear elastic	$\lambda = 6.6 \text{ kPa}$	$\lambda = 33 \text{ kPa}$
Wellman et al. (1999)	Indentation - 15%	Linear elastic	$\lambda = 17.4 \text{ kPa}$	$\lambda = 271.8 \text{ kPa}$
Azar et al. (2002)	Indentation	Exp. elastic	$b = 4.46 \text{ kPa}; m = 7.4$	$b = 15.1 \text{ kPa}; m = 10$
Samani and Plewes (2004)	Indentation	Linear elastic	$\lambda = 3.25 \pm 0.91 \text{ kPa}$	$\lambda = 3.24 \pm 0.61 \text{ kPa}$
In-vivo estimation				
Van Houten et al. (2003)	MRE	Linear elastic	$\lambda = 17 - 26 \text{ kPa}$	$\lambda = 26 - 30 \text{ kPa}$
Sinkus et al. (2005)	MRE	Visco-elastic	$\mu = 2.9 \pm 0.3 \text{ kPa}$	
Rajagopal et al. (2008)	MRI-FEM	Neo-Hookean	$\mu = 0.16 \text{ kPa}$	$\mu = 0.26 \text{ kPa}$
Carter (2009a)	MRI-FEM	Neo-Hookean	$\mu = 0.25 \text{ kPa}$	$\mu = 0.4 \text{ kPa}$
Han et al. (2012)	MRI-FEM	Neo-Hookean	$\lambda = 1 \text{ kPa}$	$\lambda = 0.22 - 43.64 \text{ kPa}$
Gamage et al. (2012)	MRI-FEM	Neo-Hookean	$\mu = 0.1 \text{ kPa}$	
Griesenauer et al. (2017)	MRI-FEM	Hooke's law	$\lambda = 0.25 \text{ kPa}$	$\lambda = 2 \text{ kPa}$

Table 2.2: Material properties for adipose and glandular tissues.

of muscle elasticity in function of muscle state. In breast biomechanical models the muscle is combined with the thoracic cage and is frequently considered as a rigid breast support. In most of models, the pectoral muscle is modeled by imposing zero-displacement conditions on nodes closer to the chest wall (Samani et al., 2001; Chung et al., 2008; Rajagopal et al., 2010a) or by allowing them to slide along the chest wall line (Han et al., 2014; Georgii et al., 2016).

The muscle is nonlinear, anisotropic, incompressible material. The bibliographic data

on static mechanical properties of the muscle-tendon unit assessed by supersonic shear wave imaging elastography state a Young's modulus in range of $20kPa$ to $300kPa$ depending on the muscle location and subject's physical condition (Lima et al., 2018). The muscle shear moduli on the upper trapezius was studied by Leong et al. (2013), according to authors the muscle shear elasticity at rest was $17.11 \pm 5.82kPa$, and this increased to $26.56 \pm 12.32kPa$ during active arm holding at 30° abduction.

Skin biomechanical properties

Several studies have shown the importance of skin in biomechanical breast modeling. According to Carter (2009b), a model which includes the skin estimates better the tissues deformation under gravity loading.

Sutradhar and Miller (2013) published a complete study of breast skin estimating its elasticity for 16 different breast regions. The study was done on 23 female volunteers aging from 29 to 75 years. The authors found that the skin elastic moduli range between $15 - 480kPa$ with an average of $334 \pm 88kPa$. The elastic moduli in the lateral region (mean $370kPa$) has the highest value followed by the superior region (mean $355kPa$); the inferior region (mean $331kPa$) follows next, with the medial region having the lowest value (mean $316kPa$). However, no significant variation of elastic moduli in radial direction was found.

Other researches on skin elasticity are available, but they are not specific to the breast skin. Hendriks et al. (2006) estimated in-vivo skin properties by suction testing. The skin was considered as a homogeneous, isotropic, incompressible, hyperelastic material. The study was performed on 14 subjects and the obtained average of elastic moduli for skin was $58.4kPa$.

The estimation of the breast skin elasticity by the means of finite elements using Neo-Hookean potential function has resulted in softer materials model. Carter (2009a) found an initial shear modulus equal to $16kPa$, whereas Han et al. (2014) found that for the five studied subjects the skin shear moduli ranged between $2.47kPa$ and $5.78kPa$.

Fascias and ligaments biomechanical properties

The surrounding breast fascias and the supervisory ligament form the breast support matrix. These structures are well described for surgical purposes (thickness, location etc), however little is known about their mechanical properties. The first biomechanical breast model taking into account the effect of Cooper's ligaments was proposed by Azar et al. (2002) and took up later by Pathmanathan et al. (2008) and Han et al. (2012). The authors designed a new material model for fatty tissues including the anisotropic behavior of breast ligaments. Later, Georgii et al. (2016) come up with a spring-mass generic model for the breast support matrix. According to the authors, including the ligaments into the finite elements breast model have increased the robustness of the prone-supine simulation with respect to the input parameters.

To our knowledge, there are no experimental data describing the mechanical properties

1305 of breast superficial fascia. An approximation of the elastic moduli of Cooper's ligaments is given by Gefen and Dilmoney (2007) by extrapolating from known ligamentous structure in the human body. The authors estimated the elastic moduli of suspensory ligaments to relay between $80 - 400 \text{ MPa}$

1310 Fibrous tissues get their elasticity from elastin elastic fibers and their structural support from collagen fibers. As reported by Riggio et al. (2000), the superficial fascia is made up of both collagen and elastin fibers. In contrast, the Cooper's ligaments appeared to be composed almost of collagen fibers. The mechanical properties of a single collagen fiber from a rat tail were studied by Wenger et al. (2007); according to the authors the corresponding elastic moduli range between 5 GPa and 11 GPa . Other studies on biomechanical 1315 characterization of human body superficial fascia are available in the literature. The most frequently studied structures are the plantar fascia and foot ligaments, with a Young's moduli ranging between $0.1e^{-3} \text{ MPa}$ (Gefen, 2003) and 700 MPa (Cheung et al., 2004).

2.5.3 Boundary conditions

1320 Dirichlet conditions are usually used to constrain the sternum/axilla ends and the posterior surface of the breast or the thoracic cage if the muscular tissues are considered (Griesenauer et al., 2017; Rajagopal et al., 2008; Pathmanathan et al., 2008; Gamage et al., 2012; Griesenauer et al., 2017). As reported by Carter (2009b) the zero-displacement boundary 1325 conditions in a multi-gravity loading framework result in an over-constrained model; in that case sliding conditions on the mesh nodes corresponding to the chest wall have to be considered.

1330 Later, several teams using biomechanical breast models for multy modality image registration or surgical planing showed that including the sliding boundary conditions (Georgii et al., 2016; Han et al., 2014) improves the registration accuracy. However the most studies in which the biomechanical model is designed for breast compression, the tissues sliding over the chest wall is neglected and fixed boundary conditions are usually assumed (Sturgeon et al., 2016; Martínez-Martínez et al., 2017).

2.5.4 Conclusion

1335 During the last decades, several breast biomechanical models were proposed. However, only a small part of them (Carter, 2009b; Gamage et al., 2012; Han et al., 2014) were evaluated with respect to real tissues deformations. As we intend to build-up a subject specific 1340 breast biomechanical model capable of estimating multi-loading gravity deformations, we will only consider as relevant the biomechanical models that were evaluated and compared with real data. In this chapter, three biggest challenges were identified: the estimation of the breast reference geometry, the estimation of patient specific material properties and the definition of the boundary condition and namely the breast-muscle interface. Today's outstanding breast biomechanical models are represented by the next three models: Eiben et al. (2016c), Han et al. (2014), Gamage et al. (2012).

Gamage et al. (2012) proposed a finite elements model capable to estimate the supine breast configuration from the prone one. The breast stress-free configuration was estimated using a prediction-correction iterative algorithm optimization process, in this purpose the skin surfaces on prone configuration was used as ground-truth. Contrariwise, the material constitutive parameters were identified using the skin surface on supine breast configuration by applying a non-linear optimization algorithm. Breast tissues sliding over the chest wall was considered partially by modeling the pectoral muscle as a soft structure and including it into the optimization process. The models were evaluated for the supine breast configuration by computing the root-mean-squared error (RMSE) from the point to surface distance between the estimated and measured data. Conform to the authors, the breast supine geometry was estimated within an RMSE of 5mm (maximal distance of 9.3 mm).

In the same time, Han et al. (2014) developed a breast biomechanical model for image registration. The estimates of supine breast configuration were computed for five subjects, and the accuracy was assessed by computing the Euclidian distance between anatomical landmarks. The mean Euclidian distance range between 11.5 mm and 39.2 mm (maximal Euclidian distance ranged between 20.3mm and 61.7mm). The authors modelled the elongation of the pectoral muscle using a contact sliding model. Only the material constitutive parameters were adapted to the patients breast mechanics, the stress-free breast geometry being estimated by inverse gravity.

Finally, Eiben et al. (2016c) proposed a new model to estimate the up-standing breast configuration from the prone one. The model was evaluated on 3 subject. The patient specific stress-free geometry was computed using an inverse finite elements u-p formulation. The material parameters were optimized such that the best fit in supine configuration is obtained. The estimates quality was measured in terms of the mean Eulerian Distance between manually selected internal landmarks. Thus, the supine breast configuration was estimated within a mean distance ranging between 12.2mm and 19.8mm. The model evaluation for the up-standing configuration was not presented.

A new biomechanical breast model is proposed in the next chapter considering the patient specific breast geometry and elastic properties as proposed by the previous models. In addition, the breast tissues sliding over the chest wall is modeled by including new anatomical structures as superficial fascia and suspensory ligaments. We believe that global breast mechanics are driven by these stiff structures. Finally, the model will be evaluated by confrontation with real data collected from MR images.

Authors	Application	FE mesh	Material models	Boundary conditions	Stress-free config.
Azar et al. (2002)	Computer assisted breast surgery	8-Node hexahedrons (trilinear isotropic elements)	Skin-elastic adipose,glandular-hyperelastic polynomial	Sliding between breast - thorax and breast-paddle	Prone breast geometry
Rajagopal et al. (2007)	Breast compression	8-Node hexahedrons (tricubic Hermite elements)	Homogeneous , Neo-Hookean model	Zero-displacement BC	Buoyant breast in water
Pathmanathan et al. (2008)	Image registration	8-Node hexahedrons (trilinear elements)	Homogeneous polynomial Skin exponential hyperelastic	Zero-displacement on muscle; Compression with imposed displacement	Inverse FE algorithm
Han et al. (2014)	Image registration	4-Node tetrahedrons	Muscle, glandular, fatty, skin - Neo-Hookean model	Sliding on pectoral muscle	Inverse gravity
Gamage et al. (2012)	Computer assisted breast surgery	8-Node hexahedrons (tricubic elements)	Homogeneous+ Neo-Hookean incompressible model	Zero-displacement BC on rib cage surface, Sternum, axilla ends, shoulder	PC iterative algorithm
Patete et al. (2013)	Computer assisted breast surgery	4-Node tetrahedrons (trilinear isotropic elements)	Adipose , glandular, skin	Zero-displacement BC on the chest wall	PC iterative algorithm
Kuhlmann et al. (2013)	image registration	4-Node tetrahedrons	Adipose, glandular-gel-like (Eulerian formulation); Skin - hyperelastic material (Lagrangian formulation)	Zero-displacement chest wall	PC iterative algorithm
Georgii et al. (2016)	Surgery simulation	8-Node hexahedrons, 2-node 3D spars	homogeneous elastic material, Cooper's ligaments-generic mass-spring model	sliding BC (breast on the pectoral muscle)	NA
Eiben et al. (2016c)	Surgery outcome prediction	4-Node tetrahedrons	Fatty , glandular-Hookean model; exponential hyperelastic	Zero-displacement BC	Inverse FE algorithm
(Garcia et al., 2017)	3D breast lesion localization	4-Node tetrahedrons	adipose, glandular - Neo-Hookean models	zero-displacement BC	Prone breast configuration

Table 2.3: Breast biomechanical models

A new biomechanical breast model

3.1 Introduction

1380 State of the art in breast finite elements modeling was described previously. Three model
were identified representing the cutting-edge technologies in the field. These models use
prone MRI to create the breast reference geometry and supine MRI to compute patient-
specific tissues mechanical properties. The models were evaluated using the measured
and the estimated position of the superficial fiducial landmarks or internal anatomical
1385 landmarks in supine configuration. However, the authors assumed different boundary
conditions and considered different tissues types. In addition, none of the previous works
have quantitatively evaluated the proposed model on an additional data set of the same
patient.

1390 This chapter present a new biomechanical model developed by combining the best
practices and concepts proved by previous works. To be as realistic as possible, our model
considered breast heterogeneity, anisotropy, sliding boundary conditions, initial pre-stresses
and personalized hyper-elastic properties of breast tissue. In addition, new types of soft tis-
sue were included representing the breast support matrix composed of suspensory ligaments
and fascias. Moreover, our model was built using prone and supine breast configurations
1395 and was evaluated in supine tilted configuration (45) of the same volunteer.

1400 In the first part of this chapter the data acquisition protocol is described and details
on numerical methods and softwares used to extract the patient specific breast geometry
are given. Next, the different components of the finite elements mesh are presented and
the mesh quality is assessed using shape parameters. Then, the assumptions on boundary
condition and materials models are explained. Finally the model optimization process is
detailed and results on patient specific parameters and breast reference configuration are
presented.

3.2 Geometry extraction

Geometry extraction is the first step in FE analysis, and it consists of obtaining the 3D surface of the breast. We use the MR images to obtain the patient-specific breast volumes and the surrounding soft tissues distribution. Prior to surface extraction the MRI volume is segmented and mapped to a single reference system. The next section describe the imaging acquisition protocol and the numerical method used to generate the 3D patient specific breast geometry.

¹⁴¹⁰ **3.2.1 Data acquisition**

The images were acquired with a Siemens 3T scanner with T2 weighted image sequences. The in-plane image resolution was 0.5x0.5 mm, and the slice thickness was 0.6 mm. During this acquisition, the contact between the breasts and the contours of the MRI tube, or with the patient body (arms, thorax), was minimized.

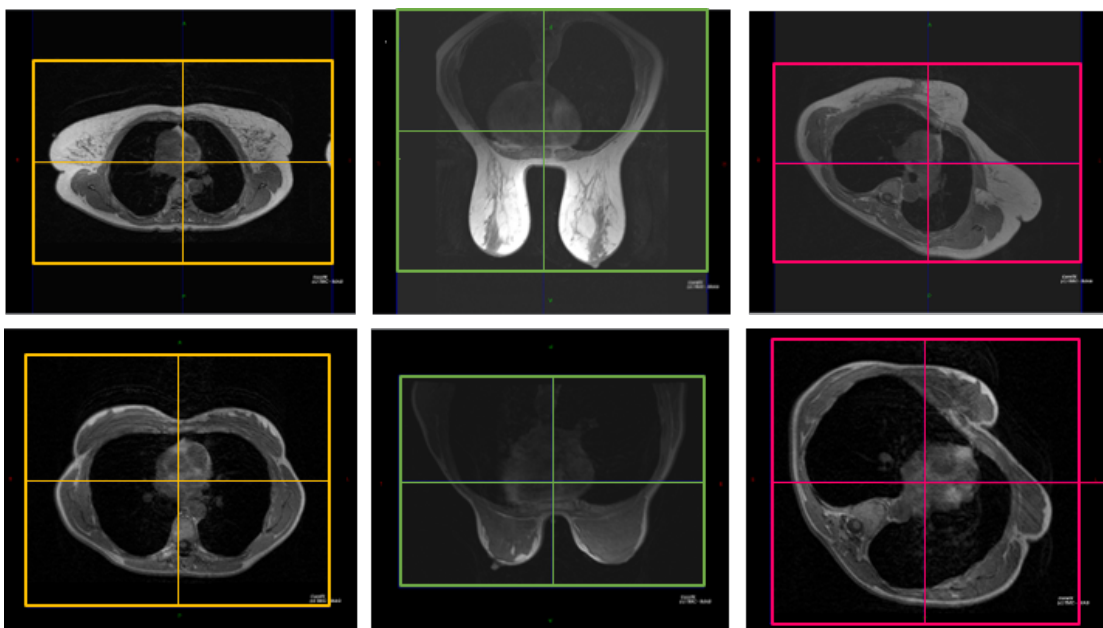


Figure 3.1: MRI images in three breast configuration: first line- subject 1; second line- subject 2

¹⁴¹⁵ The two volunteers taking part to this study agreed to participate in an experiment part of a pilot study approved by an ethical committee (MammoBio MAP-VS pilot study). The volunteers are 59 and 58 years old and have A-cup (subject 1) and F-cup (subject 2) breast size respectively.

¹⁴²⁰ Three different positioning configurations are considered: prone, supine and supine titled (45 deg). The positions were chosen to assess the largest possible deformations

with minimal contact areas between the volunteer and the relatively narrow MRI scanner tunnel.

3.2.2 Image segmentation

A semi-automated active contour method proposed by ITK-Snap software is used to segment the pectoral muscle, the breast and the internal organs from MR images.
1425

The segmentation process for one tissue type is performed progressively by small regions of interest (ROI, see Figure 3.2.a). For each ROI the segmentation of one tissue takes place in 3 steps (Figure 3.2):

1. Firstly, the random forest algorithm is used to compute the probability of a pixel to belong or not to the segmented tissue. The training data is manually selected by the user and include state and space characteristics as: voxel grey intensity, voxel's neighbors intensity (with variable radius of neighboring), (x; y; z) voxel position (Figure 3.2.c).
1430
2. Secondly, spherical seeds point with variable radius are placed on the new synthetic volume to mark the connected components belonging to the segmented tissue (Figure 3.2.d).
1435
3. Finally, the placed seed point will evolve in the 3D space with a speed and direction derived from the pixel intensity and sign in the synthetic volume (Figure 3.2.d).

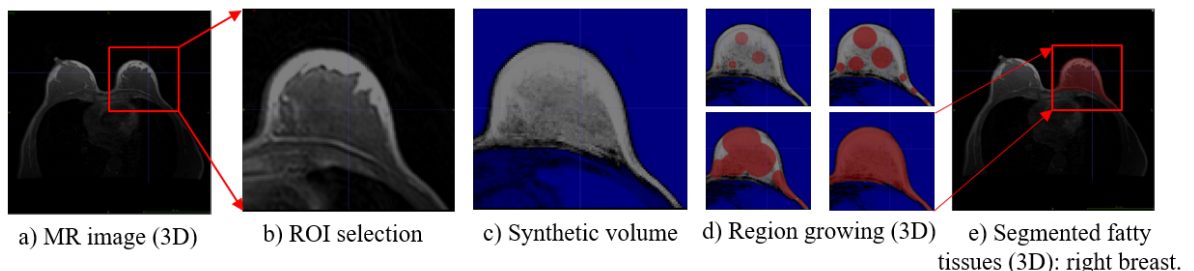


Figure 3.2: Breast tissues segmentation on the breast MRI of the second subject. Prone breast configuration. White-voxel belongs to breast tissue; blue - voxel don't belongs to fatty tissue
1440

After segmentation, an additional manual correction was performed to refine components boundaries. Simple erosion and dilatation operations were applied on breast and muscle segmented volumes in order to obtain smoother connected components. Then, to avoid tissues overlapping at muscle-breast juncture binary operations were used.
1445

The process was repeated for both volunteers and for each breast configuration: supine, prone and supine tilted.

1445 3.2.3 Image registration

During the imaging acquisition process, the subject is moved in and out the MRI scanner. Therefore, the breast not only undergoes an elastic transformation, but also a rigid one. Prior to image acquisition, four landmarks are fixed on the chest wall. The landmarks are placed on sternum and inframammary fold lines; regions known to be rich in fibrous ligaments limiting the soft tissues elastic deformation. To assess the body position changes between the two configurations a rigid transform is computed by minimizing the Euclidian distance of the four points defined by the four landmarks. The transformation is estimated using the iterative closest point (ICP) algorithm proposed by ITK library.

However, because of breast hyperelasticity the computed transformation is not accurate enough. Therefore, a second registration step is performed by aligning the bone structures of the anterior part of thoracic cage from prone and supine tilted positions to the supine one. The muscular tissues mask previously segmented are used in order to remove body soft tissues. The image registration is implemented using the descendant gradient based algorithm minimizing the images cross correlation (ITK library).

1460 Figure 3.3 shows overlapping prone-supine and supine tilted-supine breast images in the transversal plane after registration. The anterior part of the chest line is wall aligned, however there are some differences because of elastic thoracic cage deformation due to hand positions or body-mass force reparation.

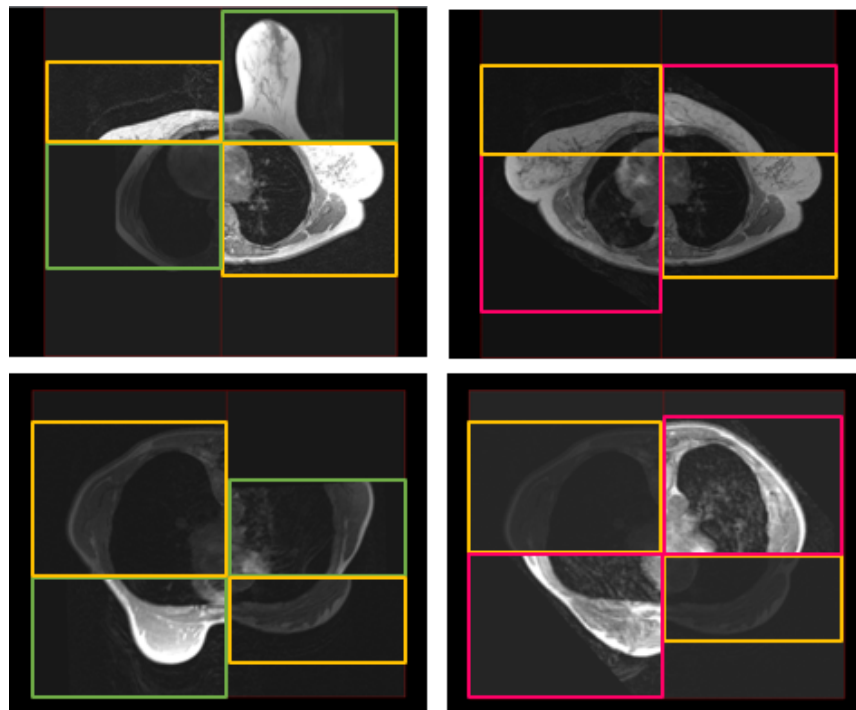


Figure 3.3: Registered MRI images: first line- subject 1; second line- subject 2; first column - prone configuration versus supine; second column - supine tilted versus supine

In a multi-gravity loading finite elements simulation, the gravity force is applied to the whole model as a body force. The gravity force orientation can be broken down into three components of the Cartesian coordinate system labeled X, Y, and Z directions. The supine configuration was chosen as a reference state, therefore the gravity loading direction was set to be oriented on the inverse direction of the Z axis (postero-anterior direction): $\gamma_s = (0, -1, 0)$. The gravity loading direction for the two other positions are given by the rigid transformation computed by images registration: $\gamma_p = (0.037, 0.985, -0.165)$ direction vector for gravity in prone position and $\gamma_{st} = (-0.744, -0.667, 0.023)$ direction vector for supine tilted position.

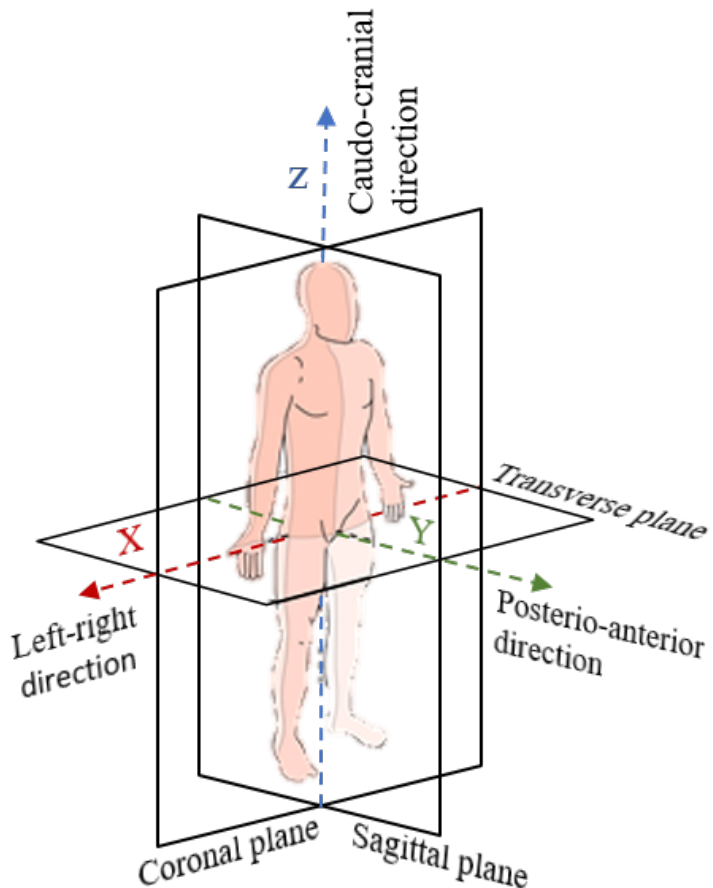


Figure 3.4: Anatomical planes and nominal Cartesian axis directions.

3.2.4 Patient-specific 3D geometry

The breast patient-specific geometry was created based on the MR images of the second subject. Following image segmentation (Figure 3.5.b), the outer shape of labeled regions

are subsequently discretized by 2D triangular elements. We used the semi-automatic Skin Surface module proposed by SpaceClaim Direct Modeler to convert the mesh surfaces to non-uniform rational basis spline (NURBS) surfaces. The NURBS are averaging curves between points, therefore they are smoother and easier to use in mechanical applications.

¹⁴⁸⁰ The resulting two surface represent the 3D geometries of the breast and the thoracic cage with muscle (Figure 3.5.c).

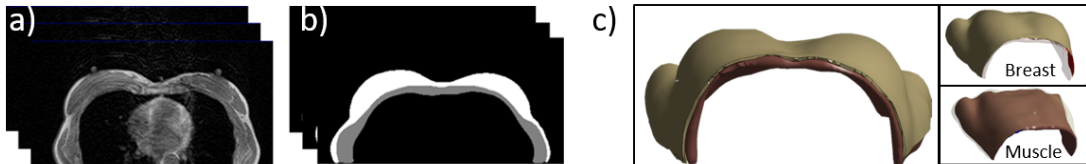


Figure 3.5: 3D geometries generation. a) MR images; b) segmented image; c) corresponding 3D geometries

3.3 Finite Elements Mesh

After computing the NURBS surfaces, the internal spatial information needs to be encoded using a volumetric mesh. The optimal elements type or mesh density in the simulation of FE models is still an open problem and topic of debate. The use of hexahedral elements results in a more accurate solution, especially when expecting high strain/stress gradients. However, in literature, because of the large computational time, they are used mostly with a reduced number of elements (Ruiter et al., 2006; Gamage et al., 2012). Tetrahedral elements are widely used due to their geometrical flexibility and because they provide a good trade-off between the computation time and displacement accuracy (Han et al., 2014; Palomar et al., 2008; Griesenauer et al., 2017).

¹⁴⁸⁵ In our case, an iterative optimization process is being considered, thus to reduce the computation time only linear tetrahedral elements are used. The first order elements are known to bear volumetric locking problems when used to model large strain for quasi-incompressible materials, (Fung et al., 2017). Then volumetric locking occurs, the displacements calculated by the finite element method are orders of magnitude smaller than they should be. It have been shown that a linear element with a mixed U-P formulation can avoid these problems (Rohan et al., 2014). In our work, the geometries are meshed using the solid element solid285 (ANSYS Mechanical) which provide a mixed U-P formulation option.

¹⁴⁹⁵ On the other hand, the mesh density have also an impact on model accuracy, a finer mesh results in a more accurate and stable solution, but also increase the computational time. So far, no experimental studies have determined the optimal resolution of the volumetric mesh for simulation of breast tissues deformation. To determinate the appropriate mesh size, a mesh convergence study was performed. The details can be found in annex According to these results the optimal elements sizes range between 7 and 10mm. The

chosen mesh consists in 18453 elements with 9625 elements assigned to the pectoral muscle and the toracic cage and 8828 elements assigned to breast tissues (Figure 3.7).

The mesh quality is measured using three criteria: element skewness, aspect ratio and maximal corner angle. The Figure 3.6 shows the ranges of values for different elements shape parameters. The element's aspect ratio and maximal corner angle range between the nominal limits defining a good mesh quality (Section 2.3). There is a small number of elements with a skewness larger than the maximal theoretical quality limit (0.75) , however there are no degenerated elements (skewness = 1).

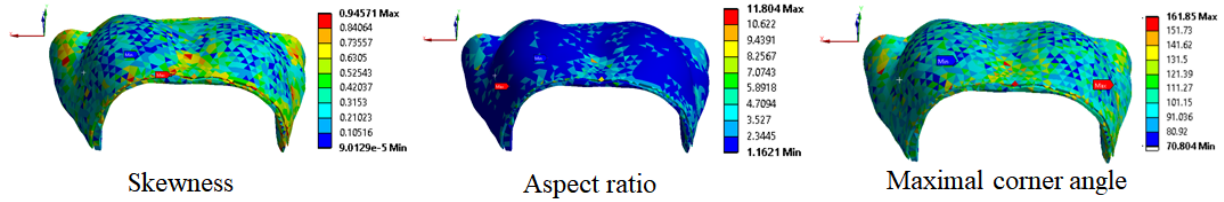


Figure 3.6: Finite elements mesh quality.

The breast skin layer is added a posteriori as a 2mm thick single layer of shell elements (1980 elements). Shell elements and the underlying solid elements are sharing the same nodes (Figure 3.7).

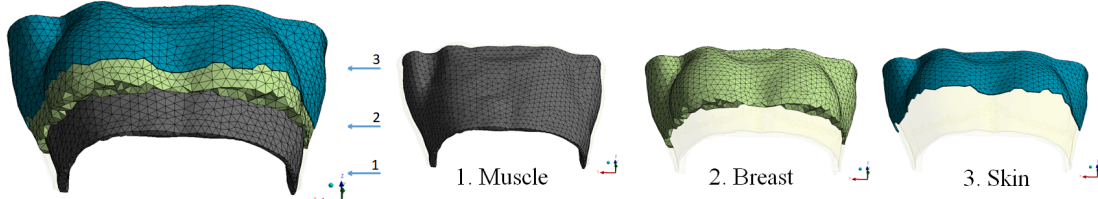


Figure 3.7: Finite elements mesh components. The tissues components are cropped for visualization purposes.

3.4 Breast reference configuration

To estimate the reference configuration of the breast, an adapted prediction-correction iterative approach was implemented. Prone and supine image data sets are used to compute the stress-free geometry. The overall iterative process is presented in Figure 3.8. The first estimate of stress-free breast configuration is obtained by inverse gravity on supine geometry. Then, at each iteration, the estimated stress-free configuration is used to simulate breast deformation due to gravity in a prone position. The differences between result of this simulation and the real shape of the breast in prone position is quantified by computing the Euclidian distance D_i between the *active nodes* defined at the breast external surface. This distance is then used in the next iteration of our process to simulate an

imposed displacement (Dirichlet condition) to the active node i in the stress-free condition. To limit any mesh distortion, the displacement is only partially imposed using a multiplicative regularization factor ($\alpha < 1$). The process repeats as long as the new transformation improves the similarity between two geometries by more than 1mm on average. The similarity between the estimated and measured prone breast configuration is given by the mean Euclidean distance over the active nodes.

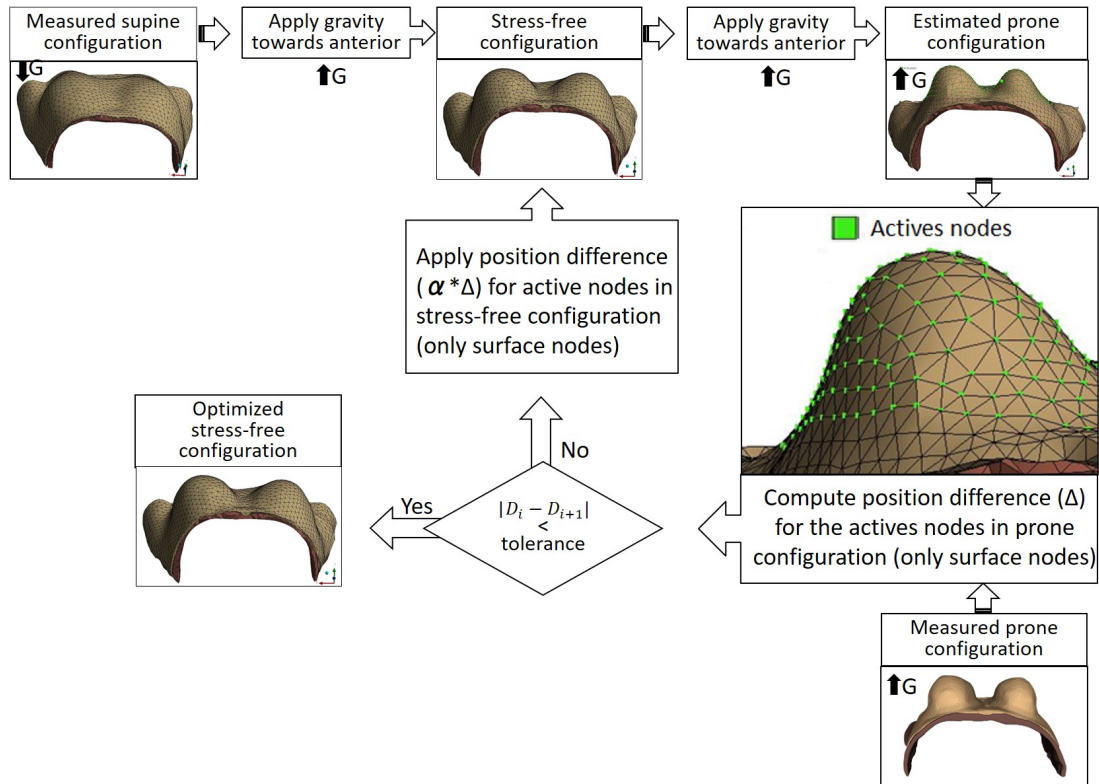


Figure 3.8: Fixed point type iterative algorithm for stress-free geometry approximation. D_i - mean node to node distance over the active nodes at iteration i , G - gravity force

To compute the position difference D_i of the node i between the estimated and measured breast configurations , the position of the active surface nodes on prone configuration have to be known. Thus, an additional mesh registration step is performed at each iteration. The active nodes are morphed into prone configuration using the elastic deformation method proposed by Bucki et al. (2010). The method estimates a C1-diffeomorphic, non-folding and one-to-one transformation to register a source point cloud onto a target data set D , which can either be a point cloud or a surface mesh. The input source points set is initially embedded in a deformable virtual hexahedral elastic grid. Then an iterative registration technique is performed by successive elementary grid deformations and at different grid refinement level.

3.5 Boundary conditions

1545 Breast deformation can be modeled by solving the motion equations using two different types of boundary conditions, regarding either displacement (Dirichlet conditions) or force (Neumann conditions).

1550 First, to provide a rigid support for the muscle mesh component, zero displacement conditions are imposed to its posterior face (figure 3.9). Next, the interface between the breast mesh and muscle mesh is models using contact mechanics. The muscle is stiffer than the adipose tissues, thus it's anterior face represents the target surface and the posterior breast face represents the contact surface.

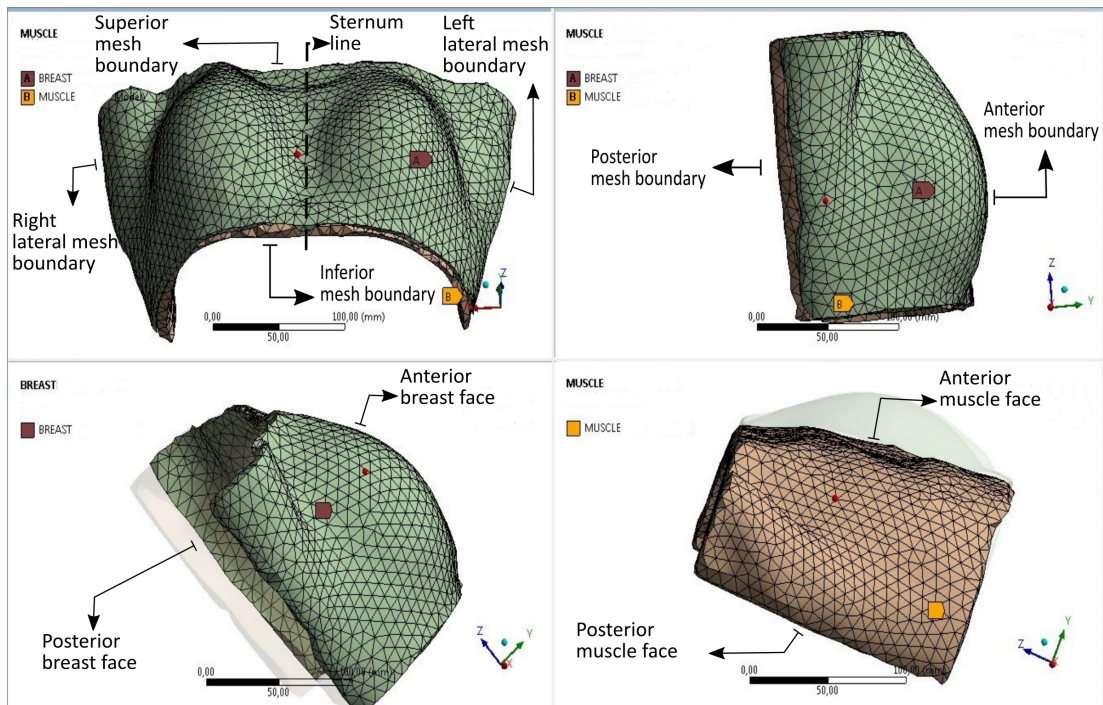


Figure 3.9: Finite elements mesh boundaries

1555 Previous works have proved that to model breast deformation from prone to supine configurations breast tissues sliding over the chest wall have to be considered (Carter et al., 2012; Han et al., 2014). Moreover, anatomical books (Mugea and Shiffman, 2014; Clemente, 2011), describe that the breast soft tissues are firmly attached to the deep fascia via suspensory ligaments but move freely over the pectoralis muscle. Therefore, the juncture surface is modeled as a no-separation contact with a frictional behavior proposed by ANSYS Contact Technologies (see sec.2.4.2). Penalty algorithm is used with a meticulous control
1560 of contact normal and opening stiffness parameters. Stiffness parameters don't have a physical meaning and have to be identified by *trial and error* methods. Because they are extremely sensitive to the underlying elements stiffness and to the local deformation direction, new values have to be identified for each new simulation case.

To study the impact of the frictional coefficient parameter on tissues sliding, several simulation have been performed at different values of μ_f . We found that, with the Coulombus friction law, even for a high values of μ_f the tissues sliding is overestimated. When simulating prone breast configuration from the supine one, the sliding overestimation results also in an unconvenger solution due to element distortion. At the contact surface, because of excessive sliding, the tissues accumulation in the region of the sternum line 1570 results in a sinuous surface (fig. 3.10) ; the finite elements undergo important distortion and the solution is compromised. Therefore different strategies based on anatomical breast structures were investigated to limit the amount of sliding and to overcome solution instabilities (Annex 2). However, a small amount of friction improve the solution convergence capabilities (refer ansys manual), thus the friction coefficient is kept to $\mu_f = 0.1$.

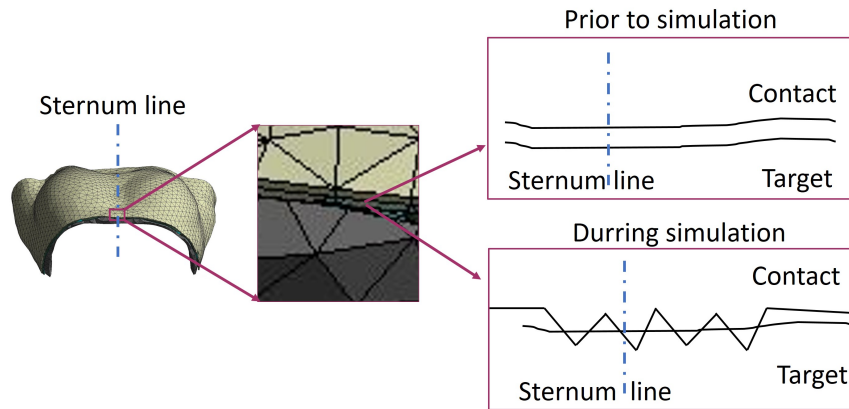


Figure 3.10: Tissues accumulation on the sternum line with excessive sliding

The selected strategies chosen to control the amount of tissues sliding relies on ligamentous breast structures described on sec. 1.2.3. From breast support matrix only the largest structures are modeled, i.e. fascias and suspensory ligaments. Superficial layer of superficial fascia is integrated in the skin layer, assuming a higher material stiffness. In addition, a new layer of 0.1mm thick shell elements is added at the juncture surface 1580 between muscle and breast tissue to model the deep layer of the superficial fascia. Shell elements and the underlying breast elements are sharing the same nodes. Since the deep fascia and muscle tissues are supposed to present similar elastic properties, the deep fascia is not explicitly modeled. Two ligamentous structures (inframammary ligament and deep medial ligament) are modeled using Ansys link type elements connecting breast posterior 1585 surface nodes to anterior muscle surface nodes (Figure 3.11).

Several additional Dirichlet conditions are set on the mesh boundaries: superior and inferior ends of the deep fascia layer are constrained in Z direction; superior and inferior ends of skin layer are constrained in Y direction. For left and right lateral breast boundaries (Figure 3.9), Dirichlet conditions are too strong and preclude breast tissue to slide laterally. Therefore, in these regions new ligamentous structures are included with a cable-like behavior (fig. 3.11).

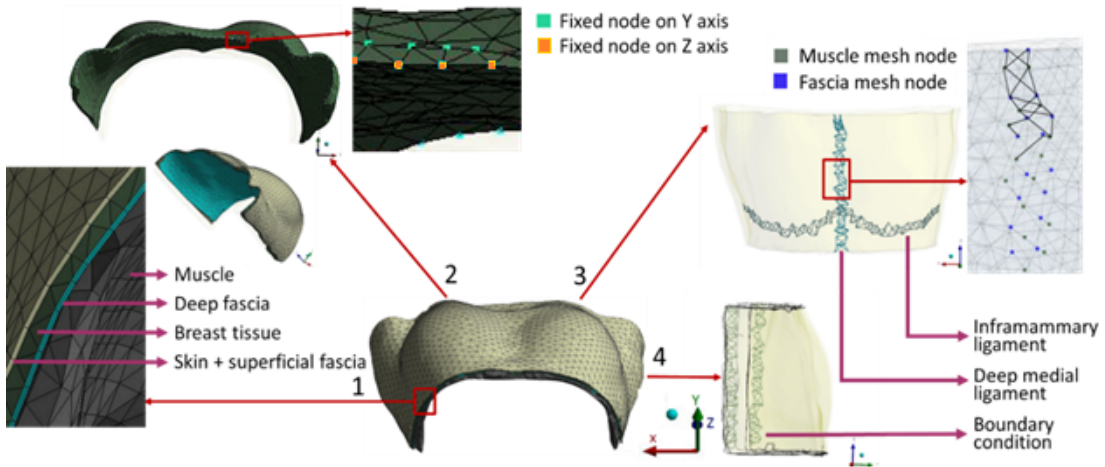


Figure 3.11: Components of the finite elements mesh.

The deep layer of superficial fascia is much stiffer than underlying adipose tissues. Due to imposed boundary conditions, the amount of sliding depends fascia's elasticity. The suspensory ligaments define regions were the breast sliding is minimal regardless of applied deformation. These additional stiff structure reduce the tissues sliding and improve the solution convergence capability.

3.6 Materials constitutive models

The final model consists of 6 types of tissues, wherein 4 tissues (glandular, fatty, muscle and skin) are well described and regularly used for biomechanical modeling and 2 of them (fascia and suspension ligaments) with limited use and poorly described in literature. A large range of constitutive parameters are available for each tissue, however because of an inconsistent interindividual variability, patient specific parameters have to be identified.

Here, all materials except the suspensory ligaments are modeled using the Neo-Hookean potential function. Breast ligaments are considered as linear materials. Subject specific mechanical tissue properties are computed using an optimization process based on a multi-gravity loading simulation procedure (Figure 3.12). First, for a given set of parameters ($\lambda_{breast}, \lambda_{muscle}, \lambda_{skin}, \lambda_{fascia}, \lambda_{ligam}, \nu$) the breast stress-free configuration is estimated by minimizing the difference between the simulated and measured breast geometry in prone configuration. Then, from the new estimated stress-free geometry, the supine breast configuration is derived. The estimated supine geometry is compared to the measured one using modified Hausdorff distance, thus representing the estimation error. To avoid taking in account the geometry dissimilarity due to arms position, the modified Hausdorff distance is computed only on breast skin surface. The process implies multiple simulation based on imposed nodes displacement, therefore the FE mesh can be significantly altered before reaching an optimal stress-free geometry. Mainly for that reason we chose to perform an

exhaustive manual rather than an automatic research of the optimal set of constitutive parameters.

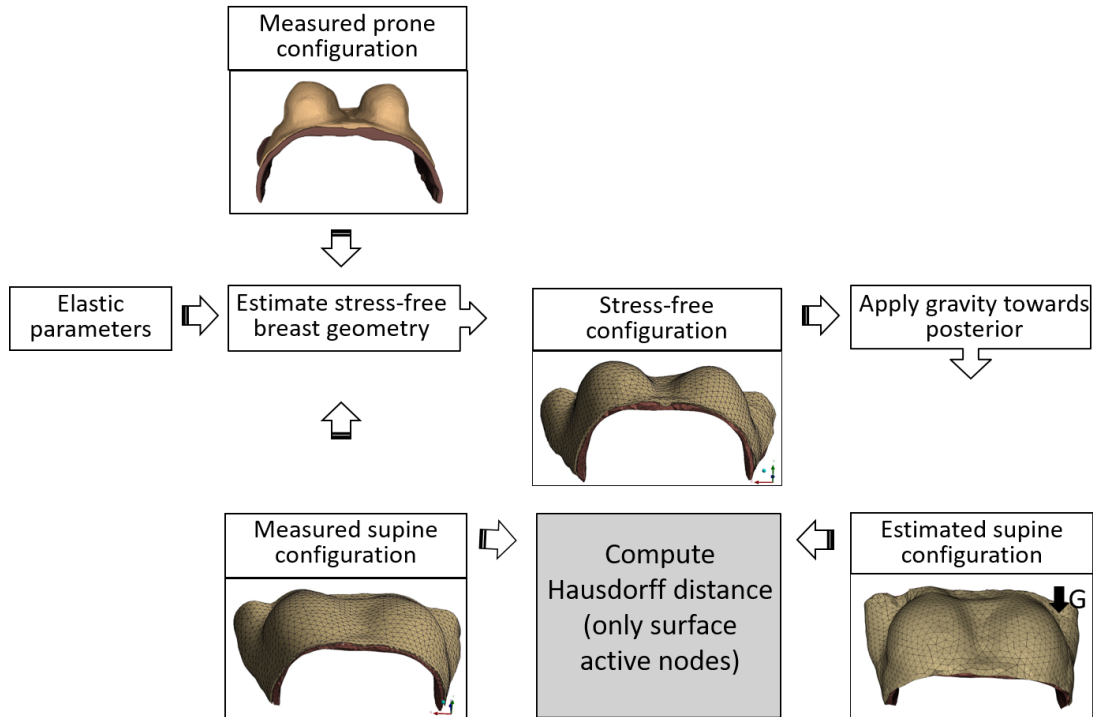


Figure 3.12: Process to estimate optimal material parameters

An optimization process including finite elements simulation with 6 parameters results is a complex and time consuming problem. The model simplification is then performed in two steps. First, the parameters which variation have non-significant effect on simulation results are identified and set to a optimal fixed value. Next for parameters which variation have a high impact a sensitivity study is performed to redefine the search intervals and interval's discretization step.

3.6.1 Model simplification

The breast tissues are mainly composed of water, an usual assumption is to consider them as nearly incompressible materials (Fung, 2013). However, previous works proposed a Poisson's ratio value ranging between $\nu = 0.3$ (Hopp et al., 2013) and $\nu = 0.5$ (Gamage et al., 2012). In a multi-loading gravity simulation, the breast volume is nearly constant, thus, the influence of Poisson's ratio on nodes displacements is studied only for values laying between $\nu = [0.45, 0.495]$ (fig. 3.13).

The simulations were performed by applying the gravity force in posterio-anterior direction on breast geometry from supine configuration. On the right hand side, the mean and the maximal displacement of the skin nodes is given for each values of ν . On the left hand side the maximal difference of nodal displacement between two consecutive simulations

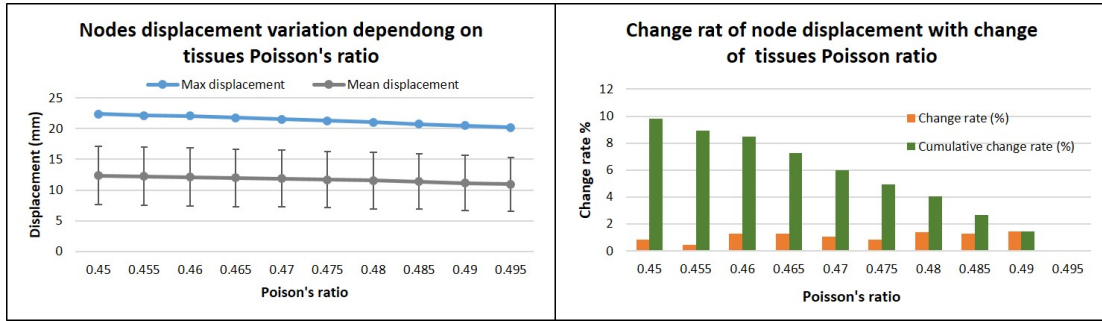


Figure 3.13: Process to estimate optimal material parameters

(change rate) and the maximal difference of node displacement between the actual and the less deformed geometry (cumulative change rate) are plotted. The change rate is computed within the assumption that the maximal displacement over the simulations set represents 100% change rate. Non significant variations are observed on the mean and maximal displacement of skin nodes, thus a constant values of $\nu = 0.49$ was chosen.

The pectoral muscle together with the thoracic cage are the breast tissues support, under gravity loading the muscle deformation is neglected. Therefore, its Young's modulus was not included on the parametric study and was chosen large enough so that only minimal deformations occur ($\lambda_{muscle} = 10kPa$).

The ligamentous breast structures are added with a cable-like behavior to reduce tissues sliding. Their young's modulus is also not included in the optimization process and is set sufficiently high ($\lambda_{ligam} = 500kPa$) to preclude their elastic deformation.

The adipose and glandular tissues are known to be extremely soft and to undergo large deformation under gravity loading. Calvo-Gallego et al. (2015) proposed a uniform polynomial material model for the mixture of adipose and glandular tissues. The authors also shown that the breast outer shape deformation does not depend on glandular distribution but is highly dependent on its volumetric ratio. Here, the glandular and fatty tissues are also modeled as a single homogeneous material with an equivalent Young's modulus λ_{breast} . The mechanical properties of the equivalent breast tissue is in direct relation with glandular and adipose volumes ratios. Because the left and right breasts may have a different granularity, two different parameters are considered ($\lambda_{breast}^l, \lambda_{breast}^r$).

Breast skin and superficial fascia are an essential part of the breast support matrix. The two layers are much stiffer than breast tissues and are the structures governing the amount of deformation. Their elastic behavior was included on the optimization process.

Based on existing publications, an interval of possible values are given in table 3.1 for each parameter included in the optimization process ($\lambda_{breast}^l, \lambda_{breast}^r, \lambda_{skin}, \lambda_{fascia}$). To characterize model sensitivity to parameters variations, a set of simulation were performed. The defined interval was discretized by steps of 10% and at each step the skin node displacement was computed. Results of the corresponding simulations are shown on fig.3.14. As previously, the first column represents the variation of mean and maximal displacement of skin nodes in function of the elastic parameter of each material; the second column

represent the change rate and the cumulative change rate of skin nodes displacement.

	Search intervals from bibliographic data			Search intervals after model simplification		
	Breast	Skin	Fascia	Breast	Skin	Fascia
Min (kPa)	0.3	7.4	100	0.3	2	50
Max (kPa)	6	58.4	5000	4	20	250

Table 3.1: Minimal and maximal value (in kPa) for Youngs modulus.

The figure shows that the model is very sensitive to the variation of Youngs modulus of breast tissue, skin and fascia (Figure 3.14). However, beyond some values, the materials become too stiff and do not change significantly under gravity loadings. Therefore, the search intervals for breast tissue and skin Youngs modulus are reduced such that a larger value impacts the cumulative change rate less than 20% (max displacement less than $\sim 5\text{mm}$). As the fascia stiffness governs the lateral displacement and shows a smaller variation over the search interval, a threshold of 10 % ($\sim 2.5\text{mm}$) is chosen. The obtained results are summarized in table 3.1

3.6.2 Estimation of optimal constitutive parameters

To perform the optimization process, the new intervals defined by sensitive analysis are discretized by steps of 0.1kPa , 1kPa and 40kPa . The discretization step are chosen such that the change rate between two consecutive simulations is less than 10%.

The previously described multi-loading gravity process was performed for each parameters set and the model error distribution is shown in fig 3.15. The contour lines are estimated by linear interpolation between two consecutive succeeded simulations. We found that the breast tissues Young's modulus is lower than the ones proposed in the bibliography, therefore more simulations were done outside the defined interval. However, for very low values, below 0.2 kPa, 2 kPa and 80 kPa for breast, skin and fascia's Young's moduli respectively, the tissues deformation is too large and the finite element mesh becomes degenerated at the first step of multi-loading simulation. For values above 1 kPa, 5 kPa and 160 kPa, tissues deformation is too small compared to the ones measured on the MR images and the simulations were excluded. All other missing values correspond to failed simulations due to a non-converging force, specifically in the region of the contact surface between the breast and the muscle.

For very soft fascia ($\lambda_{fascia} = 80\text{kPa}$), the lateral displacement of breast tissues is more important than the one measured on MR images. Conversely, for stiff fascia material ($\lambda_{fascia} = 160\text{kPa}$) the amount of sliding is too small; therefore, to match the breast geometry in supine configuration, very low values for Young modulus are required ($\lambda_{breast} < 0.2\text{kPa}$). For such low values, the breast tissues are highly deformed, thus the finite elements undergo distortions. Because of errors in elements formulation the simulations giving the minimal Hausdorff distance have not succeed.

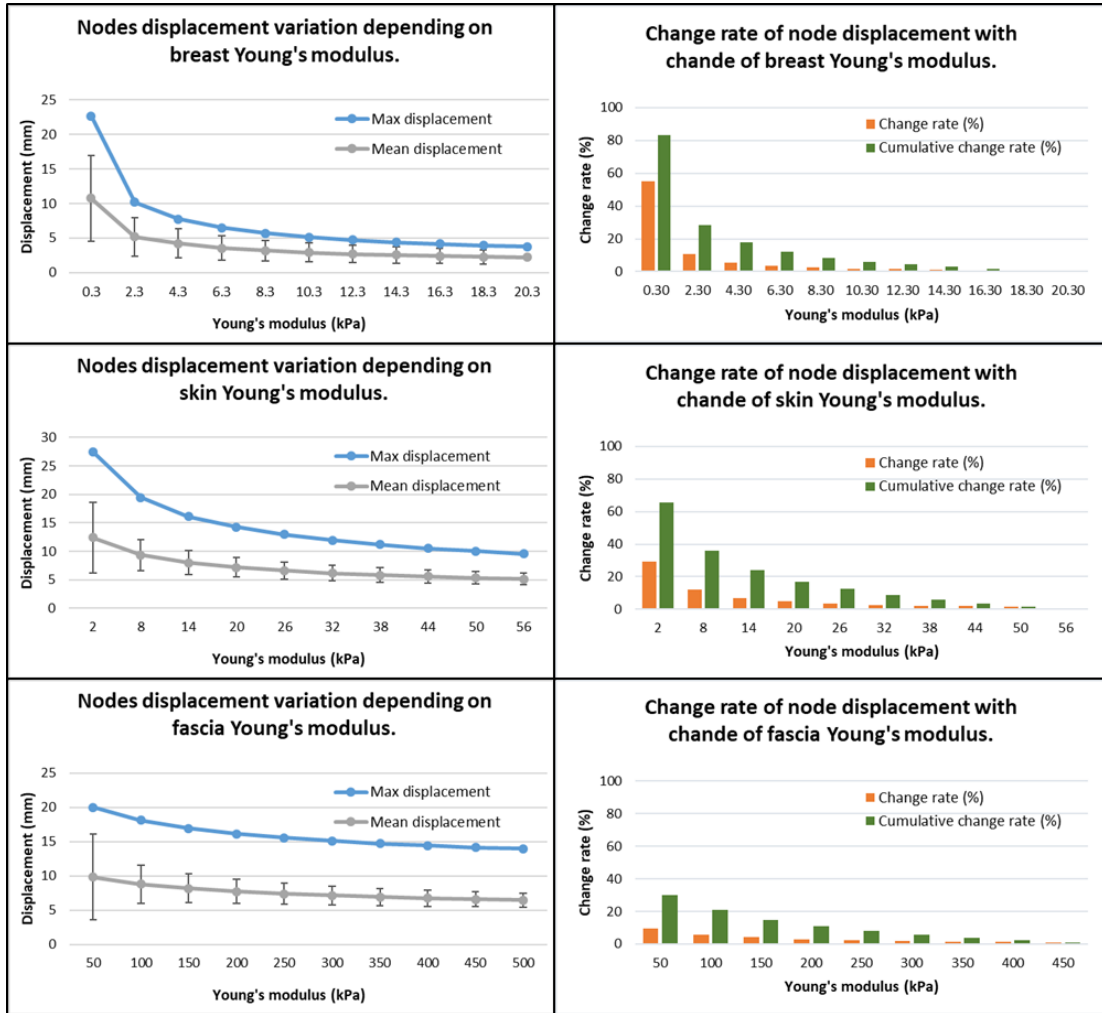


Figure 3.14: First column: relation between maximal and mean nodes displacement and the equivalent Young's modulus variation for different tissues. Second column: rate and cumulative change rate of node displacement in function of quivalent Young's modulus

The set of parameters giving the best match between simulated and measured supine breast configurations is ($\lambda_{breast}^r = 0.3 \text{ kPa}$, $\lambda_{breast}^l = 0.2 \text{ kPa}$, $\lambda_{skin} = 4 \text{ kPa}$, $\lambda_{fascia} = 120 \text{ kPa}$).
1700

3.6.3 Conclusion

This chapter propose a new biomechanical breast model. The model was build on patient-specific data extracted from MR images in different breast configurations. New structures as pectoral fascia and suspensory breast ligaments were considered and their impact on breast mechanics was analyzed in a multi-loading gravity simulations. A particular attention was granted to the estimation of subject-specific breast stress-free geometry and

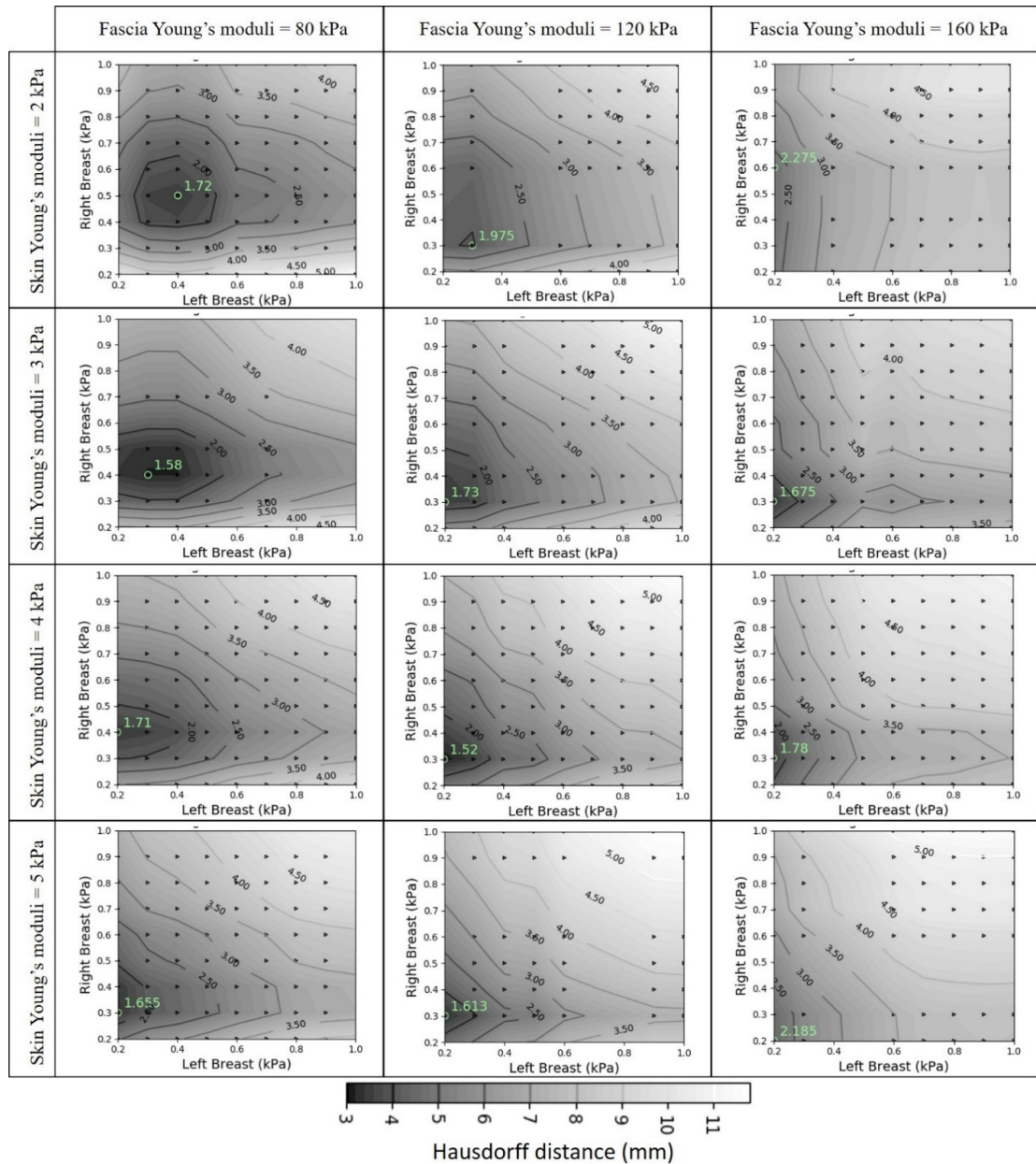


Figure 3.15: Hausdorff distance on the skin surface over the constitutive parameters space

tissues constitutive models.

The proposed breast model shows that introducing a sliding movement of the breast tissues over the pectoral muscle together with a ligamentous system and pectoral fascia, allows a better estimation of supine and prone configurations. The latter support structures provide a finer method for boundary conditions definition which also improve the convergence capability of the solution. It can be stated that the obtained Youngs modulus of breast soft tissues is relatively low (0.2-0.3kPa for breast tissues and 4kPa for skin),

which is a contradictory result compared to some studies on the field. However, only
1715 with such small values together with sliding boundary conditions that prone and supine
configurations were accurately estimated.

With the obtained optimal constitutive parameters set ($\lambda_{breast}^r = 0.3kPa, \lambda_{breast}^l = 0.2kPa, \lambda_{skin} = 4kPa, \lambda_{fascia} = 120kPa$) and the corresponding breast stress-free configuration simulations with the gravity force oriented in different directions could by simulated.
1720 The next chapter evaluate the model accuracy on three breast configurations: supine, prone and supine tilted.

Model validation

4.1 Introduction

- 1725 The previous chapter describe the numerical methods used to develop the breast model and to optimize the patient specific geometrical and mechanical properties. The constitutive parameters giving the best fit between the simulated and measured breast geometries were identified. Knowing the mechanical behavior, the corresponding stress-free geometry is computed and used hereafter as reference configuration for each finite elements simulations.
- 1730 Only the information from MRI volumes in supine and prone configurations were used for the development of the patient specific model.

1735 Previous biomechanical models have used the same MR images for the optimization and evaluation process. In such cases, the model accuracy is assessed for single a deformation case, the one used during the optimization process. Because of overfitting problems, the model fidelity to the global breast mechanics independently on the applied gravity direction is poorly described.

1740 The developed breast model is needed to model breast tissues deformation under compression, thus the model error have to be assessed in a more general context. In this chapter the model accuracy is evaluated on supine, prone and supine tilted configuration. The third configuration was not used during the optimization process which allow us to quantify the model accuracy in a more general context than the one used for model optimization.

4.2 Technical approach

The breast reference geometry together with previously defined materials models were used to compute breast deformation under gravity loading. Three loading cases were considered: supine, prone and supine tilted. The body force direction was defined conform to the corresponding vectors obtained by image registration (section 3.2.3).

To asses the model accuracy to the tissues real deformation, different measures of distance were used:

- Euclidian node to surface distance;
- Mean Euclidian node to surface distance and standard deviation;
- Maximal Euclidian node to surface distance;
- Modified Hausdorff distance;

The detailed description of each distance measure can be found in annex ...

Each distance was computed between simulated and measured skin surfaces. Because the arm position can change between two body position, the node to surface distance is computed only on the skin nodes bellowing to the breast surface. The results for the three body position are presented in the following section.

4.3 Results

Figure 4.1 shows node to surface distance magnitude, mean node to surface distance and modified Hausdorff distance between the simulated and measured breast geometries obtained with the optimal sets of parameters for the three previously defined body configurations.

The prone and supine body configurations was used to optimize breast stress-free configuration and material's constitutive parameters. The breast geometry is better estimated in supine configuration with an Hausdorff distance equal to 1.72 mm. This is probably due to a better representation of the boundary conditions in supine configuration, as this configuration was used to create the initial finite element mesh. The breast geometry in prone configuration is also well estimated with a modified Hausdorff distance equal to 2.17 mm. The maximal node to surface distance is obtained on the breast lateral parts. Assuming a non uniform skin thickness or elastic properties over the breast surface as described by Sutradhar and Miller (2013), should improve the obtained results.

One may see that the estimated supine tilted breast configuration describes inadequately the breast geometry given by the MR images (Hausdorff distance equal to 5.90 mm). Large difference between simulated and measured breast surfaces is caused by the excessive sliding of breast tissues over the chest wall. Numerical or structural modeling choices could explain such behavior.

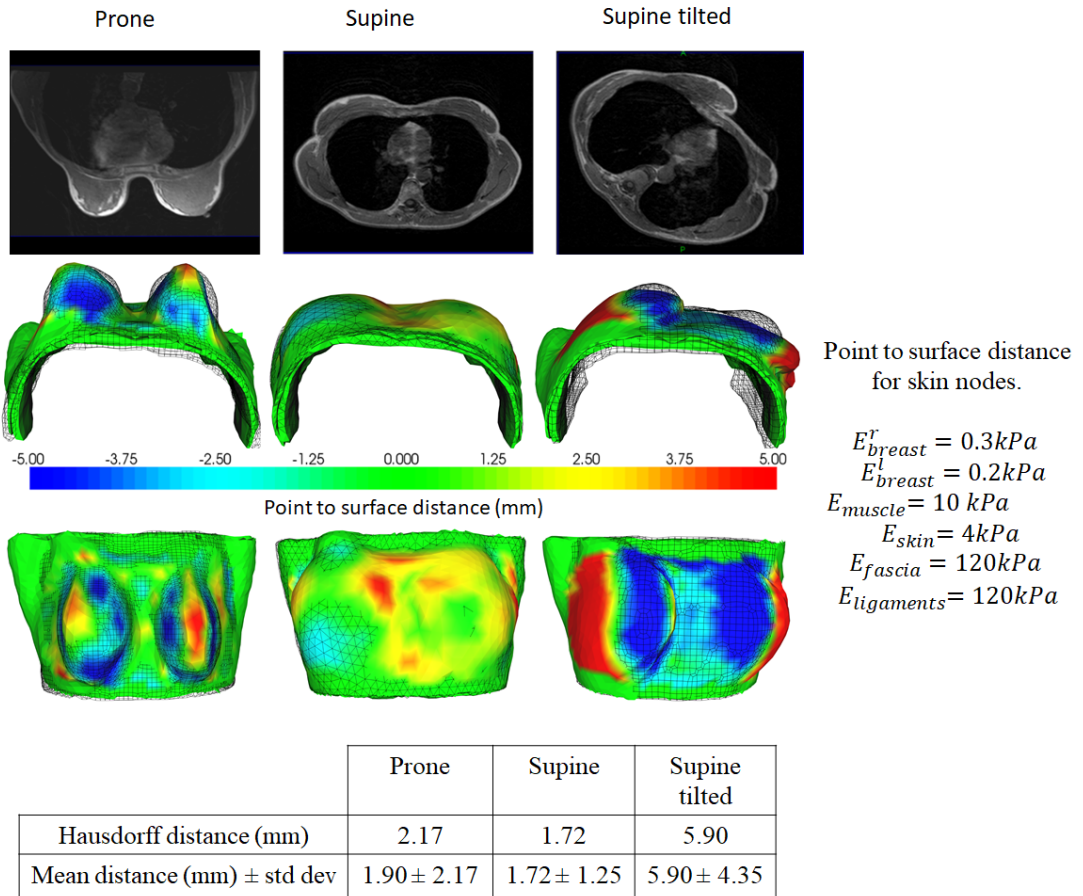


Figure 4.1: Three breast configurations: prone, supine and supine tilted. First line - MR images in 3 breast configurations. Second and third lines - point to node distance from simulated breast shape (surface mesh) to the measured one (black grid lines).

Firstly, the fascial and ligamentous tissues are usually characterized by a cable-like behavior. The strain-energy density function must behave asymptotically in order to limit the fascia stretch and thus to reduce non-linearly the breast sliding over the chest wall.

1780 Limitations of the neo-Hookean model to capture the mechanical response of some non-linear materials is well known (Kaliske and Rothert, 1997). For large strain rates, the Neo-Hookean material may undergo a relaxation and therefore becomes easier to deform.

1785 Our experimental results have shown that the maximal strain at the fascia level is significantly higher in supine tilted position (about 140%) than in supine or prone positions (about 50%). Therefore, an asymptotic behavior of fascia mechanical response must be considered. The Gent form of strain-energy function characterizes better such mechanical response (Gent, 1996) and should be considered as an alternative choice .

Secondly, the breast support matrix is composed of 4 suspensory ligaments, however only three of them were partially modeled: inframammary, deep medial and deep lateral ligaments. The 3D structures connecting the skin to some muscular areas were neglected,

and namely the cranial ligament. The particularity of the cranial ligament consist in it's position, almost it's entire structure underlay the skin and the only attachments to the thorax are situated at the clavicle and seventh rib level (inframammary ligament). Including such structures at the skin surface may result in local high strain gradient rates
1795 causing solution instability and anesthetic surface deformations.

4.4 Discussions and conclusion

In the current part of the manuscript, a new finite elements breast model was proposed and evaluated with real tissues deformations measured on MR images. To this end, MR images of two patients were acquired in three different configurations: supine, prone and supine tilted.
1800 The supine and prone MRI volumes were used to adapt the biomechanical model to the patient individual breast geometry and it's respective tissues mechanical properties. The optimal mechanical properties were found by exhaustive search over a predefined parameters domain. For each combination of tissues elastic properties, the breast reference configuration was computed using an adapted prediction-correction iterative scheme. The
1805 parameters set giving the best fit between estimated and measured breast configurations were selected. Using these optimal estimates the supine, prone and supine tilted breast configurations were computed and compared to the MRI volumes.

We found that, extremely soft materials low (0.2-0.3kPa for breast tissues and 4kPa for skin) have to be used in order to obtain the same tissues displacements rate as measured
1810 on MR images. Moreover, the breast tissues sliding have to be considered then computing such large deformations. However, because of tissues hyper-elasticity, the model boundary conditions have to be revisited in order to ensure the convergence capability of the solution. With such soft tissues, the finite elements mesh may become highly distorted, then to limit elements distortion a stiffer layer was added between the breast tissues and muscle
1815 representing the deep layer of the superficial fascia. The excessive sliding was prevented by using ligamentous structures fixing the soft tissues on the pectoral muscle.

Contrarily to the previous works, our model is evaluated in 3 breast configurations. Among the 3 geometries, two of them were used for the model optimization and evaluation, and the last one (supine tilted geometry) was used for the evaluation only. Good
1820 estimates were obtained in prone and supine configurations with a Hausdorff distance equal to 2.17mm and 1.72mm respectively. The estimate of the supine tilted breast geometry pointed out the limitations of the Neo-Hookean model to assess rich mechanical behavior of breast soft tissues for large strains. These limitations were not identified in the previous works.

The model optimization if a tough and time consuming process. It was extremely difficult to obtain the solutions convergence when combining the tissues large deformation with the sliding contact conditions. Because of the lake of time, the reference breast configuration and the optimal constitutive parameters were computed only for the first subject. The model optimization of the second subject is considered for feature work.
1825

Next, we assume that our model describe well the breast mechanical behavior and is

used to compute breast tissues deformation under compression. The internal tissues strain and the pressure distribution over the skin surface will be used to quantify the patient comfort during the mammography exam.

Part IV

Breast Compression: a comparative study

Background

5.1 Introduction

1840 Mammography is the sole screening method recognized by the European Commission for women aged 50-69 years. It's morphological method enable examination of the breast in its entirety and offer a high sensitivity for early-stage tumours. However, the mammographic exam is knew to be awkward and unpleasant for the patient, the main source of discomfort lying in it's operating principle. The perceived pain is related to the breast compression between the image receiver and the compression paddle.

1845 For such a standard and wide-used procedure good conditions and patient comfort should be ensured. Therefore a study on the relevance of breast compression methodology in mammography is of a potential interest. In the next chapters, a numerical simulation tool enabling the characterization of existing breast compression techniques in terms of 1850 patient comfort id developed. The latter would serve to build an optimal compression paddle, and therefore increase the adherence to breast cancer screening.

In this purpose, MR images of two subjects are used to create patient specific finite elements breast models. The mechanical behavior of soft tissues under compression is computed for both subjects and for both paddle designs. The perceived pain for a given 1855 paddle design is quantitatively characterized by contact pressure, internal stress and strain distributions. After compression, three sets of macrocalcifications are inserted into breast volumes. The latter are then subject to a Monte-Carlo based simulation (CatSim8) enabling to simulate the image acquisition of the compressed breast with a mammography system. Then, the diagnosis quality is assessed by measuring the signal-difference-to-noise- 1860 ratio (SDNR), signal-to-noise-ratio (SNR) and the average glandular dose (AGD).

5.2 Breast compression: overview

- Describe breast positioning and compression (Groot)
- Describe today's compression standards: force-thickness relation; thickness- AGD; force/thickness and pain relation; Pressure standardized mammography.

¹⁸⁶⁵ 5.2.1 Mammographic positioning

During mammography, a qualified radiologic technologist positions the breast of the patient between the stationary bucky (X-ray detector housing) and a movable paddle. A routine mammographic exam consists of two views: cranio-caudal (CC) and mediolateral oblique (MLO) projections. The views are complementary and provide a complete image of the entire breast. However, sometimes special view can be required to confirm or reject suspicious findings (Groot et al., 2015).

In a regular workflow, the breast compression is performed in the up-right body position. In the CC view the breast is placed on the bucky , which is initially positioned at the inframammary folder level or a few cm higher depending on breast mobility in the ¹⁸⁷⁵ corresponding direction. Then the technologist lowers the compression paddle using a foot switch and gently pull the breast onto the bucky to correctly position the breast and to maximize the amount of projected tissues. In the MLO view, the bucky is rotated to an angle between 40 to 55 degrees. The woman rests the lateral oblique site of her breast against the bucky. In this view the pectoral muscle is located between the detector the ¹⁸⁸⁰ compression paddle; As the muscle is stiffer than the breast tissues , the woman have to stay relaxed in order to have better breast flattening. When lowering the compression paddle, the technologist have to pull the breast up and forward to prevent drooping of the breast, and again smoothen out any skin folds.

The mammography devices are equipped with paddle position and force sensors to ¹⁸⁸⁵ measure and display the compressed breast thickness and the amount of force applied to the breast.

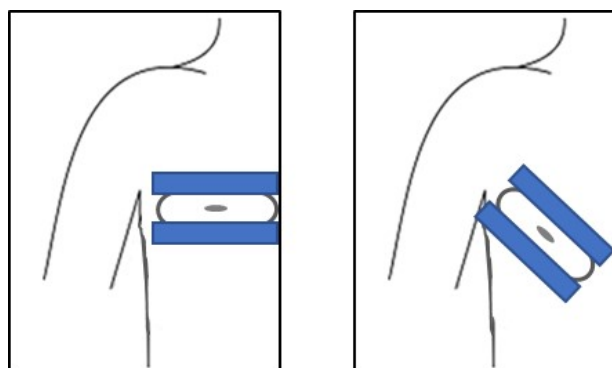


Figure 5.1: left: cranio-caudal breast compression; right - mediolateral oblique breast compression

5.2.2 Compression mechanics

de Groot et al. (2015) studied the breast compression cycle, according to the authors the compression cycle is characterized by two phase: flattening and clapping. During the flattening phase, the breast is gradually deformed by increasing the compression force, the deformation lasted 7.5 ± 2.6 . By contrast, during the clamping phase which last approximately 12.8 ± 3.6 , the compression paddle is immobilized holding the breast in a stationary position.

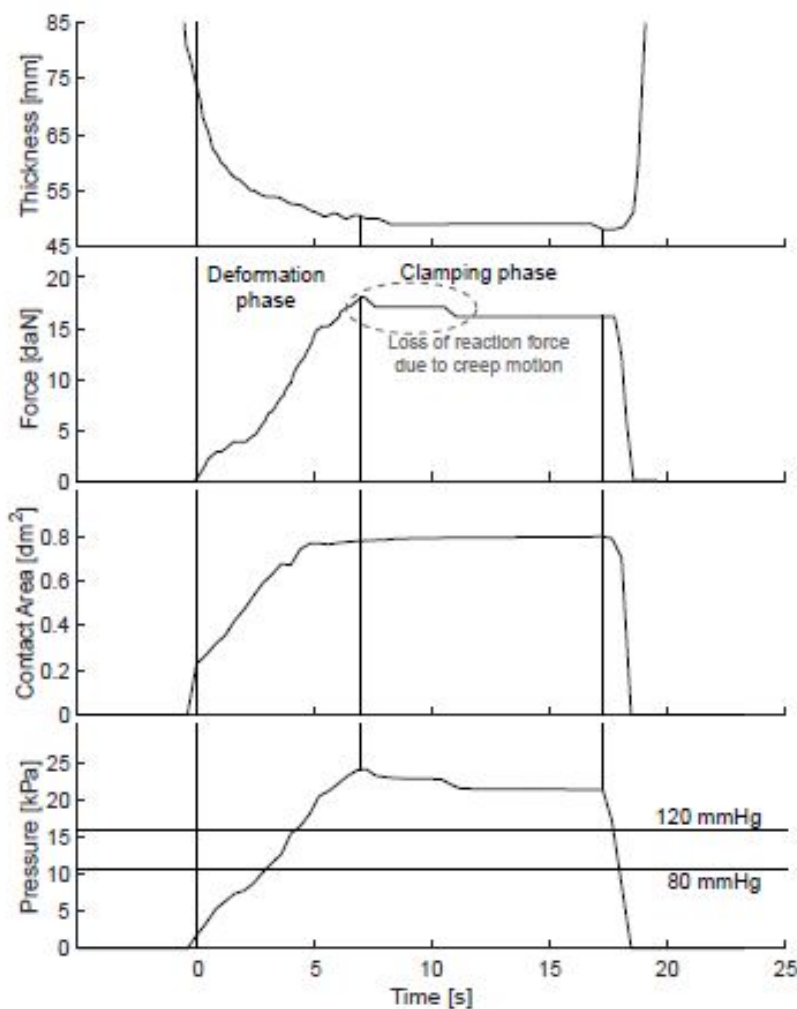


Figure 5.2: A typeical breast compression cycle. Reproduced from Groot et al. (2015)

Figure 5.2 shows a typical compression cycle for a CC breast compression. One can see that during the compression paddle the breast thickness and contact area evolve non-linearly and remains constant during the clamping phase. The compression force and pressure increase quasi-linearly, however in the first 10s of the clamping phase they slightly decrease. This may be explained by breast volume changes because of the viscous effusion

of blood and lymph into the central systems.

Figure 5.3 shows the relation between breast thickness and compression force depending on breast size and firmness. One can see that, for a larger breast size higher compression force is needed, but the overall behavior remains the same. For similar breast sizes, the final compression force stay within the same range, however a firmer breast will reach faster the limiting value of breast thickness resulting in a direct increase of the compression force.

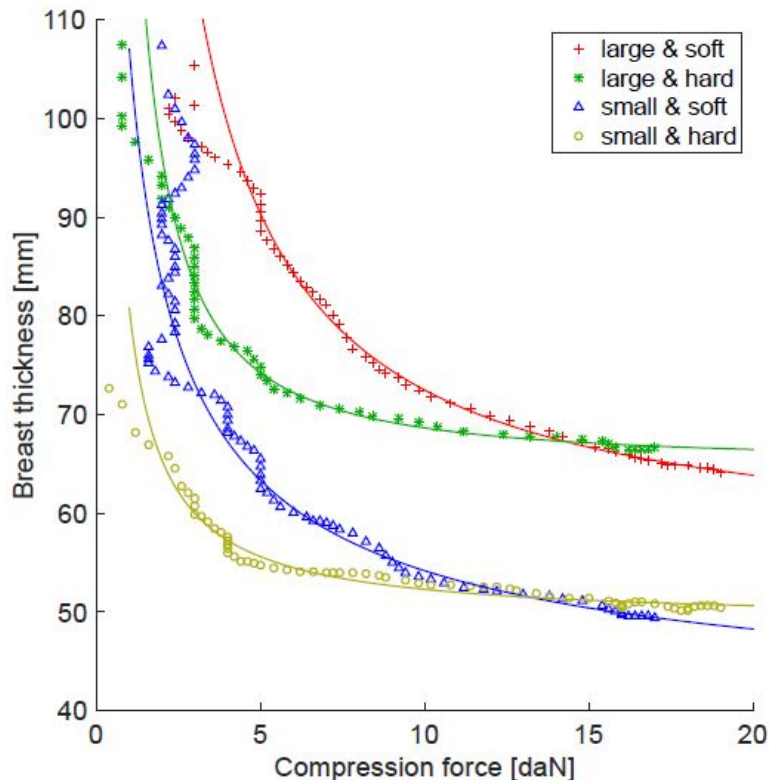


Figure 5.3: Characteristic breast flattening curve as function of the applied force. Reproduced from Groot et al. (2015)

1905

5.2.3 Compression paddle designs

In addition to the large and small standard paddles, many compression paddles of varying size and shape are included with each mammography unit. Although each paddle has specific indications, using the paddles creatively may facilitate the positioning process

1910 The technologist gradually compresses the breast in order to even out the breast thickness and to spread out the soft tissues. Nowadays, two types of compression paddles are widely available: rigid compression paddles (RCP) and flex compression paddles (FCP).

The RCP is fixed to its frame and is constrained to move in the up-down direction. This paddle has some flexibility because of material mechanical properties and can slightly bend when compressing the breast, while remaining globally flat and parallel to the image receptor. On the other hand, the FCP is attached to its frame by rotational joints and therefore, presents an additional rotational degree of freedom enabling the paddle to tilt with respect to the image receptor plane (Figure 3.c).

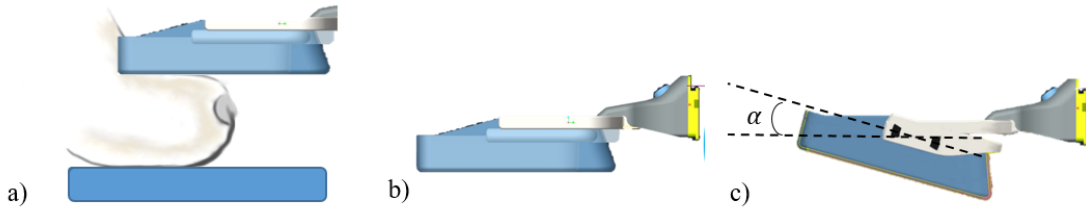


Figure 5.4: Breast compression between the paddle (up) and the receiver (down): a) Rigid paddle; b) Flex paddle with flexion angle α

5.3 Pain and discomfort

5.4 Image quality and average glandular dose

5.5 Conclusion

Great strides in positioning are evident in the field today. We are imaging more tissue than before, but not without experiencing some drawbacks. For example, imaging greater amounts of posterior tissue in thick breasts can reduce the amount of compression in the anterior breast possibly obscuring a small anterior cancerous tumor. The technologist has the critical job of applying positioning methods using common sense, as in the previous case an additional third projection to better compress the anterior tissue may be necessary. Use of available tools, such as the American Mammographics S.O.F.T. Paddle or Hologic FAST Paddle may be another option.

Breast compression quality evaluation

6.1 Breast compression simulation

Knowing what, in a clinical framework, woman breast is compressed only in a up-right or prone body position, the respective breast geometries are usually used to estimate tissues deformation under compression . In such modeling conditions, the gravity induced tissues pre-stresses can be neglected when compared to the compression induced stresses (Han et al., 2012; Ruiter et al., 2006; Sturgeon et al., 2016). However, for a different framework, as a multi-loading gravity simulation the latter assumptions highly penalizes the simulation results.

1940 6.2 Image acquisition simulation

6.3 Compreure quality metrics

6.3.1 Patient comfort

With a rigid paddle, the breast under compression presents a nearly uniform thickness all over the contact surface. Contrariwise, with a flex paddle, the compressed breast thickness decreases quasi linearly from the chest wall to the nipple. Flex paddles are used to better conform the breast contours and thereby to improve compression. However, Broeders and colleagues¹¹ have shown that such compression paddle may decrease the diagnostic quality of mammograms as the breast tissues may be pushed out to the chest wall resulting in less retro-glandular tissue visible on the image.

1950 The volunteers were also asked to provide the compression force and breast thickness as measured on their most recent mammograms. Such data are summarized in Table 6.1.

	Subject 1		Subject 2	
	Right breast	Left breast	Right breast	Left breast
Force (N)	21.9	40.9	94.8	56.6
Breast thickness (mm)	47	42	50	49

Table 6.1: Compression force and breast thickness for both subjects for a cranio-caudal mammogram

6.3.2 Image quality

To assess the impact of breast compression on image quality, we inserted a set of microcalcifications into each compressed breast volume. The smallest breast volume contains 21 microcalcifications arranged in a matrix of 7 rows and 3 columns (Figure 4a). The largest breast volume contains 56 microcalcifications arranged in a matrix of 7 rows and 8 columns. The matrix of calcifications is parallel with the entrance surface of the image receptor and positioned at the breast mid thickness (Figure 4b). The distance between two consecutive columns or rows is 10mm. We assumed a uniform breast-equivalent material composed of glandular/adipose tissue with a 20/80 ratio. A mammogram was simulated using typical clinical acquisition parameters obtained with the standard automatic optimization of parameters (AOP) mode. Two simulations were performed with microcalcifications of 0.2 mm and 0.3mm in diameter. The signal-difference-to-noise ratio (SDNR) per pixel of these microcalcifications was measured. Additionally, the signal-to-noise ratio (SNR) was computed on the same pixels excluding the microcalcifications.

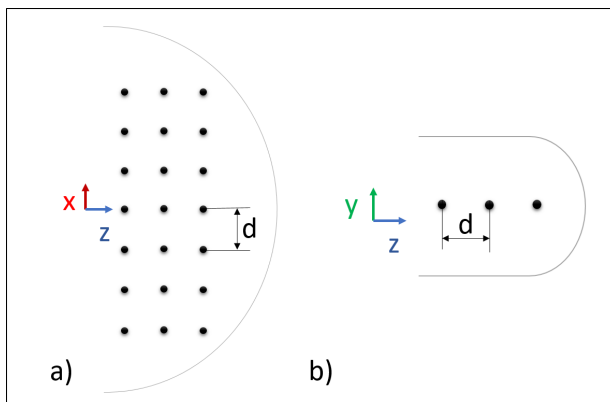


Figure 6.1: Microcalcification distribution over the smallest breast volume ($d = 10\text{mm}$): a) axial view, b) sagittal view.

6.3.3 Average glandular dose

The average glandular dose (AGD) was derived using the approach proposed by Dance et al¹² regardless the paddle type. In practice, it is very difficult to accurately measure the

exact breast thickness. Thus, the nominal breast thickness was used to compute conversions factors which relate measurements of incident air kerma to the delivered mean glandular dose.

6.4 Results

The force versus breast thickness curves are plotted in Figure 5 for both volunteers with the rigid and flex paddles. We observed a nominal compression thickness roughly equals for both paddles. The resulting internal stress and strain distributions, as well as contact pressure maps were derived at compressive forces of 22 N for the first volunteer (Figure 6) and 95 N for the second one (Figure 7).

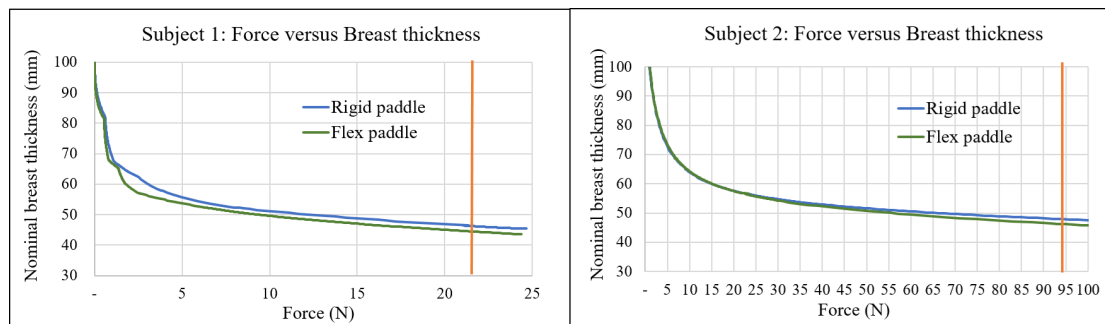


Figure 6.2: Resulting breast thickness for a given compression force

As concerns the small breast volume (Figure 6), there is no significant difference between FCP and RCP in pressure distribution over the skin surface or in internal stress/strain intensity distributions. For both compression paddles, high pressure at the skin surface is concentrated in the juxtathoracic region with a maximum pressure of 77.7 kPa. Several clinical studies^{11,13} sustained this result of no significant difference in experienced pain when using FCP or RCP. In addition, the FE simulations confirm that in small breasts the paddle tilt is too small to impact the tissues compression in the middle part of the breast. FCP applied on large breast volumes (Figure 7) results in significantly lower intensities of pressure at the skin surface in contact with the compression paddle, with a maximal pressure of 37 kPa, compared to 56 kPa when using RCP. No significant difference in the measured maximal intensities of strain and stress was observed, however strain and stress distribution patterns are different. When the breast is compressed with a rigid paddle, maximal strain and stress are concentrated in the retromammary space and decrease considerably toward the nipple. When a flex paddle is used, stress and strain are more uniformly distributed over the breast volume with the highest values in the middle third of the breast. The areal pressure distribution patterns has already been demonstrated in the work by Dustler and colleagues¹³. The authors have studied the pressure distribution patterns of 103 women undergoing breast compression with a rigid paddle at different compression levels. Four groups have been differentiated: a) skin pressure widespread over the

breast (29%); b) skin pressure concentrated on the central part of the breast (8%); c) skin pressure concentrated on the juxtathoracic region (16%); d) skin pressure concentrated along a narrow zone at the juxtathoracic region (26%). The pressure distribution patterns
2000 observed for our first and second volunteers correspond to the group d and a respectively.

The nominal breast thickness may vary by about 2mm between rigid and flex paddle for both volunteers (Table 3). Accordingly, no significant difference was found between the estimated AGD, while a dose reduction of 2% for the smaller breast and 4% for larger breast was observed.

2005 The SNR and SDNR have been estimated and compared between flex and rigid paddles. When using a flex paddle instead of a rigid paddle on the largest breast (volunteer 2), we observe a statistically significantly higher SNR. The same trend is observed on SDNR for both 200 and 300 m microcalcifications, while not statistically significant. We did not observe any statistically significant difference in SNR or SDNR for microcalcification of any
2010 size when considering the compression of the smallest breast by a rigid or a flex paddle. Therefore, despite a breast thickness varying linearly from chest wall to nipple when the flex compression paddle is used, the image quality is preserved or improves compared to the image quality obtained with the rigid compression paddle.

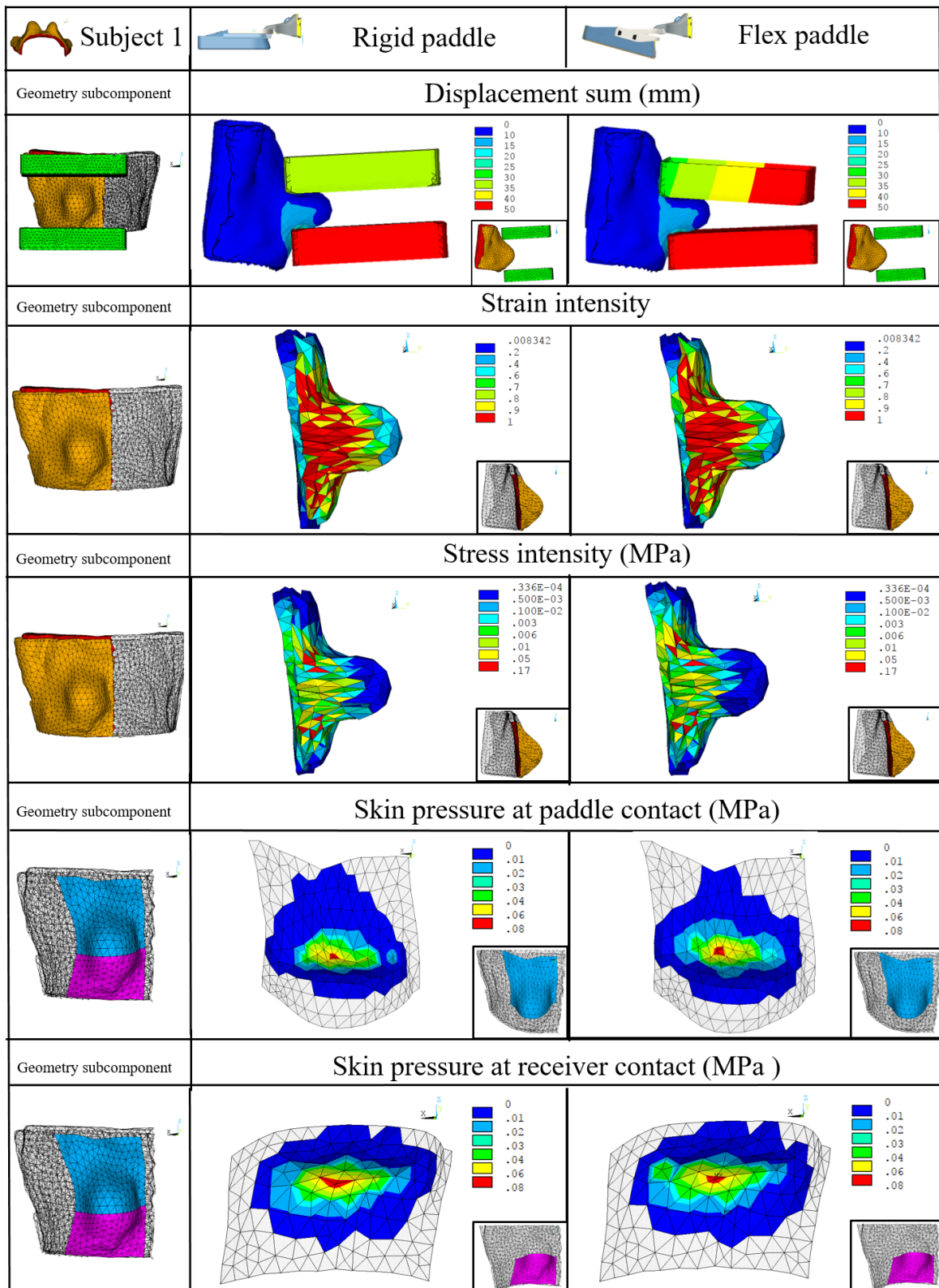


Figure 6.3: Stress, strain and contact pressure distribution for the first subject

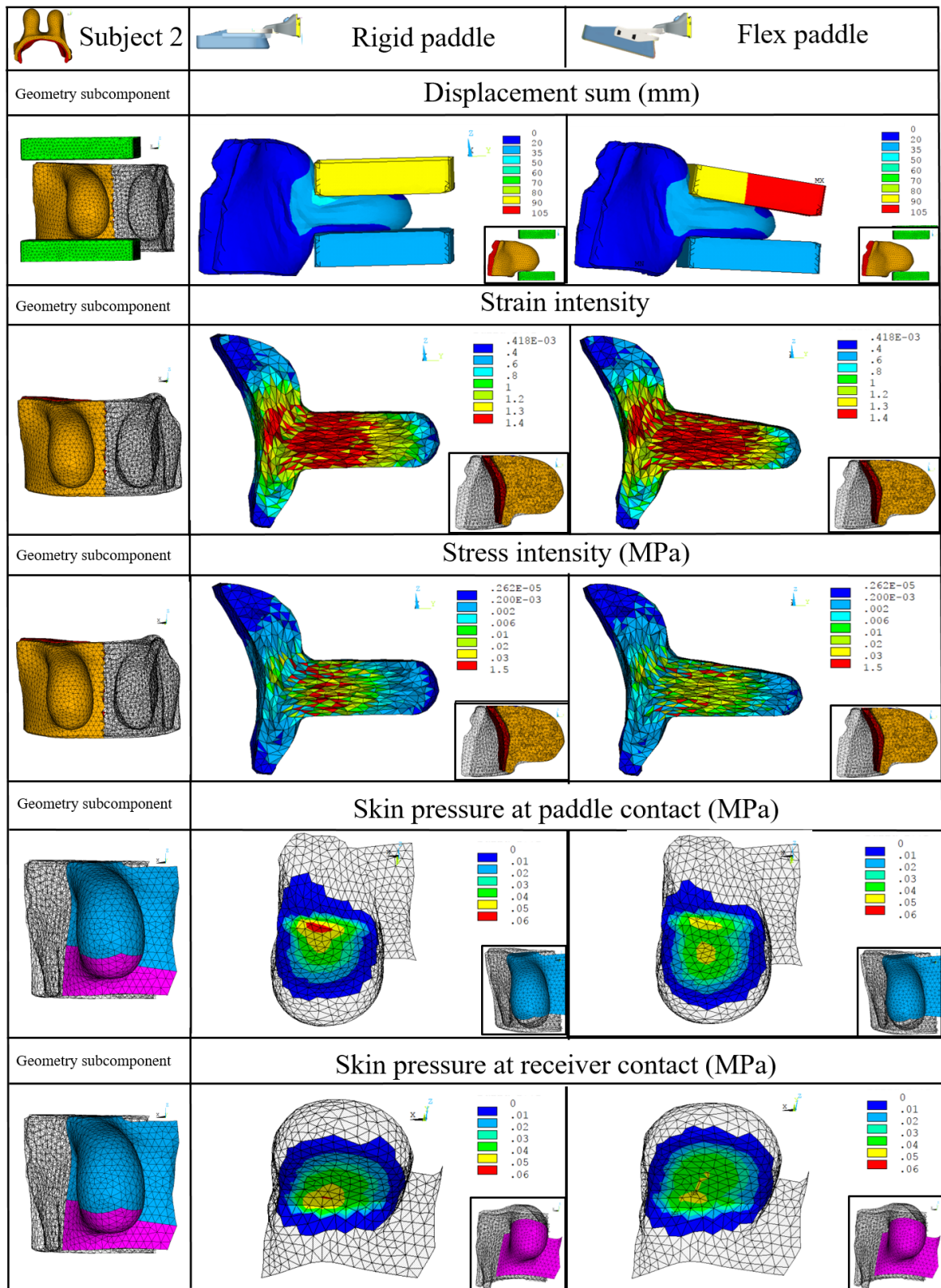


Figure 6.4: Stress, strain and contact pressure distribution for the second subject

	Rigid Paddle		Flex Paddle		p-Values	Rigid Paddle		Flex Paddle	
	Mean SNR	StdDev SNR	Mean SNR	StdDev SNR		BNT (mm)	AGD (mGy)	BNT (mm)	AGD (mGy)
Volunteer 1	82,90	43,09	83,70	37,72	0,706	46	1,15	44	1,12
Volunteer 2	126,89	8,75	137,21	10,73	0,000	48	1,20	46	1,15

	200 um				300 um					
	Rigid Paddle		Flex Paddle		Rigid Paddle		Flex Paddle			
	Mean SDNR	StdDev SDNR	Mean SDNR	StdDev SDNR	p-Values	Mean SDNR	StdDev SDNR	Mean SDNR	StdDev SDNR	p-Values
Volunteer 1	0,74	0,68	0,79	0,54	0,689	2,01	1,28	1,85	1,02	0,224
Volunteer 2	1,14	0,57	1,13	0,53	0,885	2,96	0,76	3,15	0,92	0,093

Figure 6.5: Breast nominal thickness (BNT), average glandular dose (AGD), signal-to-noise-ratio (SNR) and signal-difference-to-noise (SDNR) for both volunteers and both compression paddle types

6.5 Discussions and conclusion

2015 Breast compression with flex and rigid paddle have been simulated using the finite elements theory applied to segmented MRI images acquired on 2 volunteers under different geometries. Applying the Gent form of strain-energy potential, instead of the Neo-Hookean form, allowed to obtain compression force magnitudes comparable with the real subject data. After simulating the breast compression, the SDNR of microcalcifications and the
2020 AGD, delivered during the acquisition of the corresponding simulated mammography, have been computed. The simulations have been repeated for two different breast volumes (cup sizes A and F) with a rigid and a flex paddle. The four configurations have been analyzed to compare patient perceived pain (measured as strain and stress) and image quality (measured as SNR, SDNR and AGD). The results of our simulations indicate that, for the
2025 smallest breast, there is no significant difference for the patient perceived pain when using the rigid or the flex paddle. The shape of the breast under compression does not present significant changes between the two paddle designs. We did not observe any statistically significant difference in SNR or SDNR for microcalcification of any size when considering the compression of the smallest breast by a rigid or a flex paddle. Therefore, our results suggest that using a flex paddle should not significantly impact image quality and delivered dose in small breasts, and should not reduce significantly the perceived pain.
2030 For the largest breast, our simulations indicate that using a flex paddle may reduce the maximal pressure intensity on the skin surface by about 30% compared to the rigid paddle. The tissues deformation is more uniformly distributed inside the breast volume, and the
2035 highest deformation is occurring in the middle breast region corresponding to the supposed location of dense tissues. Moreover, our simulations have shown that flex paddle have no significant impact on the average glandular dose and improves image quality compared to the rigid paddle. In conclusion, our simulations confirm that using the flex paddle used for breast compression may improve the patient comfort without affecting the image quality
2040 and the delivered average glandular dose. Moreover, despite a breast thickness varying linearly from chest wall to nipple, when a flex compression paddle is used on large breasts, the image quality seems to be preserved or improved compared to the image quality obtained with a rigid compression paddle

Part V

Thesis review

Conclusion

Perspective

2050 esel

Bibliography

- Abeyaratne, R. (2012). *Continuum Mechanics: Volume II of Lecture Notes on The Mechanics of Elastic Solids*. Cambridge MA and Singapore. 25
- 2055 Abu-Hijleh, M., Roshier, A., Al-Shboul, Q., Dharap, A., and Harris, P. (2006). The membranous layer of superficial fascia: evidence for its widespread distribution in the body. *Surgical and Radiologic Anatomy*, 28(6):606–619. 15
- ACS (2017). American cancer society: Types of breast cancer. <https://www.cancer.org/cancer/breast-cancer/understanding-a-breast-cancer-diagnosis/types-of-breast-cancer.html>. 18, 19
- 2060 Andolina, V. and Lillé, S. (2011). *Mammographic imaging: a practical guide*. Lippincott Williams & Wilkins. 14, 17, 18
- Andrews, F. J. (2001). Pain during mammography: implications for breast screening programmes. *Journal of Medical Imaging and Radiation Oncology*, 45(2):113–117. 22
- 2065 ANSYS (2017a). *ANSYS Contact Technology Guide*, 17 edition. 44
- ANSYS (2017b). *Theory reference for the mechanical APDL and mechanical applications*, 17 edition. 38
- Aro, A. R., Absetz-Ylöstalo, P., Eerola, T., Pamilo, M., and Lönnqvist, J. (1996). Pain and discomfort during mammography. *European Journal of Cancer*, 32(10):1674–1679.
- 2070 3
- Aro, A. R., De Koning, H. J., Absetz, P., and Schreck, M. (1999). Psychosocial predictors of first attendance for organised mammography screening. *Journal of Medical Screening*, 6(2):82–88. 22
- Azar, F. S., Metaxas, D. N., and Schnall, M. D. (2002). Methods for modeling and predicting mechanical deformations of the breast under external perturbations. *Medical Image Analysis*, 6(1):1–27. 33, 48, 50, 51, 54
- 2075 Bayati, S. and Seckel, B. R. (1995). Inframammary crease ligament. *Plastic and reconstructive surgery*, 95(3):501–508. 15

BIBLIOGRAPHY

- 2080 Belytschko, T., Liu, W. K., Moran, B., and Elkhodary, K. (2013). *Nonlinear finite elements for continua and structures*. John wiley & sons. 25, 37
- Bucki, M., Lobos, C., and Payan, Y. (2010). A fast and robust patient specific finite element mesh registration technique: application to 60 clinical cases. *Medical image analysis*, 14(3):303–317. 62
- 2085 Calvo-Gallego, J. L., Martínez-Reina, J., and Domínguez, J. (2015). A polynomial hyper-elastic model for the mixture of fat and glandular tissue in female breast. *International Journal for numerical methods in biomedical engineering*, 31(9). 67
- Carter (2009a). *Determining material properties of the breast for image-guided surgery*. International Society for Optics and Photonics. 50, 51
- 2090 Carter, T., Han, L., Taylor, Z., Tanner, C., Beechy-Newman, N., Ourselin, S., and Hawkes, D. (2012). Application of biomechanical modelling to image-guided breast surgery. *Soft Tissue Biomechanical Modeling for Computer Assisted Surgery*, pages 71–94. 48, 63
- Carter, T. J. (2009b). *Biomechanical modelling of the breast for image-guided surgery*. PhD thesis, University of London. 46, 47, 48, 49, 51, 52
- 2095 Catanuto, G., Spano, A., Pennati, A., Riggio, E., Farinella, G. M., Impoco, G., Spoto, S., Gallo, G., and Nava, M. B. (2008). Experimental methodology for digital breast shape analysis and objective surgical outcome evaluation. *Journal of Plastic, Reconstructive & Aesthetic Surgery*, 61(3):314–318. 13
- Chan, H.-P., Galhotra, S., Vyborny, C. J., MacMahon, H., Jokich, P. M., et al. (1987). Image feature analysis and computer-aided diagnosis in digital radiography. i. automated detection of microcalcifications in mammography. *Medical physics*, 14(4):538–548. 20
- 2100 Cheung, J. T.-M., Zhang, M., and An, K.-N. (2004). Effects of plantar fascia stiffness on the biomechanical responses of the ankle-foot complex. *Clinical Biomechanics*, 19(8):839–846. 52
- Chung, J.-H., Rajagopal, V., Nielsen, P. M., and Nash, M. P. (2008). Modelling mammographic compression of the breast. In *Medical Image Computing and Computer-Assisted Intervention MICCAI 2008*, pages 758–765. Springer. 50
- 2105 Ciocca, D. R. and Fanelli, M. A. (1997). Estrogen receptors and cell proliferation in breast cancer. *Trends in Endocrinology & Metabolism*, 8(8):313–321. 18
- Clemente, C. D. (2011). *Anatomy: a regional atlas of the human body*. Wolters Kluwer-/Lippincott Williams & Wilkins Health. 13, 15, 63
- Conley, R. H., Meszoely, I. M., Weis, J. A., Pheiffer, T. S., Arlinghaus, L. R., Yankeelov, T. E., and Miga, M. I. (2015). Realization of a biomechanical model-assisted image guidance system for breast cancer surgery using supine mri. *International journal of computer assisted radiology and surgery*, 10(12):1985–1996. 46

BIBLIOGRAPHY

- 2115 de Groot, J. E., Broeders, M. J., Grimbergen, C. A., and den Heeten, G. J. (2015). Pain-preventing strategies in mammography: an observational study of simultaneously recorded pain and breast mechanics throughout the entire breast compression cycle. *BMC women's health*, 15(1):26. 80
- 2120 Dullum, J. R., Lewis, E. C., and Mayer, J. A. (2000). Rates and correlates of discomfort associated with mammography. *Radiology*, 214(2):547–552. 3, 22
- Eder, M., Raith, S., Jalali, J., Volf, A., Settles, M., Machens, H.-G., and Kovacs, L. (2014). Comparison of Different Material Models to Simulate 3-D Breast Deformations Using Finite Element Analysis. *Annals of Biomedical Engineering*, 42(4):843–857. 48, 49
- 2125 Eiben, B., Lacher, R., Vavourakis, V., Hipwell, J. H., Stoyanov, D., Williams, N. R., Sabczynski, J., Bülow, T., Kutra, D., Meetz, K., et al. (2016a). Breast conserving surgery outcome prediction: A patient-specific, integrated multi-modal imaging and mechano-biological modelling framework. In *International Workshop on Digital Mammography*, pages 274–281. Springer. 48
- 2130 Eiben, B., Vavourakis, V., Hipwell, J. H., Kabus, S., Buelow, T., Lorenz, C., Mertzanidou, T., Reis, S., Williams, N. R., Keshtgar, M., and Hawkes, D. J. (2016b). Symmetric Biomechanically Guided Prone-to-Supine Breast Image Registration. *Annals of Biomedical Engineering*, 44(1):154–173. 46
- 2135 Eiben, B., Vavourakis, V., Hipwell, J. H., Kabus, S., Lorenz, C., Buelow, T., and Hawkes, D. J. (2014). Breast deformation modelling: comparison of methods to obtain a patient specific unloaded configuration. *Proc. SPIE*, 9036:903615–8. 47
- Eiben, B., Vavourakis, V., Hipwell, J. H., Kabus, S., Lorenz, C., Buelow, T., Williams, N. R., Keshtgar, M., and Hawkes, D. J. (2016c). Surface driven biomechanical breast image registration. In *SPIE Medical Imaging*, pages 97860W–97860W. International Society for Optics and Photonics. 46, 52, 53, 54
- 2140 Fanelli, M. A., Vargas-Roig, L. M., Gago, F. E., Tello, O., De Angelis, R. L., and Ciocca, D. R. (1996). Estrogen receptors, progesterone receptors, and cell proliferation in human breast cancer. *Breast cancer research and treatment*, 37(3):217–228. 18
- Feldman, A. G. (1986). Once more on the equilibrium-point hypothesis (λ model) for motor control. *Journal of motor behavior*, 18(1):17–54. 49
- 2145 Fleming, P., O'Neill, S., Owens, M., Mooney, T., and Fitzpatrick, P. (2013). Intermittent attendance at breast cancer screening. *Journal of public health research*, 2(2). 22
- FNAH (2016). Cancer du sein : modalités spécifiques de dépistage pour les femmes haut risque. https://www.has-sante.fr/portail/jcms/c_1740821/fr/cancer-du-sein-modalites-specifiques-de-depistage-pour-les-femmes-a-haut-risque. 19

FRM (2017). Les chiffres du cancer du sein. <https://www.frm.org/cancer-du-sein/>.
18

Fung, Y.-c. (2013). *Biomechanics: mechanical properties of living tissues*. Springer Science & Business Media. 66

2155 Fung, Y.-c., Tong, P., and Chen, X. (2017). *Classical and computational solid mechanics*, volume 2. World Scientific Publishing Company. 60

Gamage, T. P. B., Boyes, R., Rajagopal, V., Nielsen, P. M. F., and Nash, M. P. (2012). Modelling prone to supine breast deformation under gravity loading using heterogeneous finite element models. In Poul M.F. Nielsen, Adam Wittek, and Karol Miller, editors, 2160 *Computational Biomechanics for Medicine*, pages 29–38. Springer New York. 46, 50, 52, 54, 60, 66

Garcia, E., Oliver, A., Diaz, O., Diez, Y., Gubern-Merida, A., Marti, R., and Marti, J. (2017). Mapping 3d breast lesions from full-field digital mammograms using subject-specific finite element models. In *SPIE Medical Imaging*, pages 1013504–1013504. International Society for Optics and Photonics. 48, 54

2165 Gefen, A. (2003). The in vivo elastic properties of the plantar fascia during the contact phase of walking. *Foot & ankle international*, 24(3):238–244. 52

Gefen, A. and Dilmoney, B. (2007). Mechanics of the normal woman’s breast. *Technology and Health Care*, 15(4):259–271. 52

2170 Gent, A. (1996). A new constitutive relation for rubber. *Rubber chemistry and technology*, 69(1):59–61. 74

Gent, A. and Thomas, A. (1958). Forms for the stored (strain) energy function for vulcanized rubber. *Journal of Polymer Science Part A: Polymer Chemistry*, 28(118):625–628. 34

2175 Georgii, J., Paetz, T., Harz, M., Stoecker, C., Rothgang, M., Colletta, J., Schilling, K., Schloo-Z-Vries, M., Mann, R. M., and Hahn, H. K. (2016). Simulation and visualization to support breast surgery planning. In *International Workshop on Digital Mammography*, pages 257–264. Springer. 46, 50, 51, 52, 54

Govindjee, S. and Mihalic, P. A. (1998). Computational methods for inverse deformations in quasi-incompressible finite elasticity. *International Journal for Numerical Methods in Engineering*, 43(5):821–838. 47

Griesenauer, R. H., Weis, J. A., Arlinghaus, L. R., Meszoely, I. M., and Miga, M. I. (2017). Breast tissue stiffness estimation for surgical guidance using gravity-induced excitation. *Physics in Medicine and Biology*, 62(12):4756. 50, 52, 60

BIBLIOGRAPHY

- 2185 Groot, J. E. d., Branderhorst, W., Grimbergen, C. A., Heeten, G. J. d., and Broeders, M. J. (2015). Towards personalized compression in mammography: A comparison study between pressure- and force-standardization. *European Journal of Radiology*, 84(3):384–391. viii, viii, 79, 80, 81
- 2190 Han, L., Hipwell, J. H., Eiben, B., Barratt, D., Modat, M., Ourselin, S., and Hawkes, D. J. (2014). A nonlinear biomechanical model based registration method for aligning prone and supine mr breast images. *IEEE transactions on medical imaging*, 33(3):682–694. 48, 50, 51, 52, 53, 54, 60, 63
- 2195 Han, L., year, J. H., Tanner, C., Taylor, Z., Mertzanidou, T., Jorge Cardoso, Sébastien Ourselin, and David J Hawkes (2012). Development of patient-specific biomechanical models for predicting large breast deformation. *Physics in Medicine and Biology*, 57(2):455–472. 46, 49, 50, 51, 83
- Hendriks, F., Brokken, D., Oomens, C., Bader, D., and Baaijens, F. (2006). The relative contributions of different skin layers to the mechanical behavior of human skin in vivo using suction experiments. *Medical engineering & physics*, 28(3):259–266. 51
- 2200 Hofvind, S., Geller, B., Skelly, J., and Vacek, P. (2012). Sensitivity and specificity of mammographic screening as practised in vermont and norway. *The British journal of radiology*, 85(1020):e1226–e1232. 20
- 2205 Hopp, T., Dietzel, M., Baltzer, P. A., Kreisel, P., Kaiser, W. A., Gemmeke, H., and Ruiter, N. V. (2013). Automatic multimodal 2d/3d breast image registration using biomechanical fem models and intensity-based optimization. *Medical image analysis*, 17(2):209–218. 66
- Huang, S.-Y., Boone, J. M., Yang, K., Packard, N. J., McKenney, S. E., Prionas, N. D., Lindfors, K. K., and Yaffe, M. J. (2011). The characterization of breast anatomical metrics using dedicated breast ct. *Medical physics*, 38(4):2180–2191. 14
- 2210 Itoh, A., Ueno, E., Tohno, E., Kamma, H., Takahashi, H., Shiina, T., Yamakawa, M., and Matsumura, T. (2006). Breast disease: clinical application of us elastography for diagnosis. *Radiology*, 239(2):341–350. 21
- Kaliske, M. and Rothert, H. (1997). On the finite element implementation of rubber-like materials at finite strains. *Engineering Computations*, 14(2):216–232. 74
- 2215 Kanitakis, J. (2002). Anatomy, histology and immunohistochemistry of normal human skin. *European journal of dermatology: EJD*, 12(4):390–9. 14
- Kellner, A. L., Nelson, T. R., Cervino, L. I., and Boone, J. M. (2007). Simulation of mechanical compression of breast tissue. *IEEE Transactions on Biomedical Engineering*, 54(10):1885–1891. 46

BIBLIOGRAPHY

- 2220 Kemp Jacobsen, K., O'meara, E. S., Key, D., SM Buist, D., Kerlikowske, K., Vejborg, I., Sprague, B. L., and Lynge, E. (2015). Comparing sensitivity and specificity of screening mammography in the united states and denmark. *International journal of cancer*, 137(9):2198–2207. 20
- Kopans, D. B. (2007). *Breast imaging*. Lippincott Williams & Wilkins. 11, 12, 15, 16, 20
- 2225 Krouskop, T. A., Wheeler, T. M., Kallel, F., Garra, B. S., and Hall, T. (1998). Elastic moduli of breast and prostate tissues under compression. *Ultrasonic Imaging*, 20(4):260–274. 49, 50
- Kuhlmann, M., Fear, E., Ramirez-Serrano, A., and Federico, S. (2013). Mechanical model of the breast for the prediction of deformation during imaging. *Medical engineering \& physics*, 35(4):470–478. 47, 54
- 2230 Leong, H.-T., Ng, G. Y.-f., Leung, V. Y.-f., and Fu, S. N. (2013). Quantitative estimation of muscle shear elastic modulus of the upper trapezius with supersonic shear imaging during arm positioning. *PloS one*, 8(6):e67199. 51
- Lima, E., K. M. M., Júnior, J. F. S. C., de Albuquerque Pereira, W. C., and de Oliveira, L. F. (2018). Assessment of the mechanical properties of the muscle-tendon unit by supersonic shear wave imaging elastography: a review. *Ultrasonography*, 37(1):3. 51
- 2235 Lorenzen, J., Sinkus, R., Biesterfeldt, M., and Adam, G. (2003). Menstrual-cycle dependence of breast parenchyma elasticity: estimation with magnetic resonance elastography of breast tissue during the menstrual cycle. *Investigative radiology*, 38(4):236–240. 17, 49
- Martin, L. J. (2017). What causes breast cancer? <https://www.webmd.com/breast-cancer/guide/what-causes-breast-cancer>. 17, 18
- 2240 Martínez-Martínez, F., Rupérez-Moreno, M., Martínez-Sober, M., Solves-Llorens, J., Lorente, D., Serrano-López, A., Martínez-Sanchis, S., Monserrat, C., and Martín-Guerrero, J. (2017). A finite element-based machine learning approach for modeling the mechanical behavior of the breast tissues under compression in real-time. *Computers in Biology and Medicine*, 90:116–124. 46, 48, 52
- Mugea, T. T. and Shiffman, M. A. (2014). *Aesthetic Surgery of the Breast*. Springer. 13, 15, 63
- 2245 NHSBSP (2012). 2012 review of the uk breast screening programme. <http://www.cancerresearchuk.org/about-cancer/breast-cancer/screening/screening-2012-review>. 19
- Nordez, A. and Hug, F. (2010). Muscle shear elastic modulus measured using supersonic shear imaging is highly related to muscle activity level. *Journal of applied physiology*, 108(5):1389–1394. 49

BIBLIOGRAPHY

- Ogden, R. W. (1972). Large deformation isotropic elasticity—on the correlation of theory and experiment for incompressible rubberlike solids. In *Proc. R. Soc. Lond. A*, volume 326, pages 565–584. The Royal Society. 35
- Olgun, D. Ç., Korkmazer, B., Kılıç, F., Dikici, A. S., Velidedeoğlu, M., Aydoğan, F., Kantarcı, F., and Yilmaz, M. H. (2014). Use of shear wave elastography to differentiate benign and malignant breast lesions. *Diagnostic and Interventional Radiology*, 20(3):239. 21
- Palomar, A. P. d., Calvo, B., Herrero, J., Lpez, J., and Doblar, M. (2008). A finite element model to accurately predict real deformations of the breast. *Medical Engineering & Physics*, 30(9):1089–1097. 46, 47, 60
- Pandya, S. and Moore, R. G. (2011). Breast development and anatomy. *Clinical obstetrics and gynecology*, 54(1):91–95. 17
- Patete, P., Iacono, M. I., Spadea, M. F., Trecate, G., Vergnaghi, D., Mainardi, L. T., and Baroni, G. (2013). A multi-tissue mass-spring model for computer assisted breast surgery. *Medical Engineering and Physics*, 35(1):47–53. 54
- Pathmanathan, P., Gavaghan, D. J., Whiteley, J. P., Chapman, S. J., and Brady, J. M. (2008). Predicting tumor location by modeling the deformation of the breast. *IEEE Transactions on Biomedical Engineering*, 55(10):2471–2480. 47, 51, 52, 54
- Pechter, E. A. (1998). A new method for determining bra size and predicting postaugmentation breast size. *Plastic and reconstructive surgery*, 102(4):1259–1265. 12
- Peters, N. H., Borel Rinkes, I. H., Zuithoff, N. P., Mali, W. P., Moons, K. G., and Peeters, P. H. (2008). Meta-analysis of mr imaging in the diagnosis of breast lesions. *Radiology*, 246(1):116–124. 22
- Peto, R., Boreham, J., Clarke, M., Davies, C., and Beral, V. (2000). Uk and usa breast cancer deaths down 25% in year 2000 at ages 20–69 years. *The Lancet*, 355(9217):1822. 18
- Pike, M. C., Spicer, D. V., Dahmoush, L., and Press, M. F. (1993). Estrogens progestogens normal breast cell proliferation and breast cancer risk. *Epidemiologic reviews*, 15(1):17–35. 17
- Poulos, A., McLean, D., Rickard, M., and Heard, R. (2003). Breast compression in mammography: how much is enough? *Journal of Medical Imaging and Radiation Oncology*, 47(2):121–126. 3
- Rajagopal, V., Chung, J.-H., Highnam, R. P., Warren, R., Nielsen, P. M., and Martyn P. Nash (2010a). Mapping microcalcifications between 2d mammograms and 3d MRI using a biomechanical model of the breast. In Karol Miller and Poul M.F. Nielsen, editors, *Computational Biomechanics for Medicine*, pages 17–28. Springer. 50

- Rajagopal, V. et al. (2007). *Modelling breast tissue mechanics under gravity loading*. PhD thesis, ResearchSpace@ Auckland. 54
- ²²⁹⁵ Rajagopal, V., Lee, A., Chung, J.-H., Warren, R., Highnam, R. P., Nash, M. P., and Nielsen, P. M. (2008). Creating individual-specific biomechanical models of the breast for medical image analysis. *Academic Radiology*, 15(11):1425–1436. 47, 48, 49, 50, 52
- Rajagopal, V., Nielsen, P. M. F., and Nash, M. P. (2010b). Modeling breast biomechanics for multi-modal image analysis—successes and challenges. *Wiley Interdisciplinary Reviews: Systems Biology and Medicine*, 2(3):293–304. 48
- ²³⁰⁰ Riggio, E., Quattrone, P., and Nava, M. (2000). Anatomical study of the breast superficial fascial system: the inframammary fold unit. *European Journal of Plastic Surgery*, 23(6):310–315. 52
- ²³⁰⁵ Rivlin, R. S. and Saunders, D. (1951). Large elastic deformations of isotropic materials vii. experiments on the deformation of rubber. *Phil. Trans. R. Soc. Lond. A*, 243(865):251–288. 34
- Rohan, P.-Y., Lobos, C., Nazari, M. A., Perrier, P., and Payan, Y. (2014). Finite element modelling of nearly incompressible materials and volumetric locking: a case study. *Computer methods in biomechanics and biomedical engineering*, 17(sup1):192–193. 60
- ²³¹⁰ Ruiter, N. V., Stotzka, R., MULLER, T.-O., Gemmeke, H., Reichenbach, J. R., and Kaiser, W. (2006). Model-based registration of x-ray mammograms and MR images of the female breast. *IEEE Transactions on Nuclear Science*, 53(1):204–211. 46, 60, 83
- Samani, A., Bishop, J., Yaffe, M. J., and Plewes, D. B. (2001). Biomechanical 3-d finite element modeling of the human breast using MRI data. *Medical Imaging, IEEE Transactions on*, 20(4):271–279. 49, 50
- ²³¹⁵ Samani, A. and Plewes, D. (2004). A method to measure the hyperelastic parameters of ex vivo breast tissue samples. *Physics in Medicine and Biology*, 49(18):4395–4405. 50
- Samani, A., Zubovits, J., and Plewes, D. (2007). Elastic moduli of normal and pathological human breast tissues: an inversion-technique-based investigation of 169 samples. *Physics in medicine and biology*, 52(6):1565. 48
- ²³²⁰ Sinkus, R., Tanter, M., Xydeas, T., Catheline, S., Bercoff, J., and Fink, M. (2005). Viscoelastic shear properties of in vivo breast lesions measured by mr elastography. *Magnetic resonance imaging*, 23(2):159–165. 50
- Skandalakis, J. E. (2009). Embryology and anatomy of the breast. *Breast augmentation: principles and practice*. Springer, Berlin, 12. 11

BIBLIOGRAPHY

- 2325 SPF (2016). Sante publique france: Cancer du sein.
<http://invs.santepubliquefrance.fr/Dossiers-thematiques/Maladies-chroniques-et-traumatismes/Cancers/Donnees-par-localisation/Cancer-du-sein>. 18
- 2330 Sturgeon, G. M., Kiarashi, N., Lo, J. Y., Samei, E., and Segars, W. P. (2016). Finite-element modeling of compression and gravity on a population of breast phantoms for multimodality imaging simulation. *Medical Physics*, 43(5):2207–2217. 46, 47, 48, 52, 83
- Sutradhar, A. and Miller, M. J. (2013). In vivo measurement of breast skin elasticity and breast skin thickness. *Skin Research and Technology*, 19(1). 14, 51, 73
- Tabár, L., Vitak, B., Chen, H.-H. T., Yen, M.-F., Duffy, S. W., and Smith, R. A. (2001). Beyond randomized controlled trials. *Cancer*, 91(9):1724–1731. 19
- 2335 Tanner, C., Schnabel, J. A., Hill, D. L. G., Hawkes, D. J., Leach, M. O., and Hose, D. R. (2006). Factors influencing the accuracy of biomechanical breast models. *Medical Physics*, 33(6):1758. 48
- Treloar, L. (1943). The elasticity of a network of long-chain moleculesii. *Transactions of the Faraday Society*, 39:241–246. 34
- 2340 Ulger, H., Erdogan, N., Kumanlioglu, S., and Unur, E. (2003). Effect of age, breast size, menopausal and hormonal status on mammographic skin thickness. *Skin Research and Technology*, 9(3):284–289. 15
- Van Houten, E. E., Doyley, M. M., Kennedy, F. E., Weaver, J. B., and Paulsen, K. D. (2003). Initial in vivo experience with steady-state subzone-based mr elastography of the human breast. *Journal of magnetic resonance imaging*, 17(1):72–85. 50
- 2345 Vandeput, J. and Nelissen, M. (2002). Considerations on anthropometric measurements of the female breast. *Aesthetic plastic surgery*, 26(5):348–355. 13
- Vavourakis, V., Hipwell, J. H., and Hawkes, D. J. (2016). An inverse finite element u/p-formulation to predict the unloaded state of in vivo biological soft tissues. *Annals of biomedical engineering*, 44(1):187–201. 47
- 2350 Wellman, P., Howe, R. D., Dalton, E., and Kern, K. A. (1999). Breast tissue stiffness in compression is correlated to histological diagnosis. *Harvard BioRobotics Laboratory Technical Report*, pages 1–15. 48, 50
- Wenger, M. P., Bozec, L., Horton, M. A., and Mesquida, P. (2007). Mechanical properties of collagen fibrils. *Biophysical journal*, 93(4):1255–1263. 52
- 2355 Whelehan, P., Evans, A., Wells, M., and MacGillivray, S. (2013). The effect of mammography pain on repeat participation in breast cancer screening: a systematic review. *The Breast*, 22(4):389–394. 22

BIBLIOGRAPHY

- 2360 Yaffe, M., Boone, J., Packard, N., Alonzo-Proulx, O., Huang, S.-Y., Peressotti, C., Al-Mayah, A., and Brock, K. (2009). The myth of the 50-50 breast. *Medical physics*, 36(12):5437–5443. 14
- Yeoh, O. (1990). Characterization of elastic properties of carbon-black-filled rubber vulcanizates. *Rubber chemistry and technology*, 63(5):792–805. 35
- 2365 Youk, J. H., Gweon, H. M., and Son, E. J. (2017). Shear-wave elastography in breast ultrasonography: the state of the art. *Ultrasonography*, 36(4):300. 21
- Zajac, F. E. (1989). Muscle and tendon properties models scaling and application to biomechanics and motor. *Critical reviews in biomedical engineering*, 17(4):359–411. 49

